MAX-PLANCK-INSTITUT
FÜR POLYMERFORSCHUNG

JOHANNES GUTENBERG
UNIVERSITÄT MAINZ

Stretchable Organic Electrochemical Transistors: From Material Design to Device Characterization

Dissertation zur Erlangung des akademischen Grades eines „Doctor rerum naturalium“ (Dr. rer. nat.) der Fachbereiche:

08: Physik, Mathematik und Informatik, 09: Chemie, Pharmazie, Geographie und Geowissenschaften, 10: Biologie, Universitätsmedizin

vorgelegt von *Carla Volkert*

Mainz im Mai 2025

Max Planck Graduate Center
mit der Johannes Gutenberg-Universität

Die vorliegende Dissertation wurde in der Zeit von November 2021 bis April 2025 am Max-Planck-Institut für Polymerforschung in Mainz unter der Betreuung von [redacted] angefertigt.

1. Gutachter: [redacted]

2. Gutachter: [redacted]

3. Gutachter: [redacted]

Tag der mündlichen Prüfung: [redacted]

I hereby declare that I wrote the dissertation submitted without any unauthorized external assistance and used only sources acknowledged in the work. All textual passages which are appropriated verbatim or paraphrased from published and unpublished texts as well as all information obtained from oral sources are duly indicated and listed in accordance with bibliographical rules. In carrying out this research, I complied with the rules of standard scientific practice as formulated in the statutes of Johannes Gutenberg-University Mainz to insure standard scientific practice.

.....

(Carla Volkert)

Abstract

Stretchable electronics are rapidly emerging as a key technology for wearable healthcare applications, driving intense research efforts in the field. Among these, stretchable organic electrochemical transistors (OECTs) have gained considerable attention as mixed-conductor devices capable of transporting both electronic and ionic charges. This unique property allows them to seamlessly interface with biological systems, making them highly promising for biomedical applications. The conductive polymer poly(3,4-ethylenedioxythiophene):poly(styrenesulfonate) (PEDOT:PSS) plays a pivotal role in these devices due to its dual charge transport capability, excellent mechanical properties, biocompatibility and commercial availability. Despite their promising future, stretchable electronics and OECTs in particular face notable challenges. This includes the development of reliable fabrication techniques for stretchable systems and addressing the trade-off between stretchability and conductivity, which is a major bottleneck in the field. Furthermore, little is known about how strain-induced morphological changes in PEDOT:PSS affect the coupled ionic and electronic transport in stretchable OECTs. Addressing these obstacles and deepening the understanding of stretchable OECTs was the focus of this doctoral thesis. Accordingly, this doctoral thesis is structured into three main sections: fabrication, electrical understanding and integration into stretchable OECTs.

As a foundational step for this thesis, a fast, reliable and versatile transfer-printing method is developed to deposit PEDOT:PSS onto flexible, transparent and biodegradable poly(vinyl alcohol) (PVA):glycerol substrates (**Chapter 3**). This approach avoids harsh chemical treatments and is compatible with established techniques to enhance PEDOT:PSS's stretchability and conductivity. The transfer-printed films are validated through electrical and morphological studies, and a simple O_2-plasma patterning method is introduced to pattern PEDOT:PSS and create structures, which are also successfully transfer-printed onto stretchable substrates. These methodologies pave the way towards stretchable OECTs.
Before utilizing a conducting material in stretchable OECTs, it is essential to understand its electrical and morphological response to strain. While PEDOT:PSS is a widely used material in stretchable electronics, its inherent brittleness limits its ability to withstand significant stretching. To address this, **Chapter 4** examines the effects of organic plasticizers on the morphology and electrical properties of PEDOT:PSS thin-films using a two-layer system of transfer-printed PEDOT:PSS on stretchable PVA substrates infused with glycerol (15 - 55 wt%). Within this system, glycerol is found to diffuse into PEDOT:PSS, causing reorganization of PEDOT and PSS. This process, modeled using multicomponent diffusion, is found to cause a plasticizer-dependent conductivity increase due to more interconnected PEDOT domains. This reorganization improves the material's response to strain and enables crack-free elongation, allowing pristine PEDOT:PSS to stretch up to 160 %. The improved response to strain becomes evident in an increased conductivity with strain, which is attributed to PEDOT chain alignment.
Chapter 5 builds upon the transfer-printing process, O_2-plasma-patterning and insights into electrical behavior under strain to incorporate these findings into stretchable OECTs. Two device configurations are investigated, applying strain either parallel or perpendicular to the current flow. The impact of geometric and morphological changes—both essential for optimal OECT performance—are studied systematically. Geometric changes affect the transfer and output characteristics, electrolyte resistance, turn-off voltage and charge time, revealing opposing trends between the two configurations across all parameters. Focusing on hole mobility and ion uptake, strain-induced morphological changes are found to cause anisotropic charge transport and a reduction in volumetric capacitance, with the latter being independent of the device configuration. However, the parallel arrangement compensates this loss by enhancing charge carrier mobility. These findings underscore the critical role of geometric and morphological considerations in optimizing OECT performance under strain.

Zusammenfassung

Angesichts der vielversprechenden Anwendungsmöglichkeiten von dehnbarer Elektronik (vor allem im Gesundheitswesen, z. B. als Sensoren auf der Haut), hat die Forschung in diesem Bereich in den letzten Jahren stark zugenommen. Dabei sind organische elektrochemische Transistoren (OECTs) als Mischleiter-Bauelemente, die sowohl elektronische als auch ionische Ladungen transportieren können, von besonderem Interesse. Dank dieser einzigartigen Eigenschaft können sie sich nahtlos in biologische Systeme einfügen, was sie für biomedizinische Anwendungen sehr vielversprechend macht. Das leitfähige Polymer Poly(3,4-Ethylendioxythiophen):poly(styrolsulfonat) (PEDOT:PSS) spielt aufgrund seiner doppelten Ladungstransportfähigkeit, seiner hervorragenden mechanischen Eigenschaften, seiner Biokompatibilität und seiner kommerziellen Verfügbarkeit eine zentrale Rolle in diesen Bauteilen. Trotz ihrer vielversprechenden Anwendungsmöglichkeiten stehen dehnbare Elektronik und insbesondere OECTs vor bemerkenswerten Herausforderungen. Dazu gehören die Entwicklung zuverlässiger Herstellungstechniken für dehnbare Systeme, die Bewältigung des Zielkonflikts zwischen Dehnbarkeit und Leitfähigkeit—ein großer Engpass in diesem Bereich—und die Erforschung der Auswirkungen dehnungsinduzierter morphologischer Veränderungen in PEDOT:PSS auf den gekoppelten ionischen und elektronischen Transport in dehnbaren OECTs. Die Adressierung dieser Hindernisse und die Vertiefung des Verständnisses von dehnbaren OECTs war der Schwerpunkt dieser Doktorarbeit. Dementsprechend gliedert sich diese Dissertation in drei Hauptabschnitte: Herstellung, elektrisches Verständnis und Integration in dehnbare OECTs.

Als grundlegender Schritt für diese Arbeit wird ein schnelles, zuverlässiges und vielseitiges Transferdruckverfahren entwickelt, um PEDOT:PSS auf flexible, transparente und biologisch abbaubare Poly(vinylalkohol) (PVA):Glycerin-Substrate aufzubringen (**Chapter 3**). Dieser Ansatz vermeidet aggressive chemische Behandlungen und ist kompatibel mit etablierten Techniken zur Verbesserung der Dehnbarkeit und Leitfähigkeit von PEDOT:PSS. Die transfergedruckten Filme werden durch elektrische und morphologische Studien validiert, und es wird eine einfache O_2-Plasma-Strukturierungsmethode zur Herstellung von PEDOT:PSS-Strukturen eingeführt, die ebenfalls erfolgreich auf dehnbare Substrate transfergedruckt werden. Diese Methoden ebnen den Weg zu dehnbaren OECTs.
Bevor ein leitendes Material in dehnbaren OECTs eingesetzt werden kann, ist es wichtig, seine elektrische und morphologische Reaktion auf Dehnung zu verstehen. PEDOT:PSS ist zwar ein in der dehnbaren Elektronik weit verbreitetes Material, doch seine inhärente Sprödigkeit schränkt seine Fähigkeit ein, einer erheblichen Dehnung standzuhalten. Um dieses Problem zu adressieren, werden in **Chapter 4** die Auswirkungen von organischen Weichmachern auf die Morphologie und die elektrischen Eigenschaften von PEDOT:PSS anhand eines zweischichtigen Systems aus transfergedrucktem PEDOT:PSS auf dehnbaren PVA-Substraten untersucht, die mit Glycerin (15 - 55 wt%) versetzt sind. In diesem System diffundiert Glycerin in PEDOT:PSS und verursacht eine Reorganisation von PEDOT und PSS. Dieser Prozess, der mit Hilfe von Multikomponentendiffusion modelliert wird, führt zu einer weichmacherabhängigen Erhöhung der Leitfähigkeit, da die PEDOT-Domänen stärker miteinander verbunden sind. Diese Reorganisation verbessert die Reaktion des Materials auf Dehnung und ermöglicht selbige rissfrei, sodass PEDOT:PSS-Filme um bis zu 160 % gedehnt werden können. Das verbesserte Dehnungsverhalten zeigt sich in einer erhöhten Leitfähigkeit, die auf die Ausrichtung der PEDOT-Ketten zurückgeführt wird.
Chapter 5 baut auf dem Transferdruckverfahren, der O_2-Plasma-Strukturierung und den Erkenntnissen über das elektrische Verhalten unter Dehnung auf, um mit diesen Erkenntnissen intrinsisch dehnbare OECTs herzustellen und zu untersuchen. Es werden zwei OECT-Anordnungen untersucht, bei denen die Dehnung entweder parallel oder senkrecht zum Stromfluss erfolgt. Die Auswirkungen geometrischer und morphologischer Veränderungen—beide wesentlich für das Ein- und Ausschaltverhalten von OECTs—werden systematisch untersucht. Geometrische Veränderungen wirken sich auf die Transfer- und Ausgangskennlinien, den Elektrolytwiderstand, die Abschaltspannung

und die Reaktionszeit aus, wobei bei allen Parametern gegenläufige Tendenzen zwischen den beiden Anordnungen festgestellt werden. Im Hinblick auf die Ladungsträgermobilität der Löcher und die Ionenaufnahme wird festgestellt, dass dehnungsinduzierte morphologische Veränderungen einen anisotropen Ladungstransport und eine Verringerung der volumetrischen Kapazität verursachen, wobei letztere unabhängig von der Anordnung ist. Die parallele Anordnung mildert diesen Verlust jedoch ab, indem sie die Ladungsträgerbeweglichkeit erhöht. Diese Ergebnisse heben die zentrale Bedeutung geometrischer und morphologischer Änderungen in dehnbaren OECTs hervor und liefern wertvolle Ansätze für deren zukünftige Gestaltung.

Table of Contents

List of Abbreviations

AFM	atomic force microscopy
B-M (model)	Bernards-Malliaras model
D	drain
DBSA	4-dodecylbenzenesulfonic acid
DMSO	dimethylsulfoxide
DPP	diketopyrrolopyrrole
DPP-g2T	poly(2,5-bis(2-octyldodecyl)-3,6-di(thiophen-2-yl)-2,5-diketo-pyrrolopyrrole-alt-2,5-bis(3-triethyleneglycoloxy-thiophen-2-yl)
EG	ethylene glycol
EIS	electrochemical impedance spectroscopy
[EMIM]:[TFSI]	1-ethyl-3-methylimidazole bistrifluoromethanesulfonimide
G	gate
GIWAXS	grazing-incidence wide-angle X-ray scattering
GOPS	3-glycidyloxypropyl)trimethoxysilane
IL	ionic liquid
LED	light emitting diode
NaCl	sodium chloride
NW	nano wire
OECT	organic electrochemical transistor
OFET	organic field effect transistor
OLED	organic light-emitting diode
P3HT	poly(3-hexylthiophene-2,5-diyl)
PBS	phosphate-buffered saline
PDMS	poly(dimethylsiloxane)
PEDOT:PSS	poly(3,4-ethylenedioxythiophene): polystyrenesulfonate
PEO	poly(ethyleneglycol)
PET	poly(ethylene terephthalate)
p(g2T-T)	poly(2-(3,3'-bis(2-(2-(2-methoxyethoxy)ethoxy)ethoxy)-[2,2'-bithiophen]-5)yl thiophene)
PI	poly(imide)
PLA	poly(lactic acid)
PU	poly(urethane)
PTHS	poly(6-(thiophene-3-yl)hexane-1-sulfonate)tetrabutylammonium
PVA	poly(vinyl alcohol)
PVDF-HFP	poly(vinylidene fluoride-*co*-hexafluorpropylene)
S	source
SEBS	styrene ethylene butylstyren
SEM	scanning electron microscopy
SFM	scanning force microscopy

TPU	thermoplastic polyurethane
UV/vis	ultraviolet/ visible

1. Introduction

1.1 Stretchable and Flexible Electronics – a Growing Field

The field of stretchable and flexible electronics has grown rapidly over the last decade (**Fig. 1.1a**), propelled by the potential applications that generate scientific and commercial interest[1]. Stretchable electronic devices include optoelectronic devices[2], organic field effect transistors (OFETs)[3–5], light-emitting diodes (LEDs)[6] and organic electrochemical transistors (OECTs)[7–9], which are used, for example, in biosensors[10,11] as well as wearable electronics and electronic textiles[12,13]. Selected literature examples are shown in **Fig. 1.1b**. Generally speaking, the term 'stretchable electronics' refers to devices or materials with the ability to undergo significant deformation, typically beyond 10 % strain, while maintaining their electronic functionality[14]. This means that all examples mentioned can be deformed at least to a certain degree.

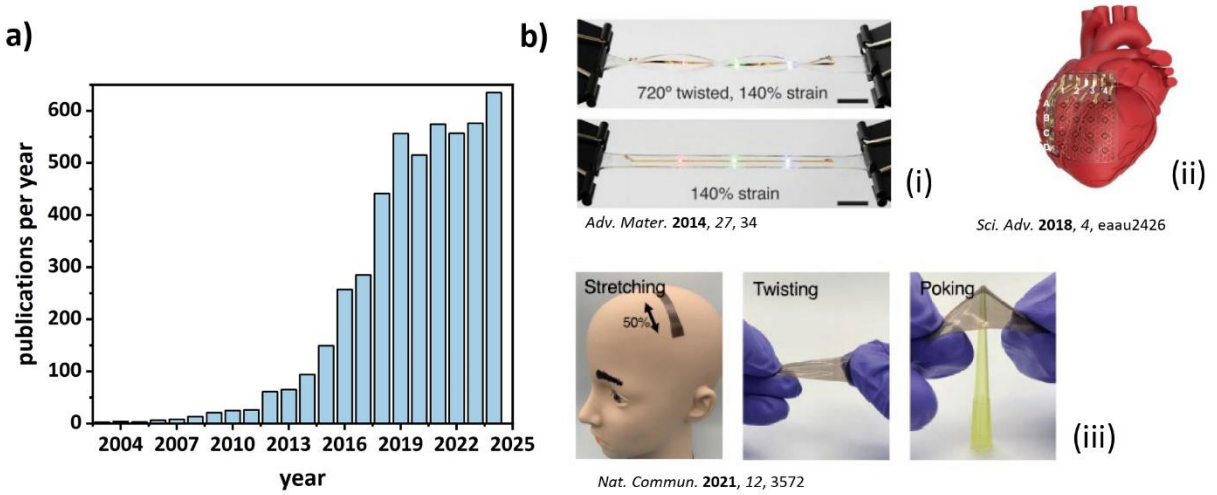

***Figure 1.1**: **a)** Publications per year, searching for 'stretchable and flexible electronics' in the web of science (date: 23.04.2025). **b)** Examples for stretchable electronics. (i) adapted from [15], (ii) adapted from [16] and (iii) adapted from [17].*

Among the mentioned examples, stretchable OECTs are particularly interesting as they are able to link the fields 'stretchable electronics' with 'organic bioelectronics', where one focuses on materials and the other on interfacing biological systems with electronic devices[18,19]. The overlap between these two fields is so significant that distinguishing them can be challenging. In the field of organic bioelectronics, OECTs frequently serve as the foundation for a diverse array of applications, with potential uses limited primarily by imagination—and, of course, experimental challenges. OECTs are exceptionally powerful because they can convert biological signals into electrical ones and vice versa[20]. This capability is driven by the movement of ions, which modulate the current flowing through the device. Therefore, direct electronic communication with biological environments is possible, as most biological processes—such as cellular signaling, molecular interactions and ion transport—are fundamentally based on the movement of ionic charges[21]. In addition, OECTs operate at low voltages (< 1 V) and have low power consumption[20,22], which is crucial for their application in wearables and on-skin electronics. For instance, OECTs have been successfully employed as COVID-19 sensors[11] and neuromorphic devices[23,24].

Often, OECTs are fabricated on rigid glass substrates with metal contacts serving as the source/ drain contacts and gate electrodes[11,25]. However, to enable close contact with the human body, a transition from rigid to stretchable and flexible materials is needed. Rigid materials like glass and metal can cause scar tissue formation, which impedes data recording, and their non-deformable nature makes achieving seamless contact with the human body challenging. The human body is soft, deformable and stretchable, with a maximum stretchability of approximately 30 %[9] (elbow), providing a benchmark for the strain tolerance required of stretchable devices. It is precisely for these reasons that more and more scientific efforts have been directed towards the development of stretchable and flexible OECTs in recent years.

Biocompatible organic polymers, both conducting and insulating, offer an ideal alternative to conventional materials. Since the elastic modulus of polymers matches that of human tissue (or can be adjusted to do so)[26,27], effective contact with human organs such as the skin is possible. This cannot be realized for rigid materials. However, the use of polymers brings its own challenges. The primary challenge lies in achieving materials that offer both conductivity and deformability simultaneously.
Broadly, the trade-off between conductivity and deformability can be managed through material design or intelligent device engineering. Accordingly, this introduction is organized into two primary sections. The first section (**Section 1.2**) explores materials commonly used in stretchable electronics, focusing on their morphology, which is essential for efficient charge transport, and strategies to enhance their stretchability. This includes an evaluation of the electrical performance of these modified systems under strain, along with common experimental challenges. The second section (**Section 1.3**) covers the integration of these materials into stretchable OECTs. It will introduce the operating principles of OECTs and methods for comprehensive analysis. Furthermore, this section delves into engineering approaches for the development of stretchable devices and provides an evaluation of the current advancements in this rapidly evolving field.

1.2 Materials for Stretchable Electronics

When researching materials for stretchable electronics, the main goal is to achieve a balance between efficient charge transport and mechanical deformability[1]. It is worth noting that engineering approaches are studied and implemented as well. However, these will be covered in **Section 1.3**. Conjugated polymers are the material of choice for stretchable electronics, as they have the potential to realize both conductivity and deformability. Furthermore, they offer several key advantages, including low-temperature and solution processability, mechanical flexibility and the fact that their molecular design can be tailored to specific needs[26,28–30]. Furthermore, their elastic modulus aligns with that of human tissue, making them particularly suitable for bio-integrated applications[26,27].

Research in the field of stretchable conjugated polymers can be conceptualized as a feedback loop, which is illustrated in **Fig. 1.2**. The process begins with the selection of a conducting polymer, followed by morphological modifications to enhance its ability to endure strain while retaining conductivity. Next, an appropriate insulating (and elastic) polymer is incorporated into the sample architecture, either to further improve deformability or as a structural necessity. Usually, the inclusion of an insulating polymer e.g. as a supporting substrate is mandatory rather than optional. This step is followed by the design of the overall sample architecture, which may sometimes precede the incorporation of the insulating polymer if appropriate. Once these elements are optimized, the material's electrical performance under strain is evaluated. If the performance meets expectations, the material can then be integrated into a stretchable device. If not, the feedback loop is revisited, and adjustments are made until the desired balance between conductivity and deformability is achieved.

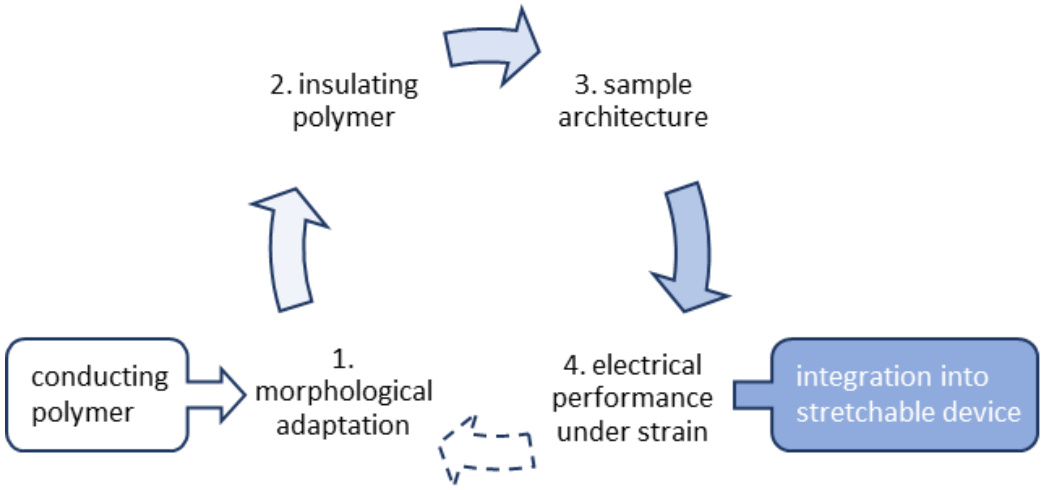

***Figure 1.2**: Schematic drawing of factors to consider and optimize to successfully develop materials for stretchable electronics.*

This section follows the structure of the feedback loop shown in **Fig. 1.2**. However, before discussing a specific polymer and how to morphologically adapt it, the basic physical relationship between conductivity and deformability in conjugated polymers will be discussed. This includes an explanation of what enables polymers to conduct charges and why these properties can have a detrimental effect on their mechanical flexibility.

1.2.1 Conductivity vs. Deformability in Conjugated Polymers

Polymers, both conducting and insulating, are composed of repeating monomer units arranged in a chain-like structure. In conducting polymers, electrical conductivity arises from their conjugated backbone, which consists of alternating single and double bonds, allowing for charge delocalization[31]. While conjugated polymers are (semi)conductors that transport charge (well) under certain conditions, they generally do not match the conducting properties of their inorganic counterparts. Nevertheless, their unique combination of processability, and chemical and mechanical adaptability makes them the preferred choice for stretchable electronics.

Focusing on conjugated polymers in their solid state and at room temperature, their morphology can be either amorphous, semi-crystalline or crystalline[32]. The specific state is influenced by the polymer's repeat units and the interactions between its chains, both of which contribute to the material's overall properties. Achieving full crystallization in polymers, however, is difficult due to their long-chain molecular structure, which leads to entanglements that hinder complete crystallization. As a result, the majority of polymers are semi-crystalline rather than crystalline[32]. This means that they consist of crystalline (ordered) and amorphous regions simultaneously[32,33] (schematically indicated in **Fig. 1.3**, bottom left). As mentioned above, conducting polymers possess a conjugated π-system that imparts their conductive properties, but this alone does not ensure high conductivity. For efficient charge transport, the polymer must exhibit a certain degree of molecular organization. This is because charge transport occurs both along and between polymer chains, requiring close packing for effective charge transport. Such organization is found in the crystalline regions of semi-crystalline polymers, where chains show strong π-π-stacking and long-range periodicity. In contrast, the amorphous regions are less ordered, and charge carriers primarily move along individual polymer chains with reduced efficiency[33–36]. While higher molecular order is beneficial for conductivity, it also tends to make the material more brittle. As brittle materials crack or break under strain, this affects not only their stretchability but also their conductive pathways, making it difficult to maintain conductivity during deformation[37,38]. Lower molecular order allows for deformations[36], however, as explained above, usually comes at the expense of the conductivity. This trade-off between molecular order and deformability presents a major challenge in developing stretchable electronics[26,30,37,38]. The phenomenon is schematically shown in **Fig. 1.3**: amorphous polymers tend to be deformable but exhibit poor conductivity, while semi-crystalline materials have better conductivity but lower deformability.

In terms of material design, there two ways of introducing stretchability in a conducting polymer, which are chemical and morphological adaptation[1,36]. This is schematically indicated in **Fig. 1.3**, right-hand side. Morphologic adaptation can be achieved by incorporating molecular additives[39–41] or insulating and elastic polymers[38,42]. Chemical adaptation has been reported for diketopyrrolopyrrole (DPP)-based polymers specifically[3,43–46], including side-chain engineering[46,47] and block-copolymers of semiconducting and elastomeric polymers[3,43,45].

Looking at the widely used polymer poly(3,4-ethylenedioxythiophene):polystyrene sulfonate (PEDOT:PSS), plasticizing the same via small or large molecules is the mainly investigated route. Furthermore, this work specifically targets PEDOT:PSS as a bench mark material for OECTs. Hence, it will also be the focus of this chapter from here on. After an introduction into the material itself, strategies for inducing conductivity and stretchability will be discussed. Then, a look into how modified PEDOT:PSS can be electrically analyzed will be taken and finally the current state of electrical performance under strain will be assessed.

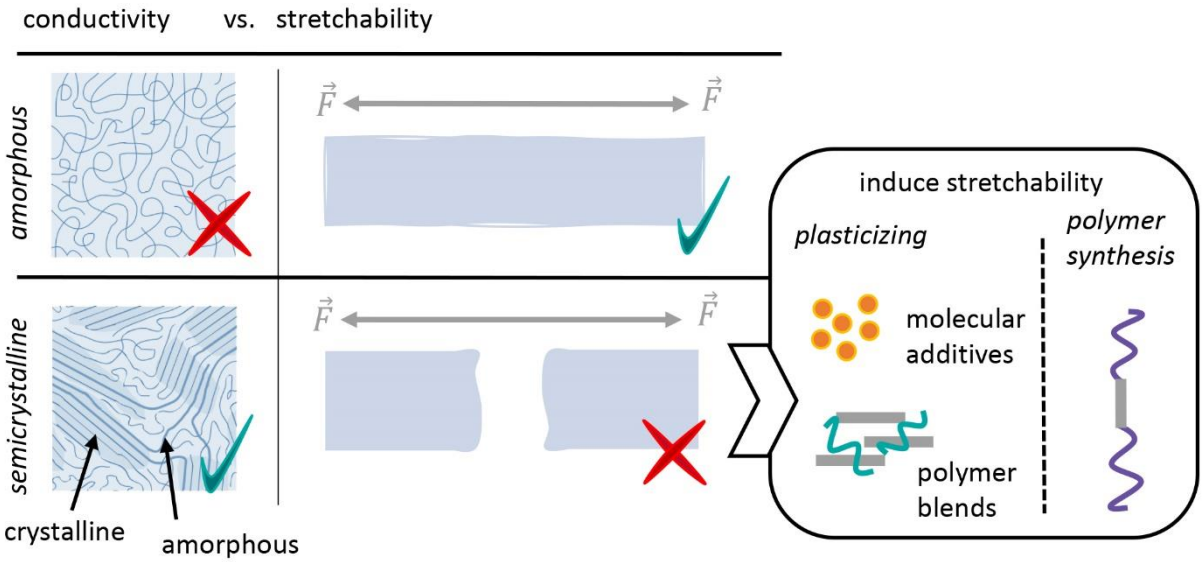

***Figure 1.3**: **Left**: Comparing conductivity and stretchability for amorphous and semi-crystalline polymers. Left-handed schematic adapted from [33]. **Right**: Stretchability in semi-crystalline polymers can be introduced via molecular additives, blending conducting and insulating e.g. elastic polymer as well as designated polymer synthesis.*

For comprehensive overviews of molecular design principles for stretchable organic polymeric semiconductors in general (not specifically PEDOT:PSS), please refer to [14,27,30,36,48].

1.2.2 PEDOT:PSS for Stretchable Electronics

As a material, the conductive organic polymer PEDOT:PSS is extremely widely used. Its popularity arises from several advantages, which include its optical transparency, mechanical properties, high conductivity and biocompatibility[37,49,50]. Additionally, its commercial availability has contributed massively to its popularity. PEDOT:PSS is a dark blue dispersion and can be easily processed into thin films—critical for organic electronics—using various techniques such as spin coating[51], inject-printing[52] or drop-casting[42]. Alternatively, electropolymerization[53] can be used to create PEDOT:PSS layers. All these advantages combined make it such an attractive candidate for stretchable electronics. Despite its popularity, PEDOT:PSS is a complex material to study due to its composition of two distinct polymers[20]. These are PEDOT- and PSS-chains; see **Fig. 1.4a** for the chemical structure. Within the composition, the PEDOT chains enable conductivity, owing to their conjugated backbone. It is important to point out that PEDOT is a p-type conductor. In contrast, PSS acts as a counter-ion for PEDOT, while also enabling its dispersion in water, as PEDOT is inherently water-insoluble[14]. This combination of PEDOT and PSS gives rise to a unique feature: PEDOT:PSS is an organic mixed ionic and electronic conductor (OMIEC), meaning it can conduct both electrons and ions. This dual capability is crucial for its usage in OECTs, a topic that will be explored in detail later (see **Section 1.3.1**).

This section focuses on the as-received adaptation of PEDOT:PSS to induce conductivity and stretchability, which is then analyzed in the form of a continuous thin film. However, it should be pointed out that other approaches have also been reported, such as chemical modification of the PSS in PEDOT:PSS[54] and in-situ polymerization of PEDOT in an elastic polymer[55]. In addition, studies on hydrogels[56,57] and porous structures (aerogels)[58] have shown interesting mechanical and electrical properties. However, non-continuous films, e.g. porous structures, are morphologically difficult to

analyze and represent a physical and engineering approach. This type of approach is discussed in **Section 1.3.2**.

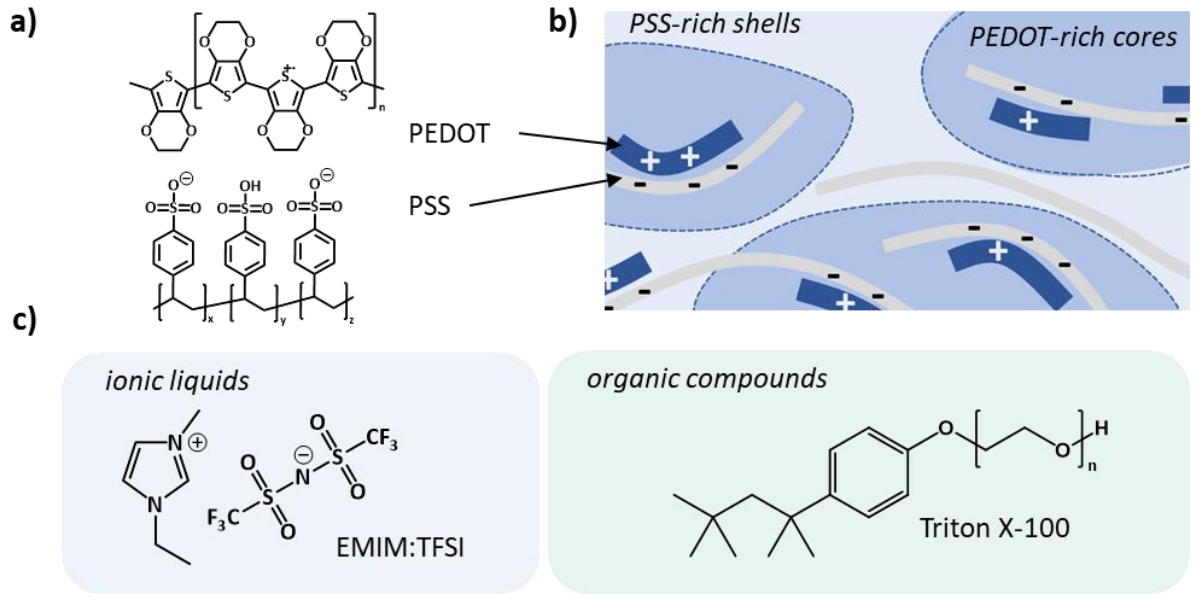

***Figure 1.4**: PEDOT:PSS for stretchable electronics: **a)** Chemical structure of PEDOT:PSS and **b)** schematic drawing of core-shell structure. **c)** Commonly used chemicals to simultaneously induce conductivity and stretchability within PEDOT:PSS.*

To integrate PEDOT:PSS into stretchable electronics, precise morphological modifications are essential to enhance and enable both conductivity and stretchability. In its pristine state, PEDOT:PSS exhibits low conductivity and like many highly conductive polymers, PEDOT:PSS becomes more brittle as the conductivity increases. However, even in its untreated state, PEDOT:PSS is inherently brittle[7,42,59–61], with a strain tolerance of less than 5%[62]. This poses a challenge for its application in stretchable electronics, where materials must maintain both high conductivity and mechanical flexibility. To address this, the addition of various chemicals have been explored. These include ionic liquids (ILs)[63–67], small/ low molecular weight organic molecules[40,68] and insulating and elastic organic polymers[69–71]. The small organic molecules used most frequently carry hydroxyl (OH) groups[68,72], such as D-sorbitol[68] (see below). Blending PEDOT:PSS with elastic polymers has been reported for Triton X-100[69,70], poly(vinylalcohol) (PVA)[61], poly(ethyleneglycol) (PEO or PEG; PEO herein)[62] and block-*co*-polymers[73,74] (see **Fig. 1.4c** for selected chemical structures). However, most frequently blends of PEDOT:PSS with insulating and elastic polymers as well as one or more additives simultaneously have been reported[41,42,57,75–78].

Given that PEDOT:PSS is most commonly processed via spin-coating, these additives can be introduced either before (pre-deposition) or after film formation (post-deposition). In pre-deposition methods, additives are mixed directly into the aqueous PEDOT:PSS dispersion[66,67,69,77], while post-deposition treatments typically involve applying solvents or other agents to the solid thin-films (e.g., via soaking[78]). The latter, however, is less frequently employed in the field of stretchable electronics. Regardless of the method, these treatments generally have a simultaneous effect on electrical conductivity and mechanical stretchability. Moreover, the simultaneous integration of several additives makes it even more difficult to attribute morphological and mechanical effects to a single

component. To improve clarity, the following discussion separates conductivity and stretchability, beginning with conductivity.

Conductivity

Structurally, thin-film PEDOT:PSS self-organizes into conductive PEDOT cores surrounded by an excess of insulating PSS shells (see **Fig. 1.4b** for schematic drawing)[79–81]. Inside the cores, PEDOT and PSS are bonded via Coulombic interactions, whereas outside the cores they are not bonded[81]. As mentioned above, pristine PEDOT:PSS has a conductivity of only about 1 S/cm. However, through the mentioned treatments, the conductivity can be increased to hundreds or thousands of S/cm[7,37,49,63,82]. This is done by changing the structural organization of PEDOT and PSS chains, which alters the distribution of PEDOT-rich cores and PSS-rich shells. This in turn influences the overall conductivity[49,83]. Due to the complex nature of PEDOT:PSS and the diversity of treatments applied, the exact mechanisms behind these conductivity enhancements are still being actively investigated. Several plausible explanations have been proposed, including: (1) a shift in the PEDOT resonance structure from a benzoid to a more planar quinoid form, (2) a conformational transition from a coil to an extended coil configuration, (3) increased grain size of the PEDOT domains, (4) improved phase separation between PEDOT and PSS, (5) improved crystallinity and (6) secondary doping or charge-screening effects[49,83]. Therefore, the effect of the individual treatments must be examined in detail in order to determine the underlying mechanism.

Stretchability

In addition to improving electrical performance, ensuring mechanical flexibility is essential in stretchable electronics. Many additives used to enhance stretchability function as plasticizers, although this is not always explicitly acknowledged in the literature. Plasticizers are compounds that are added to polymers to improve the mobility of the polymer chains by reducing their glass transition temperature (T_g)[30,32]. In this context, 'mobility' and 'mobile' refer to the freedom of movement of the polymer chains in the solid state at room temperature. The T_g-concept, however, is not easily applicable to PEDOT:PSS, as it is a polyelectrolyte with a naturally high T_g and to the best of my knowledge, the T_g(PEDOT:PSS) is not known. Hence, although the T_g(PEDOT:PSS) might be altered by a plasticizer, this cannot be easily measured.

While the principle of polymer re-arrangement triggered by a plasticizer is well researched for polymers without a conjugated backbone, the effect within conductive polymers like PEDOT:PSS is not yet fully understood[27,40]. This is attributed to the fact that conducting polymers are equipped with a conjugated backbone and carry charges[40] as well as experimental challenges: plasticized systems become more dynamic, reducing reproducibility and complicating analysis. On the other hand, lower mobility can delay a system's electrical response to strain, introducing time-dependent behavior. Such materials are less favorable for commercial applications that demand rapid and stable responses. Unfortunately, the influence of time-dependent deformation is rarely quantified in studies on PEDOT:PSS under strain.

Herein, the focus will be on organic plasticizers, as these are relevant for understanding the experimental results. Several mechanisms have been proposed to explain their effects. One commonly discussed mechanism is the weakening of interactions between polymer chains, which is thought result in a screening effect between PEDOT and PSS chains or among PSSH chains[49,84–87]. Some studies also suggest that small organic molecules can facilitate separating the PEDOT and PSS phases, thereby enhancing conductivity[42]. It is also discussed that the effect of plasticizers is the same as with insulating polymers, i.e. that they 'simply' increase the free volume and thus reduce the modulus of

elasticity[14]. And lastly, He et al.[40] identified the Hansen solubility parameter for small organic, non-polar, hydroxyl-carrying additives, specifically the hydrogen bonding parameter (δ_h). Additives with a larger δ_h were associated with a stronger plasticization of PEDOT:PSS, which significantly improved the response to strain. Although not all studies presented here investigated the conductivity of PEDOT:PSS under strain, these hypotheses are still relevant for understanding its behavior under such conditions.

In conclusion, the transition of PEDOT:PSS from a brittle, modestly conductive polymer into a highly stretchable and conductive material depends on carefully tailored morphological and chemical modifications. The dual influence of additives on both conductivity and flexibility underscores the importance of systematic investigations into their mechanisms of action. Before investigating the electrical performance of PEDOT:PSS under mechanical strain, sample preparation will be discussed briefly in the following.

Extensive literature on the effects of various conductivity-enhancing treatments on PEDOT:PSS can be found in [14,49,83]. It is worth noting that not all of these reviews are dedicated to the process of inducing stretchability in PEDOT:PSS.

1.2.3 Stretchable Systems

To study stretchable PEDOT:PSS thin-films (mixed with (organic) plasticizers), there are two common approaches regarding sample preparation: free-standing single-layer blends or layered structures with at least two stacked films, as shown schematically in **Fig. 1.5a** and **b**. In free-standing blends, PEDOT:PSS, an (elastic) insulating polymer and, if necessary, additives are mixed in the liquid state and deposited via drop-casting[41]. This means that there is no separate conducting layer. In layered structures, on the other hand, the conductive layer and the carrier substrate (the insulating polymer) are separate layers. The latter is also referred to as film-on-elastomer technique and employed more frequently[27,36].

Common choices for insulating polymers include poly(imide) (PI)[80,81], poly(dimethylsiloxane) (PDMS)[64,65,80,88], styrene ethylene butylstyrene (SEBS)[40,52,63,66,89,90], PVA[62,91], PEO[62], (thermoplastic) poly(urethane) (TPU/ PU)[58,67] and poly(lactic acid) (PLA)[92]. As a non-stretchable, but bendable substrate, poly (ethyleneterphthalate) (PET) also has been reported[93]. Some of the polymers' chemical structures are depicted in **Fig. 1.5c**. Each polymer offers distinct properties and is selected based on the intended application. One important aspect is the relaxation behavior of the material[36]. Some polymers fully recover their original shape after deformation (PDMS, SEBS, PU), while others undergo permanent deformation (PVA, PI). If the polymer undergoes permanent deformation (to at least some extend), it usually forms wrinkles perpendicular to the direction of applied strain upon relaxation. This might result in delamination as well as degradation of the conducting layer[36] and, therefore, should be taken into account as well.

While creating single-layer blends is a straightforward process, fabricating multi-layered structures poses greater challenges. The most direct approach is to spin-coat the PEDOT:PSS solution onto the flexible target substrate, as for instance reported by Wang et al.[63]. However, PEDOT:PSS adheres poorly to hydrophobic, flexible and stretchable substrates, making it difficult to form uniform films through spin-coating and often resulting in delamination[2]. One workaround is transfer-printing, which relies on the adhesion between the receiving substrate and the PEDOT:PSS layer. This method involves

lifting a spin-coated thin film from a donating substrate (usually glass) and placing it onto the target substrate, with or without the aid of a transfer medium[2,93–96]. This is schematically indicated in **Fig. 1.5d**. The advantage of transfer-printing is that it allows for harsher PEDOT:PSS treatments to increase its conductivity before transferring it onto the target substrate[2]. For successful transfer-printing, adjusting the adhesion of PEDOT:PSS is essential. This can be achieved by either reducing adhesion on the donor substrate or enhancing it on the receiving substrate. Various methods have been reported, including chemical treatments of the PEDOT:PSS[2,92,94], the target substrate[70] or both simultaneously[93]. To enhance adhesion on the receiving substrate, methods such as chemical functionalization (e.g., PDMS functionalization[70], **Fig. 1.5d**, right) or the exploitation of hydrogen bonding are employed. Combining these approaches helps optimize adhesion at multiple stages of the transfer process[93]. Alternatively, printing PEDOT:PSS formulations through a nozzle is a popular method for creating both layers and patterned structures[90,97]. Precise patterning is particularly essential for applications where PEDOT:PSS is used as electrodes or active layers in functional electronic devices, such as OECTs[98]. The process for creating these patterned structures will be discussed in more detail below (**Section 1.3.2**).

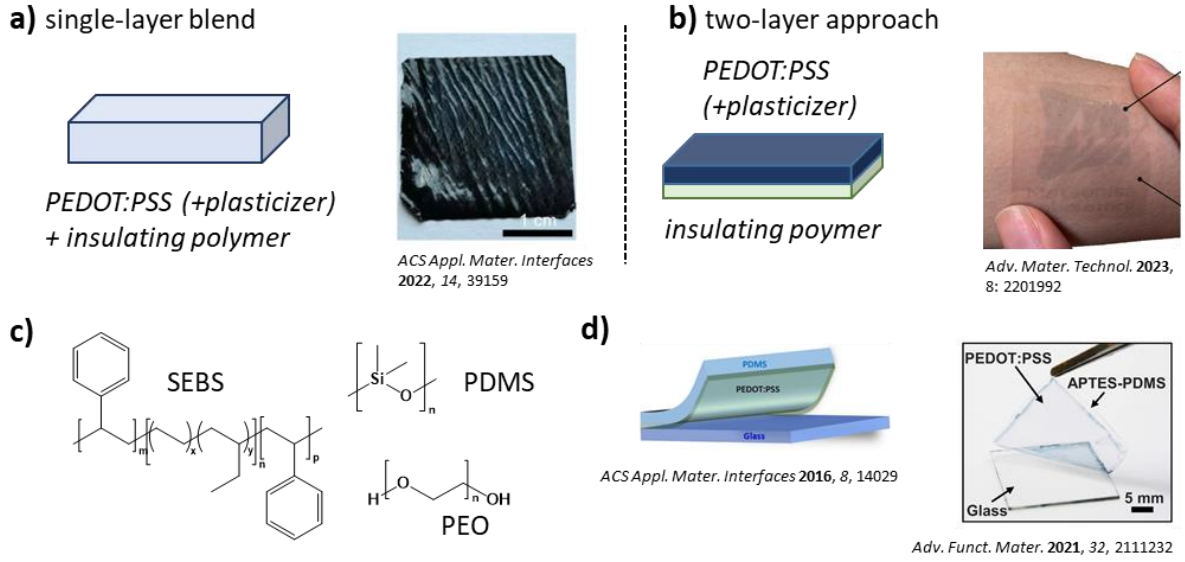

***Figure 1.5**: **a)** and **b)** Comparing single-layer blends and two-layer approach for stretchable electronics. Literature examples adapted from a) [99] and b) [67]. **c)** Chemical structures of commonly employed insulating polymers in stretchable electronics (SEBS, PDMS and PEO). **d)** Transferring PEDOT:PSS thin films onto stretchable substrates. Images adapted from [2] (left) and [70] (right).*

So far, several crucial aspects have been discussed to enable the use of PEDOT:PSS in stretchable electronics. This includes the incorporation of additives to modify both its electrical and mechanical properties and the selection of an appropriate insulating polymer, which is typically used as the supporting substrate, as well as the sample design. With these foundations in place, the next step is to investigate the electrical performance of PEDOT:PSS under mechanical strain.

1.2.4 Electrical Performance under Strain

Different types of deformations can be (electronically) studied, such as bending[69,100,101] and stretching, but this thesis will focus solely on the process of stretching. 'Stretchable' relates to a material's ability to endure strain—materials with higher fracture strain are considered more stretchable[36].

Furthermore, conducting materials can either retain/ improve or lose their electrical properties when subjected to strain. Devices and materials that maintain their electrical performance under strain are of greater commercial and scientific interest and, therefore, have been studied more extensively. Conclusively, a 'good' or 'enhanced' performance herein is defined as maintaining or improving electrical properties under strain. However, it is worth mentioning that materials that show a loss in conducting properties under strain have also found successful applications, e.g. as strain sensors[78,102]. Just like above, this thesis will focus on continuous conducting thin films, which are primarily deposited via spin-coating, drop-casting or transfer-printing.

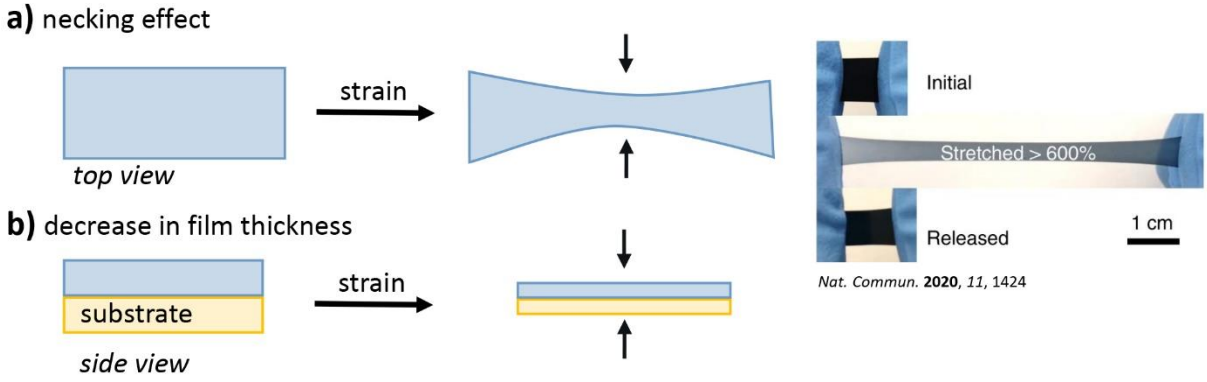

***Figure 1.6**: Geometrical changes under strain: **a)** necking effect (image adapted from [41]) and **b)** the expected decrease in film thickness with elongation.*

When evaluating the electrical performance of materials under strain, two key factors must be considered: geometrical changes and changes in the morphology of the conducting material. Typically, films are prepared as rectangular samples and then electronically analyzed using either the two-point method[64,80] or the four-point method[81,89]. Notably, four-point measurements, which are considered more accurate due to the elimination of contact resistances[103], are generally conducted on unstrained samples, whereas two-point measurements are used for samples while they undergo straining. When subjecting a rectangle sample to strain, changes in the sample length (L), width (W) and thickness (t) will occur. These changes lead to two challenges, shown schematically in **Fig. 1.6**: **a)** the necking effect, where the central portion of the examined film narrows significantly, causing the originally rectangular shape to take on a more dog-bone-like form. And **b)** the difficulty of accurately measuring changes in film thickness of the conducting layer, especially in two-layer systems. Basic theory predicts that the film thickness decreases upon elongation[104], which has been observed experimentally[105–107]. If the exact change in thickness is known, the material's conductivity (σ) (under strain) can be calculated, using the following equation and ignoring the necking effect:

$$\sigma = \frac{L}{R \cdot A} \tag{1.1}$$

with the resistance R and the area A ($= t \cdot W$). From this equation it also becomes evident that an increase in conductivity means a decrease in resistance and vice versa. However, when it is not possible to determine the conductivity, alternative methods such as measuring sheet resistance (R_S) or tracking the change in resistance relative to the initial value (R/R_0) can be used. The latter is most commonly employed.

From geometrical changes only, an increase in resistance upon strain is excepted, which can be expressed using the following equation[41,57,64–66,80]:

$$\frac{R_G}{R_0} = \frac{(1 + \varepsilon')}{(1 + \nu_1\varepsilon')(1 - \nu_2\varepsilon')} \tag{1.2}$$

with the resistance change R_G/R_0 according to the geometrical shape change, the fractional strain ε' and the Poisson ratio of the underlying substrate ν_1 as well as the conducting layer ν_2. The Poisson's ratio is a measure to describe the deformation of a material in response to applied loading[104]. Of course, this equation cannot be applied to single layer blends but only to two-layer systems. This theoretical line (green line in **Fig. 1.7a**) is oftentimes employed to get a better understanding of the overall electrical performance under strain and to discriminate between geometrical and morphological contributions. However, determining the Poisson ratios can be challenging, as the materials used are often modified in some way (such as plasticization), making it difficult to rely on standard literature values. Furthermore, the Poisson ratio might differ for thick films (for its determination) and very thin films (applications).

The second factor influencing electrical performance under strain are morphological changes in the organic semiconductor. Some of these changes can enhance performance, while others may have a negative effect. One enhancing factor is chain alignment—a process where polymer chains reorganize and align with the direction of strain when elongated[108]. This phenomenon is not unique to conjugated polymers but occurs in polymers with the 'right' chemical characteristics, such as hydrogen bonds[109–111]. In other fields, this process is referred to as strain-induced crystallization[111].
For conjugated polymers, the principle of chain alignment is schematically illustrated in **Fig. 1.7b**. While the scheme in **Fig. 1.7b** is not specific to PEDOT:PSS, it visualizes the general alignment process: the semi-crystalline domains (that enable charge transport) are randomly orientated before straining and re-organized because of the mechanical strain. In conjugated polymers, chain alignment ideally results in tighter packing of the polymer chains, which facilitates better charge transport. The factors influencing charge transport in organic semiconductors, discussed in **Section 1.2.1**, also apply here. Theoretically, greater strain should lead to more chain alignment[108], improving performance. This also means that the organization within the polymer ought to be controllable via the amount of applied strain. When designing the molecular structure of conjugated polymers for stretchable electronics, it is exactly this chain alignment that scientists (chemists) usually aim for to maintain or improve the electrical performance under strain. Furthermore, mechanical strain is one of the few methods to induce such organization in materials in their solid state[108].
Macroscopically, chain alignment is evidenced by a reduction in electrical resistance, while on a microscopic scale, it can be tracked using techniques such as AFM, UV/vis spectroscopy and grazing-incidence wide-angle X-ray scattering (GIWAXS)[108]. Strain-induced chain alignment has been observed in PEDOT:PSS[63] as well as other conjugated polymers[46,105,112,113].

Factors impairing conductivity include the formation of buckles[80] and cracks (see **Fig. 1.7c**). Crack formation is a natural limit of the elongation capabilities of conducting materials[7,9,64–66,80,88]. However, disruption of the crystalline (conducting) domains may occur before this happens, thus, also impairing charge transport[36]. This means that an increase in resistance does not necessarily have to be linked to the appearance of cracks.

Combining the conductivity enhancing and impairing factors results in the experimentally most frequently observed electrical behavior under strain, shown in **Fig. 1.7a** (solid dark-blue line)[40–42,64–66,88]. Initially, R/R_0 increases gradually up to a certain threshold, beyond which it rises sharply. Therefore, the experimentally observed line is usually divided into two regimes, which are associated with the factors introduced above: In the first regime we suspect or experimentally find chain alignment and in the second the disruption of the crystalline domains and appearance of cracks.

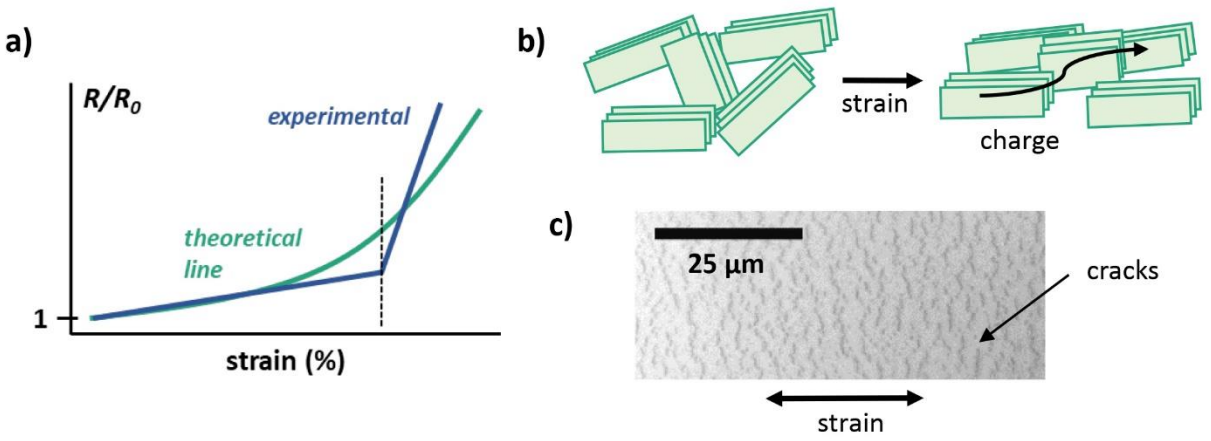

***Figure 1.7**: **a)** Electrical performance under strain: theoretical changes predicted due to geometrical effects (derived from **Eq. 1.1**; green line) alongside the most commonly observed experimental behavior (blue line). **b)** Schematic drawing of alignment of a semi crystalline polymer upon strain. **c)** Cracks emerging at higher strains, usually impairing the conductivity.*

Although the contributing factors to the electrical behavior under strain are straight-forward to describe, the reality is not quite as simple. Looking at the reported electrical behavior under strain of differently treated PEDOT:PSS, it can be seen that the choice of substrate[9,80,81,89] and the choice of plasticizer[40,42,56,63–66,76] have an influence on the electrical performance under strain. Furthermore, the film thicknesses (nanometers to micrometers in free-standing films as well as two-layer blends) and in two-layer systems the adhesion between the underlying substrate and the conducting thin film contribute as well[27].

Pristine PEDOT:PSS on various substrates in fact has been reported to exhibit a decrease in resistance upon elongation[80,81,89]. This has been attributed to different mechanisms, depending on the substrate employed. These include an irreversible growth of PEDOT grains[80,81] and promoted PEDOT:PSS adhesion to the substrate via van der Waals forces[89]. However, it needs to be pointed out that the initial conductivity of these thin films ought to be low, potentially having an influence on the electrical performance under strain. Ionic liquids (ILs) on the other hand have shown varying effects on the conducting properties of PEDOT:PSS under strain – while some studies suggest a conductivity boost[63], others reported moderate electronic performances[64–66]. Blends of PEDOT:PSS with elastomers show good ductility but moderate electrical properties, most likely owing to the insulating properties of these elastomers within the blend[14,42,56,76]. Furthermore, these blends have also been reported to phase segregate[76]. Some small organic plasticizers have been reported to improve conductivity upon elongation[40], while others, such as DMSO, have not[80]. One conclusion that may be drawn is that maintaining higher initial conductivities under strain appears to be more difficult than maintaining lower ones. This seems logical, as highly conductive PEDOT:PSS tends to be more crystalline, making it inherently more brittle and prone to damage when stretched.

Literature on PEDOT:PSS for stretchable and flexible electronics can be found in [37], a review on chain alignment in polymeric organic semiconductors (not PEDOT:PSS-specific) in [108] and a review on the highly debated effects of ILs in PEDOT:PSS in [60].

1.3 Stretchable Organic Electrochemical Transistors

OECTs are powerful devices for translating biological signals into electrical ones and vice versa. To ensure seamless contact with the human body, increasing research efforts are directed towards the development of stretchable OECTs. Therefore, this chapter discusses the operating principle of an OECT and engineering strategies for manufacturing stretchable devices. Furthermore, challenges and trade-offs will be discussed. Finally, the incorporation of strategies towards stretchable device into stretchable OECTs is evaluated. While the previous section (**Section 1.2**) covered chemical and morphological approaches, engineering strategies towards fully stretchable devices are discussed here.

1.3.1 Working Principle and Theoretical Background of OECTs

Since their discovery by White, Kittlesen and Wrighton in 1984[114], OECTs have garnered increasing research interest. Generally speaking, OECTs are particularly appealing for mobile sensing applications in close contact with the human body due to their low operating voltages (<1 V)[20], which furthermore makes them operational in aqueous environments[115]. In addition to this, OECTs offer easy processability[116] and the ability to interface seamlessly with biological environments[117].

An OECT comprises an organic semiconductor (commonly PEDOT:PSS), an electrolyte and electrodes (source, drain and gate). A schematic representation of an OECT is shown in **Fig. 1.8a**. To operate an OECT, a voltage is applied between the gate and the source, which drives ions from the electrolyte into the organic semiconductor film. This process alters the doping state of the film, thereby modulating the number of charge carriers in the channel[20]. This modulation can be monitored by applying a voltage between the source and the drain and measuring the drain current through the channel. OECTs share similarities with organic field-effect transistors (OFETs), and their operation is often compared. However, unlike OFETs, where charge modulation is restricted to the semiconductor interface, OECTs exhibit charge modulation throughout the bulk of the semiconductor[20]. This bulk modulation leads to several advantages, including high transconductance, large capacitance values and low operating voltages (<1 V)[118]. To realize OECTs, the channel material must be capable of conducting both electrons and ions, classifying it as a organic mixed ionic and electronic conductor (OMIEC). The most widely used OMIEC is PEDOT:PSS; however, various other materials have been explored for OECT applications. Examples include poly(6-(thiophene-3-yl)hexane-1-sulfonate)tetrabutylammonium (PTHS)[119,120] and poly(2-(3,3'-bis(2-(2-(2-methoxyethoxy)ethoxy)ethoxy)-[2,2'-bithiophen]-5-yl)thieno[3,2-b]thiophene (p(g2T-TT))[118,121,122].

OECTs can operate in either depletion or accumulation mode, depending on the channel material. When PEDOT:PSS is used, the device operates in depletion mode and is in the "ON" state by default, allowing charge to flow when a voltage (between source and drain) is applied. Applying a voltage between the source and gate switches the device off by driving cations from the electrolyte into the film. These cations neutralize the negatively charged PSS chains, extracting positive charge carriers from PEDOT at the drain. This process is illustrated in **Fig. 1.8a**. The interaction between PSS chains and cations is also responsible for the device's volumetric capacitance[123]. In contrast, materials such as p(g2T-TT) and PTHS operate in accumulation mode, where the device is switched on by applying a gate voltage. Accumulation-mode OECTs are increasingly favored due to their lower power consumption compared to depletion-mode counterparts[105].

Thanks to the numerous advantages provided by OECTs, flexible and stretchable applications have been developed, including soft implants[16], health monitoring devices[105], biosensors[11,124], neural interfaces[125,126] and neuromorphic devices[23,24]. These sensing applications usually rely on modifying either the gate or the channel to achieve desired functionalities[124,127,128].

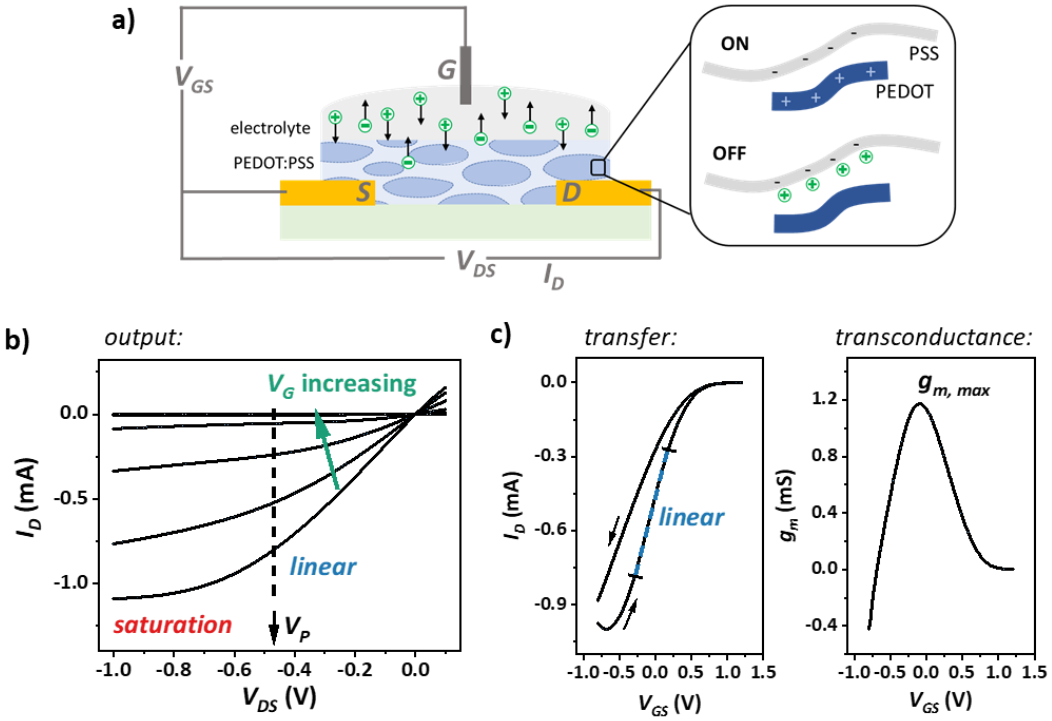

***Figure 1.8**: **a)** Typical OECT architecture, including source (S), drain (D), electrolyte and gate (G). Schematic drawing of ion diffusion upon switching off an OECT that employs PEDOT:PSS as a conducting layer. **b)** Output curves of an OECT operating in depletion mode. Linear and saturation regime as well as pinch off voltage are indicated. **c)** Transfer curve and transconductance of an OECT operating in depletion mode. The linear regime, employed to fit the Bernards-Malliaras model, is indicated. The transconductance is determined as the derivative of the forward sweep of the transfer curve.*

OECTs operate in two regimes, namely the transient and the steady regime. In the transient regime, the channel has been charged with ions, but the (de-)doping (depending on the material used) is still on-going. In the steady state, the channel has been charged with ions and (de-)doping no longer occurs. To evaluate the steady-state characteristics of an OECT, transfer and output curves are usually recorded[18,20,129]. Typical output characteristics of a depletion mode OECT are shown in **Fig. 1.8b** and transfer characteristics in **Fig. 1.8c**, left. To record output curves, the gate-source voltage (V_{GS}) is kept constant, while the source-drain voltage (V_{DS}) is swept, and the corresponding drain current (I_{DS}) is measured. In the output curve, the pinch-off voltage (V_P) marks the transition between the linear region—where the drain current increases linearly—and the saturation region, where the current saturates[18]. These linear and saturation regions are highlighted in **Fig. 1.8b** and **c**. To record transfer curves, the process is reversed: the source-drain voltage is held constant while the gate voltage is swept. From the transfer curve, key figures of merit, such as the ON/OFF current ratio and threshold voltage (V_T), can be derived. The most commonly used metric, however, is the transconductance (g_m):

$$g_m = \frac{\partial I_D}{\partial V_{GS}} = \begin{cases} -\frac{WTt}{L}\mu C^* V_{DS}, & linear\ regime \\ \frac{Wt}{L}\mu C^* (V_P - V_{GS}), & saturation\ regime \end{cases} \tag{1.3}$$

, obtained as the derivative of the transfer curve (see **Fig. 1.8c**, right). The maximum of the transconductance ($g_{m,max}$) is usually taken as a reference of the OECT's ability to translate an ionic signal into an electrical one (also indicated in **Fig. 1.8c**, right). Generally speaking, a higher value indicates a higher modulation and better performance. However, comparing these values amongst one another is challenging, as the transconductance is dependent on the geometry (channel length (L), width (W) and thickness (t)) of the OECT channel. These margins are schematically indicated in **Fig. 1.9a**. The relationship between channel size and transconductance has been shown experimentally numerous times[126,130,131]. Nevertheless, the transconductance is a useful metric for OECTs because electronic and ionic charges move simultaneously within the device. This makes it difficult to easily extract the charge carrier mobility, as is typically the case with OFETs[118].

To gain a deeper understanding of the device physics of an OECT, modeling in both the transient and steady-state regimes is a common approach[132]. Among the various models reported, one of the earliest and most widely used is the Bernard-Malliaras (B-M) model, proposed in 2007[133]. This model addresses steady-state and transient behaviors separately and utilizes modeling techniques from OFETs due to their structural and functional similarities. The core assumption is that an OECT can be represented as coupled ionic and electronic circuits, illustrated schematically in **Fig. 1.9b**. Within this representation, the electronic circuit is represented by a resistor (R) and the ionic circuit by a capacitor (C) and a resistor in series. For simplicity, the model assumes that the charge carrier mobility is constant. It is noteworthy that this assumption may not be true for conjugated polymers as their mobility depends on factors such as temperature or charge carrier concentration[134–136]. However, this assumption works well as an approximation. Derived primarily for p-type semiconductors, the final equation for the drain current I_D of a depletion-mode OECT is defined as:

$$I_D = \begin{cases} \frac{G}{V_P}\left(V_P - V_{GS} + \frac{1}{2}V_{DS}\right)V_{DS}, & linear\ regime \\ \frac{G}{2V_P}(V_P - V_{GS})^2, & saturation\ regime \end{cases} \tag{1.4}$$

with the conductance G, pinch-off voltage V_P, gate-source voltage V_{GS} and the drain-source voltage V_{DS}. G and V_P are defined as:

$$G = \frac{Wt}{L} q\mu p_0 \tag{1.5}$$

and

$$V_P = \frac{qp_0}{C/_V} \tag{1.6}$$

with

$$\sigma = q\mu p_0 \tag{1.7}$$

with the elementary charge (q), charge carrier mobility (μ), initial charge carrier density (p_0), capacitance (C) and the volume (V). The capacitance over the volume gives the volumetric capacitance (C^*). By fitting the linear region of the experimentally recorded drain current (I_D) from the transfer curve using the corresponding equation from **Eq. 1.3**, G and V_P can be extracted. The fitted area is indicated in blue in **Fig. 1.8c**, left. Subsequently, using **Eq. 1.5** - **1.7**, parameters such as conductivity and charge carrier density can be calculated[82], offering deeper insights into the OECT's operation characteristics.

As already discussed, the performance of an OECT depends on its geometry. However, looking at **Eq. 1.3**, it becomes evident that there also is a dependence on the material and the morphology of the OMIEC employed, which is expressed by the μC^*-product. This term, introduced as a figure of merit for OECTs by Inal et al.[118] in 2017, is composed of the charge carrier mobility (μ) and the volumetric capacitance (C^*). Ever since its introduction, the μC^*-product has proven to be a helpful and frequently-used parameter for benchmarking OECTs[137–140]. It can either be determined as a single value or by determining both parameters individually and multiplying them. To determine the μC^*-product as a whole, one approach is to model the transfer curve using the above-discussed B-M model. By re-arranging **Eq. 1.4** - **1.7**, the following relationship is obtained:

$$\mu C^* = \frac{G}{V_P}\frac{L}{Wt} \tag{1.8}$$

If the dimensions of the OECT are known, the μC^*-product can be calculated directly as the fitting the transfer curve yields G and V_P. Alternatively, the μC^*-product can be determined by plotting the $g_{m,max}$ of OECTs with differently sized channels against $W \cdot t/L$. This should yield a straight line and the slope then gives the μC^*-product[118]. To determine each parameter independently, the charge carrier mobility can be measured through methods such as the determination of the carrier transit time[133] or by electrochemical impedance spectroscopy (EIS)[141]. The (volumetric) capacitance can be derived employing EIS[126,138,142–144], cyclic voltammetry[145] or chronoamperometry[122]. Regardless of whether the μC^*-product is calculated directly or derived by multiplying its individual components, both approaches have been shown to be in good agreement[118].

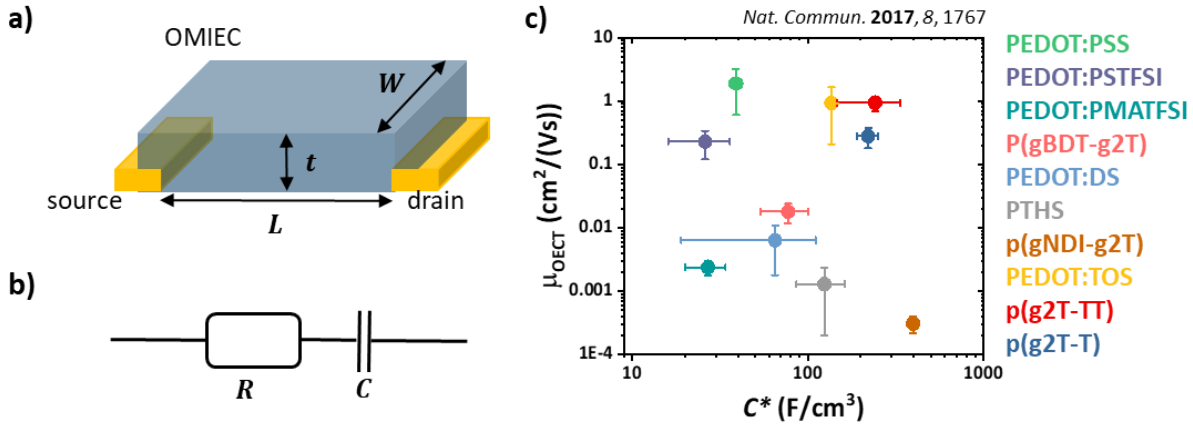

***Figure 1.9**: **a)** Schematic drawing of an OMIEC bridging source and drain, creating an OECT channel. The channel length (L), width (W) and thickness (t) are indicated. **b)** The equivalent circuit used by Bernards and Malliaras models the electrolyte as resistor (R) in series with a capacitor (C). **c)** Charge carrier mobility (μ) against the volumetric capacitance (C^*) for various OMIECs. Image reproduced from* [118].

While determining the μC^*-product as a whole may be experimentally easier, determining each parameter individually offers valuable insights into the electronic and ionic circuits that contribute to overall OECT performance. For example, PEDOT:PSS exhibits high charge carrier mobility (typically around 1 $cm^2/(Vs)$) but relatively low volumetric capacitance (approximately 30 F/cm^3), whereas p(g2T-TT) demonstrates both high charge carrier mobility and high volumetric capacitance[118] (see **Fig. 1.9c**). This understanding enables targeted molecular design of OMIECs to optimize device functionality.

Factors affecting charge carrier mobility, discussed previously (**Section 1.2.1**), are generally well-researched. In contrast, understanding of the volumetric capacitance and ionic movement within these OMIECs remains limited[137], despite its significance. One reason why the ionic motion is highly relevant is because, along with device geometry, it often represents the limiting factor for the switching speed of an OECT[22]. This in turn becomes relevant when envisioning applications such as medical devices that might call for a fast response[22,146,147]. For electrolytes, almost any ion can be used. Most commonly, an aqueous sodium chloride solution (NaCl), commercially available as phosphate-buffered saline (PBS), is employed[25,148,149]. However, ionic liquids[150,151] and solid-state electrolytes[152,153] are also viable options that can be selected depending on the intended study design or application. This diversity is another reason why OECTs are studied so frequently.

There are two factors influencing the ionic transport, which are the ions within the electrolyte themselves and the (molecular) nature of the OMIEC. For the electrolyte, it has been shown that the size (ionic radii[118,137,139,149]), charge and nature of the solvated ions, in case an aqueous electrolyte is used[118,149], are relevant. Furthermore, the salting-in and -out properties of the cations in aqueous electrolytes have been identified to contribute to the ability of the ions to penetrate the channel[137]. Colucci et al.[137] reported that cations with a higher channel swelling/ salting-in ability (according to the Hofmeister series[154]) result in a more efficient de-doping of PEDOT:PSS channels. In p(g2T-TT)-based OECTs, larger ions have been suggested to move slower, thus resulting in delayed penetration and transport, which caused a larger hysteresis in the transfer curves[58]. And lastly, the performance of OECTs was found to depend on the swelling behavior of the same, caused by the ions within the electrolyte[122,155,156]. Furthermore, the swelling nature of the OMIEC naturally depends on its molecular design, including factors such as the side-chains[122,155].

The influence of the morphology of the OMICE on the electric and ionic transport is particularly relevant for PEDOT:PSS, which is frequently chemically treated to enhance conductivity and consequently undergoes significant morphological changes (see **Section 1.2.2**). Therefore, the values for mobility and volumetric capacitance can vary depending on the specific treatment applied. Even worse, they may be competing with one another. This has been shown by Rivnay et al[51]. Studying EG-treated PEDOT:PSS thin films, it was found that an increase in charge carrier mobility comes at the expense of the volumetric capacitance. This was attributed to closer packing of the polymer chains with increasing EG-content[51]. Such trade-offs have been demonstrated for other OMIECs as well[155].

Concluding, OECTs are exciting but also challenging devices to study due to their coupled electric and ionic motion. However, employing modelling approaches and figures of merit such as the μC^*-product yields insights into the same. This is essential for deriving intelligent molecular design strategies of the OMIEC, which will in turn ensure well-working devices. Next, engineering strategies for achieving stretchable electronics and their application in OECTs will be explored.

For reviews on the basic principles and device physics of OECTs, please refer to [18,22,132].

1.3.2 Fabricating Stretchable Devices

One of the central challenges in developing and fabricating stretchable electronic devices is ensuring that all functional components—such as electrodes and interconnects—retain their performance under mechanical strain. Electronic devices often consist of multiple stacked layers, introducing both manufacturing and morphological complexity. Since each layer may respond differently to deformation, establishing clear design principles and correlating them with overall device performance becomes particularly difficult. To address these challenges, a range of engineering strategies have been developed in recent years to complement the previously discussed chemical and morphological approaches (see **Section 1.2**). Although not all of these methods have been applied to OECTs to date, they provide a valuable set of tools for improving mechanical robustness.

When envisioning stretchable OECTs, particularly those intended for use on or within the human body, an in-plane configuration would be the most practical choice as this layout would ensure consistent contact with the targeted tissue or surface. As described previously, a typical conventional OECT features an OMIEC bridging the source and drain electrodes—naturally forming an in-plane design unless a vertical OECT (vOECT) is specifically engineered[157]. Often, an Ag/AgCl electrode is used as the gate, immersed in a PBS solution, which creates an out-of-plane arrangement (as depicted in **Fig. 1.8a**). The use of an Ag/AgCl electrode avoids a voltage drop at the gate/electrolyte interface[158]. However, many rigid OECT examples exist where the gate is positioned in the same plane as the source, drain and OMIEC, realizing a fully in-plane architecture[11,142].
In general, but especially for in-plane OECTs, the structuring of thin films is crucial for the fabrication of OECTs. Therefore, strategies to pattern PEDOT:PSS are discussed in a first step. Subsequently, a general overview of physical strategies to protect stretchable electronics from stain-induced damage is given.

Creating Structures

To realize any type of (stretchable) electronics, depositing (conducting) materials in designated areas is essential. In other words, for PEDOT:PSS this means it needs to be patterned in some way. To achieve this, there are three main approaches. The first involves creating a uniform thin film, typically through spin-coating, which is then patterned afterward. This approach, known as post-deposition treatment, includes techniques like (photo)lithography[159] and multi-step etching processes[160]. The second method involves depositing PEDOT:PSS directly onto designated areas from the start, bypassing the need for later patterning. Direct patterning strategies include techniques such as screen printing[161], inkjet-printing[52,162] and electrochemical deposition[163,164]. Another approach within this category involves attaching a mask onto a flexible substrate prior to the spin-coating of PEDOT:PSS[9,70]. And the third approach is to employ chemistry. One way of doing is, is by introducing photopolymerizable additives into PEDOT:PSS, using photomasks and irradiation, followed by washing to produce micron-sized PEDOT:PSS patterns[98,165,166]. Alternatively, fine-tuning the substrate's surface chemistry can ensure PEDOT:PSS adheres only in designated areas[167]. Some of the presented strategies are directly applicable to deformable substrates, while others, such as multistep etching processes are usually not. Therefore, the transfer of the patterned structures onto a flexible and stretchable substrate potentially needs to be realized as well. For this, please refer to **Section 1.2.3**.

Physical Approaches to Protect Conducting Materials from Strain-Induced Damages

As discussed earlier, a key challenge in the development of stretchable electronics is to achieve both conductivity and deformability within the active material[26,30,37,38]. In addition to adapting the molecular or chemical properties of the active material itself (**Section 1.2**), intelligent device design can be used to protect the (semi)conductor against strain-induced damage. In the field of stretchable electronics, common strategies for physically protection include the buckling technique[7,9,168], meshes[107,169–171], employing patterned substrates[172–174] and wavy interconnects[173,175] (see **Fig. 1.10**). Another, fifth approach, is the ridged island technique. This technique stands out from the other approaches, as parts of the device do remain unstrained or are only deformed to a small extent[176]. Although this a well-established approach within the field of stretchable electronics[176,177], it has not been explored for OECTs specifically to the best of my knowledge. This section will cover a broader range of materials. This is because in stretchable OECTs it may only be the channel that is made of PEDOT:PSS (formulations). The electrodes on the other hand are often made of metals.

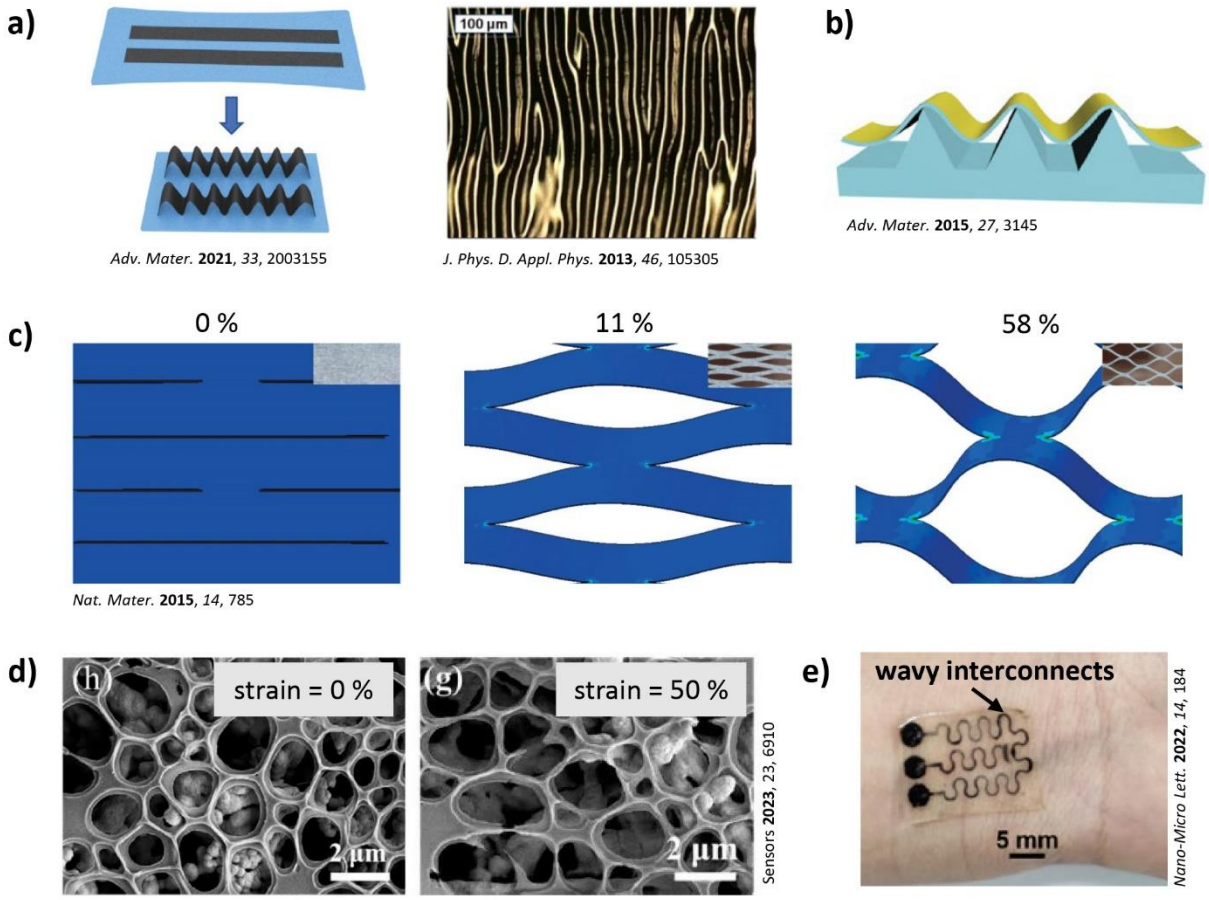

***Figure 1.10**: Engineering approaches towards stretchable devices: **a)** Buckling: Pre-straining the underlying substrate, images from [59] and [168] (buckled silver film). **b)** Patterned substrates: Schematic drawing of patterned PDMS substrate with attached conducting thin film. Image from [178]. **c)** Mesh: Kirigami structure and its deformation under strain, image from [179]. **d)** Mesh: Scanning electron microscopy (SEM) images of porous P3HT/ SEBS network at 0 % and 50 % strain, images adapted from [169]. **e)** Wavy interconnects Stretchable OECT with wavy interconnects; image adapted from [173].*

The first technique discussed is the *buckling* technique, also known as longitudinal waves and pre-straining (pre-stretching). This process is shown in **Fig. 1.10a**: an elastomeric substrate is pre-stretched,

and a conducting thin film is then deposited onto it[168]. Upon releasing the substrate, the film forms longitudinal buckles, as seen in **Fig. 1.10a**. Using this technique, the conducting layer typically retains its electrical performance up to the initial pre-strain limit, making it ideal when preserving stable electrical performance under strain is essential since the conductor does not undergo morphological changes. However, the buckling technique may prevent seamless contact with the area of interest as the material loses its uniformity. An alternative pre-straining method involves depositing the conductive layer and then cyclically stretching and relaxing the entire system, which has also demonstrated good strain performance[7,9].

Another approach to achieving non-flat but still continuous conducting films is through the use of *patterned substrates*, as schematically shown in **Fig. 1.10b**[172–174]. When the conducting film is deposited onto a patterned substrate, it adopts the underlying pattern, resulting in a structured film.

To alter the semiconductor used itself, using a type of *mesh* briefly mentioned in an earlier section (**Section 1.2.2**) is a promising way. In general, a mesh is a structure with different openings[59]. One type of openings are systematic cuts, known as a Kirigami structure[179,180] (see **Fig. 1.10c**). Another common structure are porous structures[58], sometimes called honeycomb structures. The first is created physically, while the latter can be created by intelligent evaporation of solvents, creating holes in a previously uniform thin film[107,169–171] (**Fig. 1.10d**). These structures show high strain tolerance due to their out-of-plane deformability (buckling)[59,107]. One sub-category of the mesh structures are intentional micro cracks, created by depositing gold onto a stretchable substrate following a specific procedure[106].

And lastly, within stretchable electronics it is important to establish reliable contact with the area of interest during deformation. In OECTs, this would be the channel. The simplest approach is to create straight conductive stripes, in contact with the named area of interest. However, as *serpentine patterns* were found to have a higher strain tolerance than continuous stripes, they are frequently employed[181–183]. An example is shown in **Fig. 1.10e**. The strain tolerance was found to depend on amplitude of the serpentines[183]. These wavy interconnects can be fabricated from various materials, including metals[175,181,183] and PEDOT:PSS[173].

Concluding, all these approaches allow to fabricate stretchable devices that maintain their performance well under deformation. However, they usually do not allow for structural analysis of the organic semiconductor involved. Additionally, the wide variety of techniques, combined with morphological adaptations, can complicate direct comparisons between devices.

A review on various strategies to employ PDMS as a stretchable substrate, including a wide range of physical approaches can be found here [184]. Another helpful review can be found here [59].

1.3.3 Stretchable OECTs

The development of stretchable OECTs is a young and emerging subfield that builds on the broader field of stretchable electronics. According to the WOS, the earliest publication on stretchable OECTs dates back to 2012[185]. Within this domain, a distinction can be made between intrinsically stretchable OECTs and their more conventional counterparts. Unlike conventional stretchable OECTs, which often rely on external structural or engineering solutions to reduce damage from mechanical strain, intrinsically stretchable OECTs are specifically designed to sustain stable performance during deformation without such supports, e.g. through chemical approaches. While techniques such as

structural engineering from the broader field of stretchable electronics have been adapted for conventional stretchable OECTs, research into (intrinsically) stretchable OECTs remains relatively sparse. However, early studies highlight the promise of leveraging these strategies for OECTs. In some cases, these approaches have been complemented by morphological adaptation of the OMIEC (see **Section 1.2**), further enhancing the device's mechanical resilience.

Tab. 1.1 summarizes the most important publications, organized based on the channel material (OMIEC) used. As expected, the main choice is PEDOT:PSS[7,8,174,175,186–191,9,58,90,97,101,106,172,173], however, p(g2T-TT)-[58,105,170,192], P3HT-[70,169,170,193] as well as DPP-based[107] stretchable OECTs have been reported as well. To enhance mechanical durability, various engineering approaches to protect the channel from deformation have been explored. These include wavy interconnects[173,175], intentional micro cracks in the metal electrodes[106], patterned substrates[172–174] and buckling. For the latter, either the full device is pre-strained[7,9] or only the supporting substrate to buckle the organic semiconductor[8,173,186,189]. In addition to these engineering strategies, chemical and morphological adaptations have played a vital role, including different kinds of supporting substrates[7–9,173], organic semiconductors[58,105,107,173] as well as diverse morphologies of these semiconductors[58,107]. And lastly, as electrolytes, either ionic gels[70,188] or, most frequently, NaCl in an aqueous solution[186,187] are used.

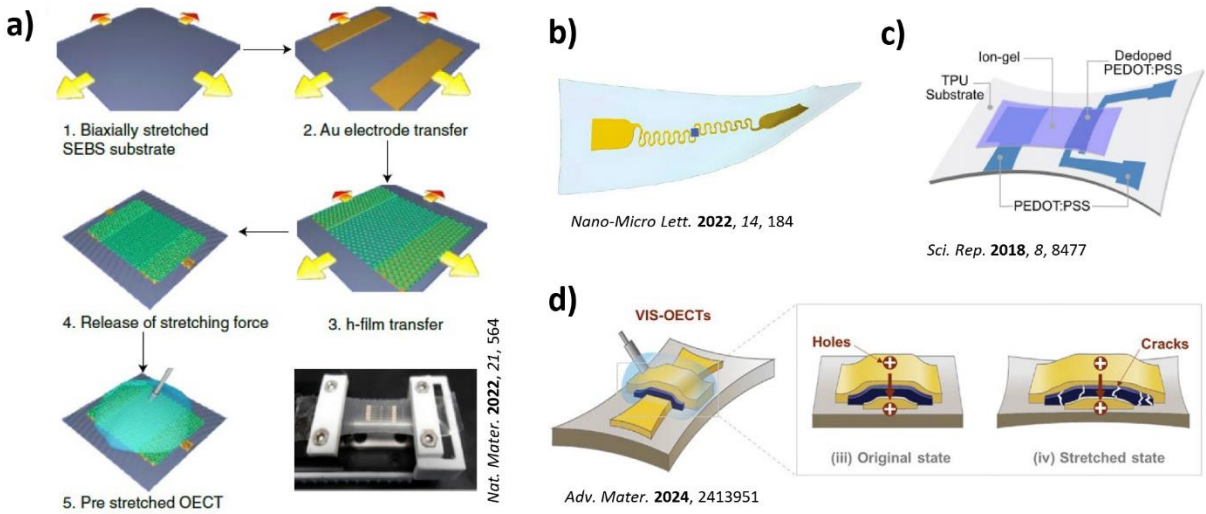

***Figure 1.11**: **a)** Chen et al.[107] fabricating stretchable devices by biaxially pre-stretching the underlying substrate as well as employing a honeycomb OMIEC. **b)** Machiori et al.[175] utilized wavy interconnects. **c)** and the intrinsically stretchable OECT of Wang et al.[173] is composed of PEDOT:PSS in combination with a solid state electrolyte. **d)** Vertical intrinsically stretchable OECT, introduced by Dai et al.[157].*

Chen et al.[107] for instance employ multiple of the afore-mentioned principles simultaneously: The underlying substrate is pre-strained biaxially and the channel material made of honeycomb poly(2,5-bis(2-octyldodecyl)-3,6-di(thiophen-2-yl)-2,5-diketo-pyrrolopyrrole-alt-2,5-bis(3-triethyleneglycoloxy-thiophen-2-yl) (DPP-g2T). Their OECT is shown in **Fig. 1.11a** and exhibited an almost unchanged electrical performance up to 100 - 150 % strain[107]. Machiori et al.[175] on the other hand employ solemnly wavy interconnects (**Fig. 1.11b**) and Wang et al.[173] none of the above-mentioned engineering approaches (**Fig. 1.11c**). These examples underscore the diversity within the field of stretchable OECTs. Interestingly, when pre-stretching either the full device or supporting substrate, a well-maintained OECT performance under strain can be achieved[8,9,58,172,173,186,189]. However, when no pre-strain is applied, the OECT performance tends to decrease with strain[97,175,187]. Lastly, the recent work by Dai et al.[157] is worth highlighting, as it introduced an intrinsically stretchable vertical OECT. Through a vertical configuration, the authors successfully created a device that maintained

functionality under strain, even in the presence of cracks. The key innovation lies in directing charge carriers to travel vertically, bypassing the cracks rather than moving in-plane with them. A schematic drawing of the vertical OECT is shown in **Fig. 11d**.

Despite initial progress in the development of (intrinsically) stretchable OECTs, a comprehensive and fundamental understanding as well as standardized design guidelines remain largely absent. This gap stems from the vast amount of available materials and fabrication techniques combined with a relatively limited body of literature. A key factor in advancing the field is understanding the complex relationship between morphology, device geometry and electrical performance under mechanical strain. However, when physical engineering strategies are employed to shield the OMIEC from strain, it becomes difficult to isolate and analyze how strain-induced morphological changes within the OMIEC impact device performance. Gaining this fundamental insight is essential for establishing robust design principles for intrinsically stretchable OECTs. Moreover, to date, no studies have systematically examined geometric transformations under strain, despite their evident occurrence. Closing these knowledge gaps is critical for driving the evolution of stretchable OECTs and enabling their practical application in real-world scenarios.

For further reading on the design principles of flexible OECTs, please refer to [194].

Table 1.1: Overview over stretchable OECTs.

channel material	added compounds	channel contacted with	substrate	electrolyte	strain tolerance	$g_{m,\,max}$ @ 0% strain	method applied	Ref.
PEDOT: PSS-based	+ PEG + Capstone FS-30 + glycerol	PEDOT:PSS as well/ Au	PDMS	NaCl in H_2O	45 %	0.1 mS	buckling (45 %, full device)	[8]
	+ PEGDE + glycerol + GOPS + DBSA	vapour deposited nano Au (20 nm)	SEBS	ionic gel (solid state)	50 %	~ 1.3 mS	-	[90]
	+ Li:TFSI	same as channel	gelatin + glycerol (partially structured)	sodium nitrate in organohydrogel electrolyte (solid state)	up to 100%	12.7 mS	wavy interconnects, patterned substrate, buckling	[173]
	+ glycerol + Capstone FS-30	Cr/ Au (evaporated)	PDMS	NaCl in H_2O	30 %	~1 mS	buckling (30 %, substrate)	[186]
	+ PAAMPSA + IL	AgNW; carbon nano tubes as gate	SEBS	EMIM:OTF in PVDF-HFP (solid state)	100 %	~13 mS	-	[174]
	+ Capstone FS-30 + GOPS + EG + xylitol	Cr/ Au	PDMS (structured)	NaCl in H_2O	30 %	NA	patterned substrate, buckling (40 %, substrate)	[172]
	+ EG + DBSA + GOPS	aluminum (waves)	PDMS	KH_2PO_4	38 %	6.5 mS	wavy interconnects	[175]
	+ Capstone FS-30	Ti (4 nm)/Au (25 nm)	PDMS or paralyene/ PDMS	NaCl in H_2O	30 %	0.4 mS	-	[7]
	+ glycerol + DBSA	same material	TPU	stretchable gel (solid state)	50 %	15 mS	buckling (50 %, full device)	[9]
	+ IL (Li:TFSI and one other)	Au	SEBS	NaCl in H_2O	30 %	0.3 mS	-	[187]
	PEG400 + DBSA + divinyl sulfone	Ag NW network	SEBS	EMIM:TFSI in PVDF-HFP (solid state)	30 %	~25 mS	-	[188]

Table 1.1: Continued.

channel material	added compounds	channel contacted with	substrate	electrolyte	strain tolerance	$g_{m,\,max}$ @ 0% strain	method applied	Ref.
PEDOT:PSS-based	+ EG + DBSA + GOPS	Au	parylene/ acrylic elastomer	NaCl in H_2O/ in cross-linked PVA (glycerol soaked)	30 %	~1.2 mS	buckling (30 %, substrate)	[189]
	purchased formulation w/ organic alcohols	Ag ink (source/drain) /AgCl (gate)	TPU	PVA-based, containing NaCl (solid state)	60 % and 150 % (2 layouts)	1.04 mS	-	[97]
	+ zonyl	Cr/ Au (sputtering)	PDMS	NaCl in H_2O	50 %	NA	patterned substrate	[101]
	+ DBSA + GOPS + EG	Au with intentional microcracks	PDMS	NaCl in H_2O	140 %	0.54 mS	mesh	[106]
	PEDOT:PSS aerogel films	PEDOT:PSS	PU	IL in polyacrylamide (solid state)	100 – 200 %	0.31 mS	mesh (porous), buckling (50-200 %, substrate)	[58]
	+DBSA + EG	Au thin film	PDMS	NaCl in H_2O	60 %	NA	mesh (micro cracks)	[190]
	+ PEI + glycerol + GOPS + DBSA	same material	TPU	ion gel (not specified)	50 %	0.15 mS	-	[191]
p(g2T-T)-based		NW (Au-based)	PDMS	NaCl in H_2O	100 %	4.2 mS	-	[105]
	+ tissue-adhesive polymer (blend)	Au (micro-cracked)	TPU	NaCl in H_2O	100 %	~1.2 mS	interconnects buckled	[192]
	p(g2T-T) areogel	PEDOT:PSS	PU	IL in polyacrylamide (solid state)	100 – 200 %	0.27 mS	mesh (porous), buckling (50 - 200 %, substrate)	[58]
	+ SEBS (porous)	Au	SEBS (porous)	NaCl in H_2O	50 %	*	mesh (porous)	[170]
P3HT-based	+ PDMS (blend)	PEDOT:PSS + Titron X-100	PDMS (modified)	EMIM:TFSI in PVDF-HFP (solid state)	30 %	NA	-	[193]
	+ PDMS (blend)	PEDOT:PSS + Titron X-100	PDMS (modified)	EMIM:TFSI in PVDF-HFP (solid state)	30 %	NA	-	[70]

Table 1.1: Continued.

channel material	added compounds	channel contacted with	substrate	electrolyte	strain tolerance	$g_{m,\,max}$ @ 0% strain	method applied	Ref.
P3HT-based	+ SEBS (porous)	Au	SEBS (porous)	EMIM:TFSI/ NaCl	50 %	1.51 mS	mesh (porous)	[169]
	+ SEBS (porous)	Au	SEBS (porous)	EMIM:TFSI	50 %	*	mesh (porous)	[170]
DPP-based	honeycomb	Au (transferred)	SEBS	KPF_6 in H_2O	30-140 %	2.47 mS	buckling (whole device), mesh (honeycomb)	[107]

*Please refer to the original publication. Due to its complexity, it cannot be summarized in a single symbol entry.

2. Motivation and Conceptual Design

Stretchable electronics, especially stretchable OECTs, hold immense potential, but face significant challenges that must be overcome to fully realize their capabilities. Partially already outlined in **Chapter 1**, these challenges can be categorized into three main areas: Processing challenges, the need for a fundamental morphological and electronic understanding of the system's behavior under strain and the integration of these insights into stretchable OECTs.
In this thesis, each of these aspects is addressed through three interconnected projects and discussed in three consecutive chapters (**Chapter 3** - **5**). Each chapter builds on the findings and techniques developed in the preceding chapter, forming a coherent flow. This is graphically illustrated in **Fig. 2.1**. The overarching focus of this thesis is to address these challenges, with the final aim of fabricating intrinsically stretchable OECTs and gaining a fundamental understanding of how strain affects their performance.

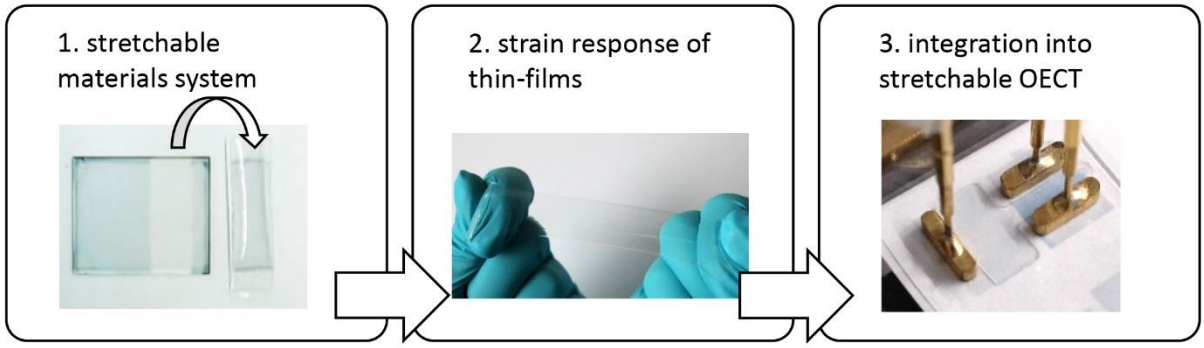

***Figure 2.1**: Conceptual framework of the findings presented in this doctoral thesis.*

To fabricate stretchable OECTs reliably, innovative strategies for patterning and depositing PEDOT:PSS onto stretchable substrates are crucial. Techniques such as inkjet printing and spin-coating show promise but require further adaptation and validation for specific systems. Moreover, selecting suitable materials for a given technique—or tailoring techniques to accommodate specific materials—poses an ongoing challenge. The wide range of available materials adds complexity to the optimization process. Additionally, developing methods that support various PEDOT:PSS treatments, enable large-area transfers and prevent delamination remains problematic. **Chapter 3** addresses these issues by introducing a transfer-printing technique for depositing PEDOT:PSS onto biodegradable PVA:glycerol substrates. The method's compatibility with diverse PEDOT:PSS treatments is demonstrated and validated through detailed morphological and electrical characterizations. Combined with a fast and reliable O_2-plasma-patterning process, this technique establishes a robust fabrication pathway for stretchable OECTs.

Efforts to fundamentally understand PEDOT:PSS's electrical and morphological response to strain come with multiple challenges. Within PEDOT:PSS the major bottleneck of the field (stretchability vs conductivity) is commonly managed through the use of plasticizers. However, tracing the effects caused by the plasticizers proves difficult for three main reasons. (i) additives/plasticizers tend to enhance both conductivity and stretchability simultaneously, making it challenging to distinguish their individual contributions, (ii) the use of multiple plasticizers in combination further complicates this differentiation and (iii) these interactions occur in the liquid phase before deposition, making it experimentally difficult to track morphological changes. This complexity underscores the need for detailed investigations to unravel these interactions and optimize performance.

Chapter 4 explores the effects of an organic plasticizer on the morphology and subsequently electrical properties of PEDOT:PSS using the transfer-printing technique introduced in **Chapter 3**. The findings reveal that concentration-dependent plasticizer diffusion from the substrate into the conducting layer prompts a rearrangement of PEDOT and PSS, resulting in better-connected PEDOT domains and enhanced conductivity. Moreover, this diffusion improves the material's electrical response to strain, offering valuable insights for optimizing PEDOT:PSS performance in stretchable applications.

Chapter 5 integrates the findings from **Chapters 3** and **4** into the development of stretchable OECTs. As research in this area is still in its infancy, the specific challenges facing stretchable OECTs remain loosely defined. However, it is clear that the previously discussed challenges must be addressed to achieve successful fabrication. While significant progress has been made over the past decade towards intrinsically stretchable OECTs, fundamental studies linking device geometry, morphological changes under strain and key OECT parameter and characteristics, remain scarce. **Chapter 5** aims to bridge these gaps by building upon the insights gained in earlier chapters. The influence of geometrical changes within the OECT on the device characteristics such as electrolyte resistance or turn-off voltage are studied in detail. Furthermore, the interplay between electric and ionic motion is examined, emphasizing how the channel material's response to strain impacts this interaction. The analysis reveals that charge transport becomes anisotropic under strain, while the volumetric capacitance consistently decreases.

Lastly, the set up (stretch station) developed within the scope of this thesis and employed for the electrical characterization under strain is introduced in a supplementary Chapter (**Chapter 7**), including experimental considerations and device details.

3. Transfer-Printing of Patterned PEDOT:PSS Structures for Bendable, Stretchable and Biodegradable Electronics

Chapter details

Authors:

Carla Volkert, Renan Colucci, Rüdiger Berger, Pol Besenius, Paul W. M. Blom and Ulrike Kraft

Reproduced with minor changes from:

C. Volkert, R. Colucci, R. Berger, P. Besenius, P. W. M. Blom, U. Kraft, 'Transfer-printing of patterened PEDOT:PSS structures for bendable, stretchable and biodegradable electronics'; *J. Mater. Chem. C* **2024**, *12*, 3865; https://doi.org/10.1039/d3tc04485h

Author contributions:

C. Volkert: Conception, planning and execution of all experiments, with the exception of the recording of some SFM images (recorded by Helma Burger; technician). Interpretation of the results and writing of the manuscript.

R. Colucci: Support in performing electrical measurements. R. Berger: Support in recording and analyzing the SFM-images. P. Besenius and P. W. M. Blom: Discussion on the concept and the results. U. Kraft: Supervision of the project. Discussion on the concept and the results and editing of the manuscript.

3.1 Abstract

The conductive polymer poly(3,4-ethylenedioxythiophene):poly(styrene sulfonate) (PEDOT:PSS) is of great interest for a variety of applications in flexible and stretchable electronics, due to its high conductivity, optical transparency, mechanical properties, commercial availability and biocompatibility. However, to advance novel applications on conformable substrates, the development of innovative and reliable methods for processing conductive polymers is vital. Here, a fast, dependable and easy PEDOT:PSS transfer-printing method onto flexible, transparent and biodegradable poly(vinylalcohol) (PVA):glycerol targets is presented. In contrast to previous work, this method neither depends on acid, nor doping, nor surface soaking treatments. Furthermore, this approach is compatible with common strategies to induce stretchability and increase the conductivity of PEDOT:PSS. To ensure the applicability to next-generation flexible and stretchable electronics, the electrical, morphological and adhesion properties before and after printing are characterized. Additionally, a straightforward methodology to pattern transfer-printable PEDOT:PSS structures is established, using an O_2-plasma treatment. Furthermore, the water-soluble targets allow for environmental-friendly disposal.

3.2 Introduction

Flexible and stretchable electronic devices and circuits offer high prospects for applications in mobile, wearable and on-skin electronics, personalized medicine and biomonitoring. Hence, enormous efforts are attributed to develop conformable devices such as biosensors[10], optoelectronic devices[2], organic field effect transistors (OFETs)[3,4], light emitting diodes (LEDs)[6] and organic electrochemical transistors (OECTs)[7–9]. To realize next-generation electronics, a change from rigid to flexible and stretchable components is required and calling for new device fabrication processes as well as flexible and stretchable electronic materials including substrates and (transparent) conductors. Additionally, defined structuring of the latter material is crucial to define electrodes and functional devices.

As a material the conducting organic polymer poly(3,4-ethylenedioxythiophene): polystyrene sulfonate (PEDOT:PSS) is a popular choice, due to its optical transparency, mechanical properties, high conductivity, commercial availability and biocompatibility[37,49,50]. It consists of positively charged PEDOT-chains and negatively charged PSS-chains. Within the polymer, PSS serves as a dopant and counter-ion for PEDOT and enables the dispersion of PEDOT in water which itself is water-insoluble. Pristine PEDOT:PSS films exhibit a conductivity of approximately 1 S/cm. Hence, various treatments, such as doping via polar solvents, strong acids or ionic liquids are commonly employed to increase the conductivity to hundreds or even thousands of S/cm[7,49,82]. Extensive research has been attributed to investigate the underlying mechanisms behind this increased conductivity of PEDOT:PSS. In general, the following factors are discussed to play a role in the conductivity enhancement: A change in the PEDOT-resonant structure from benzenoid to quinoid, a change in conformation from coil to extended-coil, a change in grain size, separation between PEDOT-rich and PSS-rich phases as well as secondary doping and charge screening effects[49,83].

In terms of flexible and stretchable substrates various materials such as polyethylene terephthalate (PET)[93], styrene ethylene butylene styrene (SEBS)[3,52] or polydimethylsiloxane (PDMS)[70] are commonly employed. However, the deposition of PEDOT:PSS thin-films e.g. through spin-coating on flexible plastic substrates faces difficulties for several reasons: First, the adhesion of PEDOT:PSS to hydrophobic flexible and stretchable substrates is generally poor[2], making it difficult to produce

uniform films and leading to delamination. In addition, flexible and stretchable plastic substrates are prone to be damaged by harsh treatments commonly employed to increase the conductivity of PEDOT:PSS, such as acid treatments[2].
An elegant approach to avoid these problems is transfer-printing, which allows e.g. acid washing and soaking on glass substrates prior to the transfer to the final soft substrates. The respective process involves lifting a spin-coated thin-film from a glass substrate and placing it onto a target substrate with or without the use of a transmission substrate[2,93–96]. To make transfer-printing successful, adjusting the PEDOT:PSS adhesion is key. It is possible to either reduce the adhesion on the donating substrate or increase it on the receiving substrate. For this purpose, (chemical) treatment of the PEDOT:PSS[2,92,94], the target substrate[70], or both simultaneously[93] are reported. Common treatments to increase the conductivity of PEDOT:PSS and simultaneously decrease its adhesion to the donating glass substrate include the addition of surfactants[92] and acid treatment of PEDOT:PSS films[2,94]. Treatments of the receiving substrate to increase the adhesion of PEDOT:PSS include chemical functionalization (e.g. of PDMS[70]) and the employment of hydrogen bonds. Combining different approaches allows the optimization of the adhesion at multiple steps. For example Fan et al.[93] performed a methanesulfonic acid-treatment on PEDOT:PSS films and furthermore spin-coated a PEDOT:PSS/D-sorbitol mixture on the receiving PET substrate to form hydrogen-bonds with the later on transferred PEDOT:PSS. All of these approaches are limited in their applicability as they depend on specific chemicals or treatments. To date, a widely applicable approach that enables the processing of variously treated PEDOT:PSS thin films on stretchable and flexible substrates is missing.

For the application of PEDOT:PSS as electrodes as well as active layer in functional electronic devices such as OECTs, patterned structures are crucial[98]. Common routes to structure PEDOT:PSS often require complicated protocols or lead to low conductivities[98,195]. In general, they can be divided into post-deposition approaches such as (photo)lithography[159] and direct patterning strategies including screen printing[161], inkjet-printing[52,162] and electrochemical deposition[163,164]. A simplified approach for photo-patterning PEDOT:PSS without the need for etching and the removal of residual photoresist, introduces photopolymerizable additives into PEDOT:PSS. Photomasks and irradiation followed by washing yield micron-sized PEDOT:PSS patterns[98,165,166]. An opposite strategy fine-tunes the interface chemistry of the substrate, so that PEDOT:PSS only adheres in specified areas[167]. Another approach attaches a mask to rubbery substrates prior to the spin-coating of PEDOT:PSS[9,70]. Lastly, PEDOT:PSS may be patterned employing a multi-step etching process[160] as reported by Kostanovskii et al. who deposited copper patterns onto a PEDOT:PSS thin-film, requiring post-patterning acid treatments to remove the residual copper. All the strategies presented above require specific chemicals, lengthy protocol or expensive equipment, underscoring the need for straightforward and easy methods to reliably pattern PEDOT:PSS thin films.

Here, we report an easy and reliable route to transfer (patterned) PEDOT:PSS to flexible and stretchable substrates. The presented transfer-printing employs biodegradable[109] poly(vinylalcohol) (PVA) in combination with the plasticizer glycerol as a flexible and stretchable substrate. To transfer the PEDOT:PSS thin-films, a novel printing method is presented. This method is compatible with common ways of increasing the conductivity and makes use of the creation of hydrogen bonds between PVA, glycerol and PEDOT:PSS. Upon transfer the conductivity is maintained and within the range of literature values. The samples were furthermore examined in detail using PeakForce Quantative Nanomechanical mapping (PF-QNM). Additionally, we demonstrate an extremely easy route towards patterned and transfer-printable PEDOT:PSS structures via O_2-plasma treatment. The work presented here will highly facilitate the processing of next-generation flexible and stretchable electronics.

3.3 Results and Discussion

Transfer-Printing

For the newly established transfer-printing process (illustrated in **Figure 3.1a**), the flexible and stretchable target substrates and the conducting thin-films (PEDOT:PSS) are prepared separately. The substrates consist of the polymer PVA and glycerol as plasticizing additive (see **Figure 3.1d** for chemical structures). PVA is an attractive candidate for substrates in stretchable electronics as it provides several advantages: First of all, hydrogels in general are attractive candidates for healthcare applications in close contact with the human body, due to their high water content, mechanical softness, biocompatibility and biofunctionality[196]. Additionally, PVA is approved by the American Food and Drug administration (FDA) for various medical applications[196]. By incorporating glycerol in varying amounts, the mechanical and optical properties of the substrates can be adjusted by tuning the free volume within the polymer[109,197,198]. This versatility allows access to systems with specifically tailored shapes and mechanical properties for various kinds of applications. To prepare the target substrates, PVA, glycerol (25 wt%) and deionized (DI) water were combined in the appropriate amounts and stirred for three hours at 90 °C to ensure the dissolving of the PVA. The resulting mixtures were drop-cast onto pre-cleaned glass slides and peeled-off after drying. Due to the good film-forming properties of PVA[197–199], the PVA:glycerol mixture can be applied to any type of glass slide and additionally cut into the desired shape after drying. The resulting films are displayed in **Figure 3.1c** and a video demonstrating the transfer-printing process can be found in the Supporting Information (due to the format of this thesis, Supporting Video S1 is accessible online). The films are transparent and may easily be stretched, twisted and bent. PEDOT:PSS thin-films were prepared via spin-coating. To ensure that the printing is compatible with common approaches to increase the conductivity, the transfer-printing of variously treated as well as pristine PEDOT:PSS (PH1000 and AI4083) films was tested to ensure the compatibility with a variety of applications. The examined treatments include the combined incorporation of ethylene glycol (EG) and dodecylbenzene sulfonic acid (DBSA)[51] (pre-deposition) and acid treatments using methansulfonic acid[2] and sulfuric acid[2] as well as DMSO soaking[82] (post-deposition). After the preparation of the PEDOT:PSS films, the PVA/ glycerol substrates were applied onto the PEDOT:PSS thin films. Mild heat facilitates the removal from the donating substrate. Key to this transfer-printing approach are hydrogen bonds formed between the PVA:glycerol target substrates and the polymer PEDOT:PSS[92,93] as schematically indicated in **Figure 3.1a** and **d**. Hence, the adhesion for any tested PEDOT:PSS-treatment has to be lower to the donor glass substrate than to the target PVA:glycerol substrate, enabling a smooth transfer. A previously reported excess of hydrophilic PSS that is forming at the top of spin-coated PEDOT:PSS thin films[79,200] might also be beneficial for the transfer-printing process as suggested in[201] and schematically indicated in **Figure 3.1d**. In general, transferring large areas of film is challenging as cracks can form easily[94,202]. Using the here reported methodology, however, it is possible to transfer films with an area of at least 7.5 x 2.5 cm. Furthermore, this approach is applicable to a wide range of PEDOT:PSS film thicknesses: **Figure 3.1e** shows the respective donating substrates as well as transferred films from drop-casted to spin-coated PEDOT:PSS films (drop-casted: 2.8 µm; spun at 500 rpm: 120 nm and at 1000 rpm: 70 nm).

In summary, the transfer-printing method presented here is not dependent on acids[2,94] or surfactant and/or doping treatments[2,92–94], is applicable to various film thicknesses and, unlike previously reported methods[92], pristine thermally annealed PEDOT:PSS film may be transferred as well. Please see **Tab. S3.1** for a comparative overview of various transfer-printing techniques onto flexible and stretchable target substrates, pointing out the advantages this methodology offers. Lastly, the PVA substrates are water-soluble and allow for environmentally friendly disposal by employing mild heat and stirring (**Figure 3.1f**).

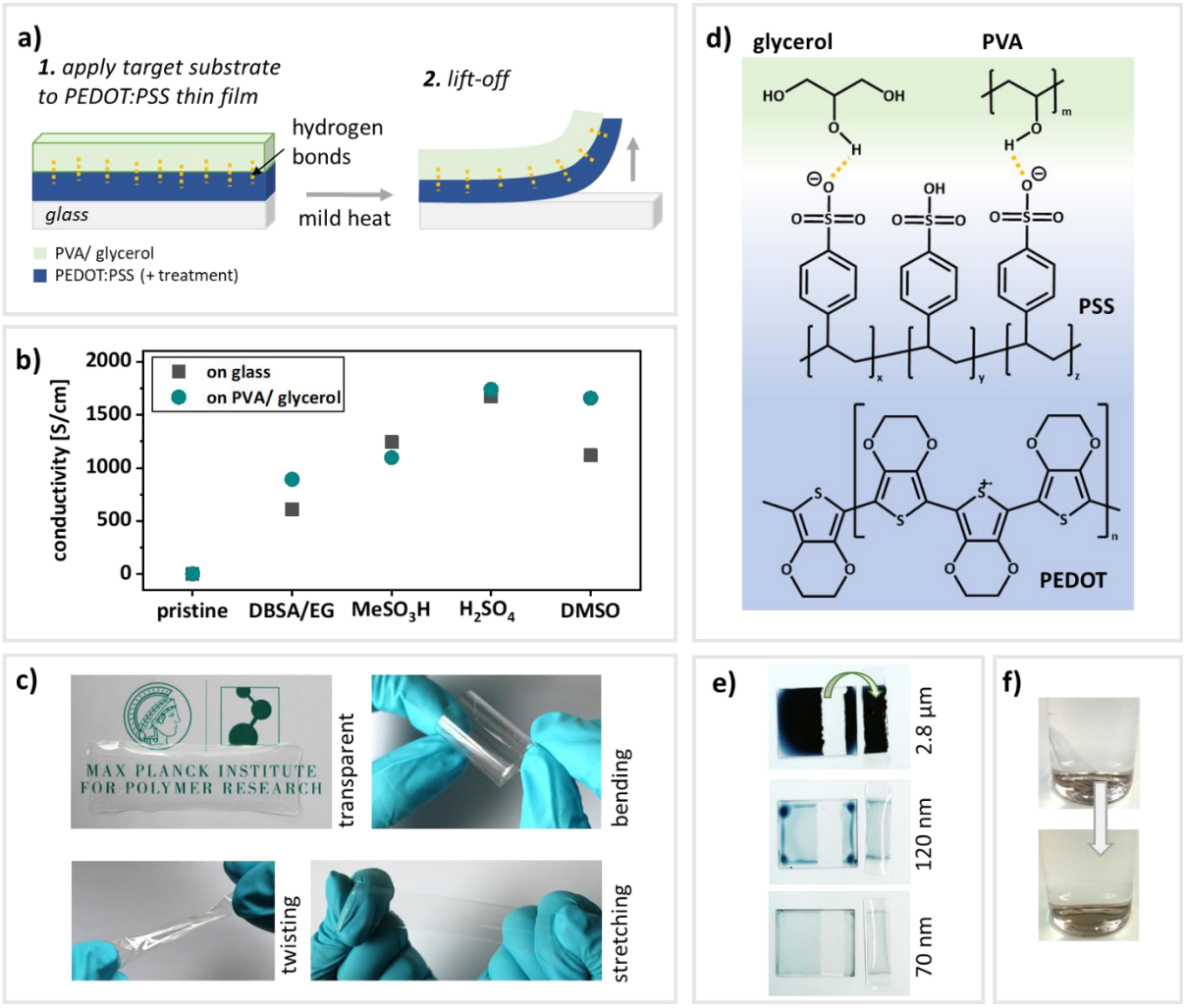

***Figure 3.1**: **a)** Schematic illustration of the transfer-printing process. **b)** Comparison of electrical conductivities of variously treated PEDOT:PSS thin-films on glass and PVA:glycerol substrates. **c)** PVA:glycerol (25 wt%) substrates are transparent, bendable, twistable and stretchable. **d)** Schematic drawing of the formation of hydrogen bonds between glycerol, PVA and PEDOT:PSS, which enables the transfer-printing process. **e)** Transfer-printing PEDOT:PSS with different thicknesses. **f)** Dissolving the PVA:glycerol/PEDOT:PSS samples in water for environmental-friendly disposal.*

Properties of Transfer-Printed Films

To make full use of the transfer-printed PEDOT:PSS films in electronic applications, they need to maintain their electrical properties during the transfer process. Hence, the conductivity of variously treated PEDOT:PSS thin-films was measured prior to and after the transfer via two point probe measurements. **Table 3.1** compares the conductivities of reported literature values, the reproduced process on glass slides and the transfer-printed films on PVA:glycerol (25 wt%) substrates. A graphical comparison is given in **Figure 3.1b**. Please note that for the assurance of process functionality, for each treatment an identical thin film was assessed both before and after transfer-printing. Furthermore, to demonstrate reproducibility, the same procedure was conducted on six individual samples of PEDOT:PSS treated with DBSA and EG (**Fig. S3.1**). It is furthermore noteworthy that for PEDOT:PSS AI4083 recording a resistance value was not possible due to too low currents (on glass as well as PVA:glycerol). Therefore, we have recorded and attached a video demonstrating the transfer-printing (video S1). As expected, the pristine PEDOT:PSS shows a conductivity of only a few S/cm, while the pre- and post-deposition treatments lead to a significant increase in conductivity. We would like to point out that the aim of this work is not the full optimization towards the highest possible

conductivities, but rather to verify that the electronic properties are maintained during the transfer. The conductivities in our work are either identical or slightly lower than the values reported in literature. However, most importantly, the initial conductivity of PEDOT:PSS on glass is maintained during the transfer process and very similar on glass and on PVA:glycerol (25 wt%) substrates for all treatments, demonstrating the versatility of the process. Interestingly, the transferred films on the stretchable PVA:glycerol substrates oftentimes even yield higher conductivities than initially on glass substrates. This may be caused by doping effects from the glycerol[40,49]. We conclude that the electrical properties of the thin films are not impaired by the transfer-printing process or might in fact even be enhanced.

Since transparency may also be a prerequisite for certain applications[67] such as optoelectronic devices it should be maintained during the transfer process. Within the visible spectrum, the transmittance of all PEDOT:PSS thin-films after transfer-printing onto PVA:glycerol remains well above 95% compared to the value obtained for PEDOT:PSS thin-films on glass (**Fig. S3.3** and **Tab. S3.3**). Hence, our methodology enables the fabrication of highly conductive, reaching almost 3000 S/cm (**Table 3.1**), and transparent PEDOT:PSS thin-films on flexible and stretchable substrates.

Table 3.1: *Comparison of conductivity, surface roughness and adhesion properties of films on glass carriers and after transfer on PVA:glycerol (25 wt%) substrates and to literature values.*

	conductivity [S/cm]			**surface roughness [nm]**		**adhesion force [nN]***	
	literature on glass	on glass	on PVA: glycerol (25 wt%)	on glass	on PVA: glycerol (25 wt%)	on glass	on PVA: glycerol (25 wt%)
PEDOT:PSS	2.5[82]	0.5	0.8	1.4	1.0	5.2	0.92
+ DMSO	2124[82]	1600	1655	1.6	1.4	0.9	0.29
+ H_2SO_4	2830[2]	2808	2976	3.0	1.2	2.2	0.28
+ DBSA/EG	800[51]	797	927	1.3	1.7	1.9	0.25
+ $MeSO_3H$	3090[2]	1348	1860	2.7	1.3	2.3	1.0

**between the sample and the SFM-tip extracted from PeakForce SFM measurements*

When envisioning future applications and for a full characterization of the transfer-printed films, insight into the surface morphology is crucial. Therefore, we performed a detailed study of the morphological and mechanical properties of the thin films before and after transfer-printing, performing scanning force microscopy (SFM) measurements applying peak-force mode. In this mode, we simultaneously map the adhesion between the SFM-tip and the surface and deformation of the film corresponding to its mechanical properties[203]. These properties provide further insight into a material beyond pure topological information. To the best of our knowledge there are only few reports on pre- and post-treated PEDOT:PSS thin-films on flexible substrates[63,80,81,94]. Additionally, these images were acquired in tapping mode and a detailed SFM adhesion study of variously treated PEDOT:PSS thin films is still lacking. All PEDOT:PSS thin films on glass exhibit a surface roughness in the order of a few nanometers (**Fig. 3.2**). The roughness values extracted from several images of an area of 1 µm x 1 µm indicate smooth surfaces (**Tab. 3.1**). In the corresponding adhesion force maps (greenish color scale, **Fig. 3.2**) we observe a contrast, which we attribute to a core-shell structure of PEDOT:PSS. A core-shell morphology is commonly reported in literature[80,81,84,94,204–208]. Taking the morphology into account, we assign the dark green areas (lower adhesion forces) to the PEDOT-rich cores and bright areas (higher adhesion forces) to the PSS-rich shells. In SFM images recorded in tapping mode it is generally assumed that bright areas (positive phase shift of the oscillating cantilever)

correspond to PEDOT-rich and dark areas to PSS-rich regions[80,206,209]. A comparison of the adhesion maps of treated and untreated PEDOT:PSS thin films reveals a reduction of the grain size caused by post-deposition acid treatments with diluted $MeSO_3H$ (40%) or H_2SO_4 (18%), which is consistent with literature[94,204,207,210]. In our recordings, this reduction in grain size is also observed for DMSO post-deposition treatments, whereas the grains appear to be more elongated and oval-shaped upon the addition of DBSA/EG. We calculated the mean adhesion force values for all surfaces (see **Table 3.1**). The average adhesion decreases with increasing conductivity. This may be attributed to the content of PSS in the PEDOT:PSS films upon conductivity-enhancing treatments as reported previously[84,206].

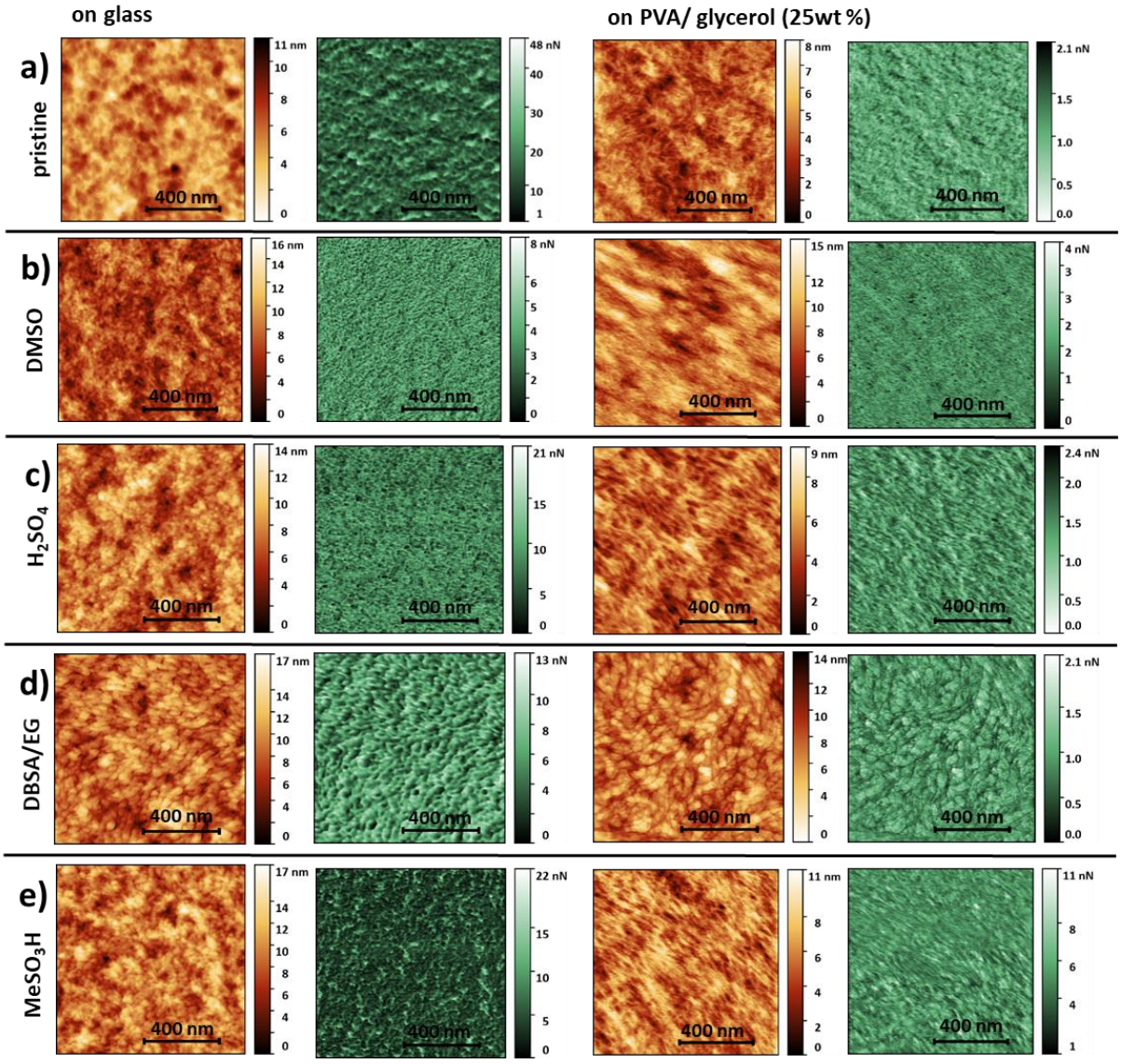

***Figure 3.2**: SFM images recorded in peak force mode. We selected an orange color scale for topography and green color scale for the corresponding adhesion forces. **a)** pristine (PH1000), **b)** DMSO[82]-, **c)** H_2SO_4[2]-, **d)** DBSA/EG[51]- and **e)** $MeSO_3H$[2]-treated PEDOT:PSS thin films on glass (left) and transfer-printed onto PVA/ Glycerol (25 wt%, right). All scale bars correspond to 400 nm.*

The topography images of the transfer-printed PEDOT:PSS films onto PVA (25 wt% glycerol) reveal a fibril-like structure with a clearly visible network of more elevated thin fibers throughout all treatments. Please note that due to the nature of the printing process the lower PEDOT:PSS surface facing the glass slide ends up facing upwards on the PVA:glycerol substrates. Hence, depending on whether the PEDOT:PSS film is examined on glass or PVA:glycerol different PEDOT:PSS surfaces are examined. A fibril-like morphology was not observed for any PEDOT:PSS films on glass. Therefore, we attribute this morphology to the PVA substrates. Upon transfer-printing the overall surface roughness values are decreased, except for DBSA/EG treated PEDOT:PSS. Nevertheless, we find that the printing leads to a very smooth surface with a rms-roughness <1.5 nm. Additionally, we observe an overall decrease in adhesion forces. The mean adhesion force follows no longer the measured conductivity (**Tab. 3.1**). As mentioned above, the transfer-printing process is enabled by the formation of hydrogen-bonds between the substrate and PEDOT:PSS. The SFM analysis indicate that the interaction with the PVA substrates seems to induce morphological changes within the PEDOT:PSS, independently of the performed treatment. However, we show by the conductivity measurements, that these morphological changes and newly-formed bonds do not negatively affect the electrical properties of the PEDOT:PSS films. It is worth mentioning that a thin layer of excess PSS accumulates on top of the PEDOT:PSS during the film formation on glass[79,200] which, due to the nature of the transfer-printing, ends up facing the PVA/ glycerol substrate. This might additionally be reflected in differences in the SFM recordings comparing films on glass and PVA:glycerol substrates.

Creating Structures: Patterning and Printing PEDOT:PSS

For functional electronic devices and circuits, patterning is crucial to e.g. define electrodes, limit leakage currents, avoid short circuits or decrease parasitic capacitances. Here, structures were defined using an O_2-plasma treatment. For this, a shadow mask was attached to the PEDOT:PSS films on glass and then an O_2-plasma treatment was applied for 4 min at 100 Watt. Parts of the PEDOT:PSS films that are exposed to the plasma are removed, while covered parts remain intact. We tested and verified the applicability of the procedure for all the above introduced PEDOT:PSS treatments. This direct plasma-patterning does not significantly affect the conductivity (see supplementary information for detailed characterization) and proves to be an easy, straightforward approach to directly pattern PEDOT:PSS thin films. Additionally, this approach does not rely on specialized equipment or long and complicated protocols. **Fig. 3.3a** depicts that various kinds of structures can be patterned and later on transferred, ranging from rectangles and stripes to stars. Even circular structures can be transferred easily. Please see **Fig. S3.4** - **S3.7** for a detailed description of all margins and a SFM topography image showing the boundary between patterned and transfer-printed PEDOT:PSS and PVA:glycerol (25 wt%). **Fig. 3.3b** depicts patterned and transfer-printed stripes with dimensions ranging from 200 - 50 µm. Furthermore, electrodes can be easily deposited on top pf the PEDOT:PSS structures by thermal evaporation in vacuum without damaging the films and without compromising the electrical performance. Finally, with the established transfer-printing process and electrode deposition (**Fig. 3.3c**), all the necessary building blocks are in place to realize future stretchable and flexible electronic devices such as stretchable OECTs for biosensor applications.

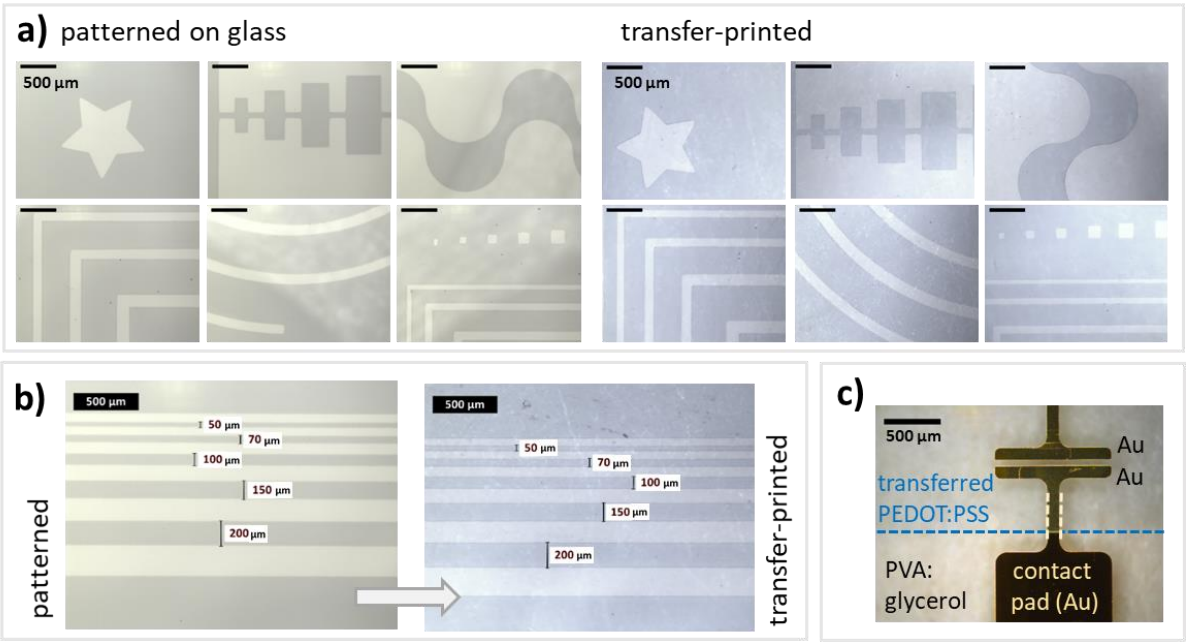

Figure 3.3: a) *Selection of microscope images of the O_2-patterned PEDOT:PSS thin films on glass (left) and transfer-printed on to PVA:glycerol (25 wt%) substrates (right).* ***b)*** *Patterned and transfer-printed stripes (minimal width: 50 µm).* ***c)*** *Patterned PEDOT:PSS on PVA:glycerol substrates with top gold contacts (thermally evaporated in vacuum) for device applications. The length of each scale bar is 500 µm.*

3.4 Conclusions

In conclusion, a novel transfer-printing method for (plasma-patterned) PEDOT:PSS thin films was established which will highly benefit the processing of future flexible and stretchable electronics. Using this method, various (harsh) conductivity-enhancing treatments may be performed prior to transfer and hence without damaging the target substrate. Furthermore, the method relies on neither pre- nor post-treatments and allows the transfer of various film thicknesses and of large areas of film as well as various patterned structures. The electrical properties of the films are not impacted by this process. Lastly, the PVA substrates are water-soluble and allow for environmentally friendly disposal.

3.5 Supplementary Information

Experimental

Materials: All materials (iso-propanol (IPA), acetone, DMSO, $MeSO_3H$, H_2SO_4, EG, BSA, PVA, glycerol) were acquired from Sigma Aldrich, TCI, honeywell riedel-de haën and PanReac AppliChem and used as received, without any further purification. PEDOT:PSS (Clevios PH1000 and AI4083, Hereaus Deutschland GmbH) was stored at 3.7 °C. Right before usage it was placed in an ultrasonic bath for 20 min and filtered through a 45 µm syringe filter.

Transfer-printing of PEDOT:PSS thin films: All samples were prepared and measured in a clean room (temperature: 22 °C; humidity: 40 – 44 %). First, glass carriers (7.5 cm x 2.5 cm) were cleaned in an ultrasonic bath in DI water for 5 min, acetone for 10 min and lastly IPA for 10 min. Afterwards, they were dried in an oven at 140 °C for 10 min. PVA:glycerol mixtures were prepared in DI water and stirred at 90 °C for three hours. 1 g PVA (M_w= 31000 – 50000 g/mol, 99 % hydrolyzed) was combined with 25 wt% glycerol in 9 mL DI water. Prior to usage the mixture was filtered through a 45 µm syringe filter and placed in an ultra sonic bath for 10 min. The mixture (1.5 mL) was drop-casted onto the previously cleaned glass slides and allowed to dry overnight yielding 95-100 µm thick films. To increase the wettability, the glass slides were previously exposed to a UV-ozone treatment for 20 min. PEDOT:PSS thin films were spin-coated on glass carriers at 500 - 1000 rpm for 60 s. Each treatment to increase the conductivity was performed following the respective procedure.[2,51,82] The pristine PEDOT:PSS thin films were thermally annealed at 120 °C for 10 min after spin-coating. After peeling-off the PVA:glycerol substrates, they were carefully applied onto the PEDOT:PSS thin films and placed on a hot plate at 80 °C for 2 min (PVA:glycerol-side facing up). Transparencies were measured using an UV-vis spectrometer (Agilent Cary 60 UV-vis).

Patterning of PEDOT:PSS thin films: A metal shadow mask was attached closely to the PEDOT:PSS thin film on glass, fixated using Kapton tape and then exposed to an O_2-plasma for 4 min at 100 Watt and a process pressure of 50 Pa (Nordson AP-600 Plasma System). By ensuring that the mask is attached closely, only minor shadowing effects are observed. The patterned structures were then transfer-printed following the above described procedure. Gold contacts (300 nm) were evaporated in vacuum using a shadow mask.

Electrical characterization: The conductivity was determined through I-V measurements using a two point probe set-up and a Keithley 2000 Multimeter. The film thickness was determined using a surface profilometer (Bruker, DektakXT Stylus Profiler). Depending on the treatment performed, film thicknesses ranged between 28 and 63 nm (see **Tab. S3.2**, Supporting Information).

Imaging: PeakForce-Quantitative Nanomechanical Mapping (PF-QNM) SFM measurements were performed using a Bruker Dimension ICON platform using OLTESPA NanoAndMore cantilevers (frequency: 70 KHz, spring constant: 2 N/m, back/ tip side coating: Al). From topography images, we calculated the root-mean-square roughness (rms also referred to as Image R_q) using the Nanoscope analysis software (Version 1.9). All rms- roughness values correspond to an area of 1 μm^2. The mean adhesion force was determined for the same area. For all SFM-samples, PEDOT:PSS films were formed by spin-coated at 750 rpm for 60 s and the glyercol amount in the flexible substrates was 25 wt%. The samples were mounted to the SFM-wafer chuck using a double-sided tape. Optical microscope images were taken in bright field mode and edited using a confocal microscope (Leica DM6000 M) and the according software (Leica Application Suite Version 4.12.0).

Literature Overview

***Table S3.1**: Comparative overview of different transfer methods onto flexible and stretchable substrates, including details on the donating substrate, required treatment, receiving substrate, limitations on PEDOT:PSS formulation and, if applicable, the dimensions of structured PEDOT:PSS that can be transferred.*

reference	donating substrate	required treatment		receiving substrate	PEDOT:PSS formulation limited?	structures transferred?	conductivity maintained after transfer?
		decrease adhesion from donating substrate	increase adhesion to receiving substrate				
[2]	glass	acid soaking or dipping treatments		PDMS	yes	no	almost identical
[93]	glass	acid treatment	PEDOT:PSS/ d-sorbitol layer on top of PET	PET	yes	no	not explicitly given
[70]	glass		chemically tailored PDMS	APTES-PDMS	unknown	yes; no exact margins given, approx. mm-scale	increased
[94]	glass	acid treatment		PDMS	yes	yes; margins not given	almost identical
[92]	glass	surfactant DBSA		poly (lactic) acid	yes	yes; 500 µm	decrease
this work	**glass**	**none**	**none**	**PVA: glycerol**	**no**	**yes ≥ 50 µm**	**almost identical/ increase**

Electrical Characterization

***Table S3.2**: Film thickness, resistance and conductivity values for variously treated PEDOT:PSS thin films before and after transfer-printing and O_2-plasma etching, respectively. All films were spin-coated speed at 1000 rpm for 60 s.*

		PRINTING				O_2-PLASMA			
		before on glass		after on PVA: glycerol (25 wt%)		before on glass		after on glass	
	d [nm]	*R* [Ohm]	σ [S/cm]	*R* [Ohm]	σ [S/cm]	*R* [Ohm]	σ [S/cm]	*R* [Ohm]	σ [S/cm]
PRISTINE	74	338 k	0.5	205k	0.8	459 k	0.3	757 k	0.2
DMSO	55	130	1600	125	1655	138	1500	169	1225
H_2SO_4	28	147	2808	139	2976	2.6	1496	284	1453
DBSA/ EG	60	239	797	206	927	257	742	556	342
$MESO_3H$	63	136	1348	98	1860	78	1939	99	1527

Please note that all resistance values were recorded for the exact same thin film before and after printing or O_2-plasma etching, respectively.

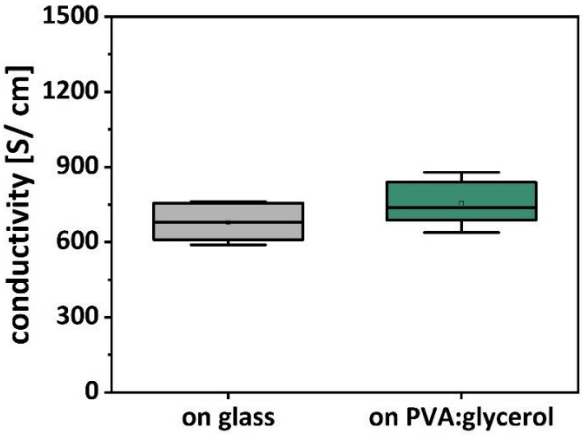

***Figure S3.1**: Conductivity values for multiple DBSA/EG treated PEDOT:PSS thin films before (on glass) and after transfer-printing (on PVA:glycerol).*

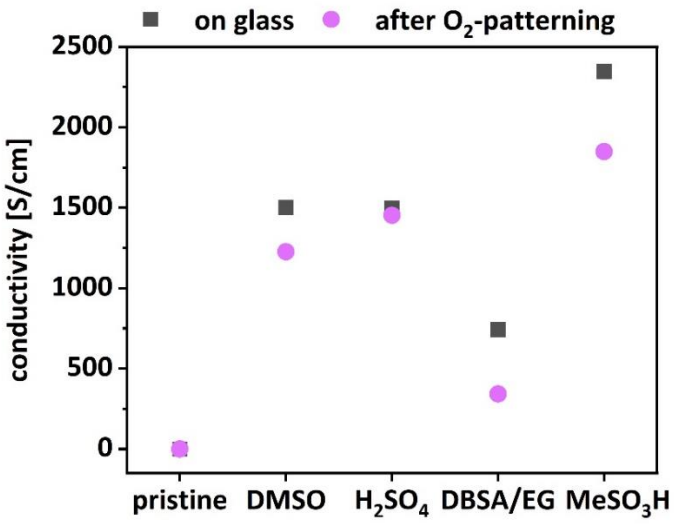

***Figure S3.2**: Effect of O_2-patterning on the conductivity of PEDOT:PSS films.*

Transmission Measurements

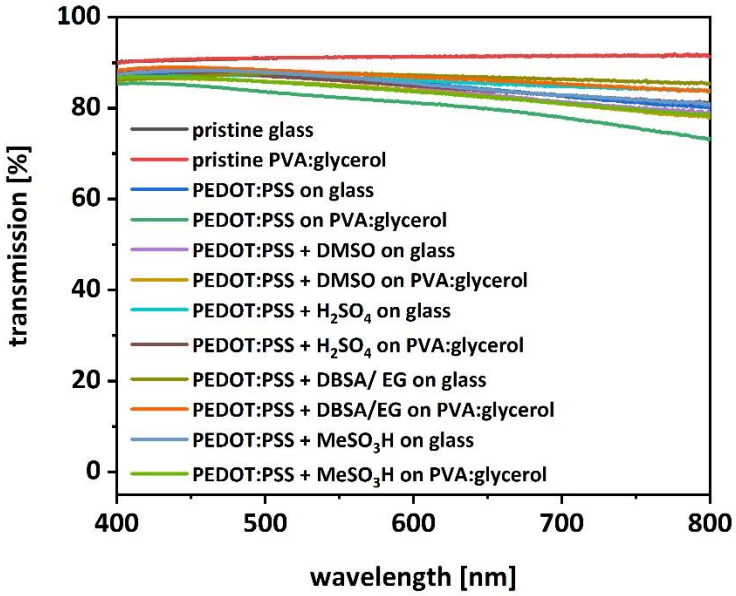

***Figure S3.3**: Transmission spectra of pristine glass and PVA/glycerol (25 wt%) substrates, as well as variously treated PEDOT:PSS films on glass or transfer-printed on PVA substrates, respectively.*

***Table S3.3**: Transmission at λ = 550 nm of pristine glass and PVA:glycerol (25 wt%) substrates, as well as variously treated PEDOT:PSS on top of glass or transfer-printed, respectively.*

	TRANSMISSION [%]				
PRISTINE GLASS	91.3				
PRISTINE PVA:GLYCEROL (25 WT%)	91.3				
PEDOT:PSS	pristine	DMSO	H_2SO_4	DBSA/ EG	$MeSO_3H$
ON GLASS	85.1	86.4	86.8	87.6	86.9
ON PVA:GLYCEROL (25 WT%)	86.3	85	86	87.6	84.7

Mask Layout and Detailed Margins of Patterned and Transfer-Printed PEDOT:PSS Thin-Films

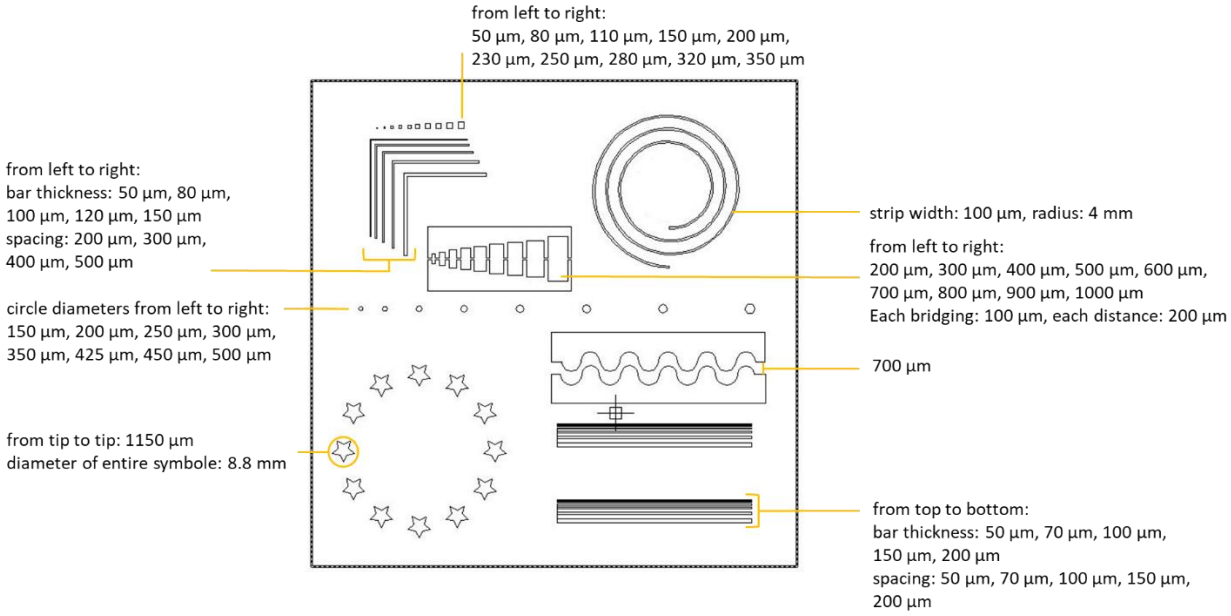

***Figure S3.4**: Mask layout for patterning PEDOT:PSS, including all margins.*

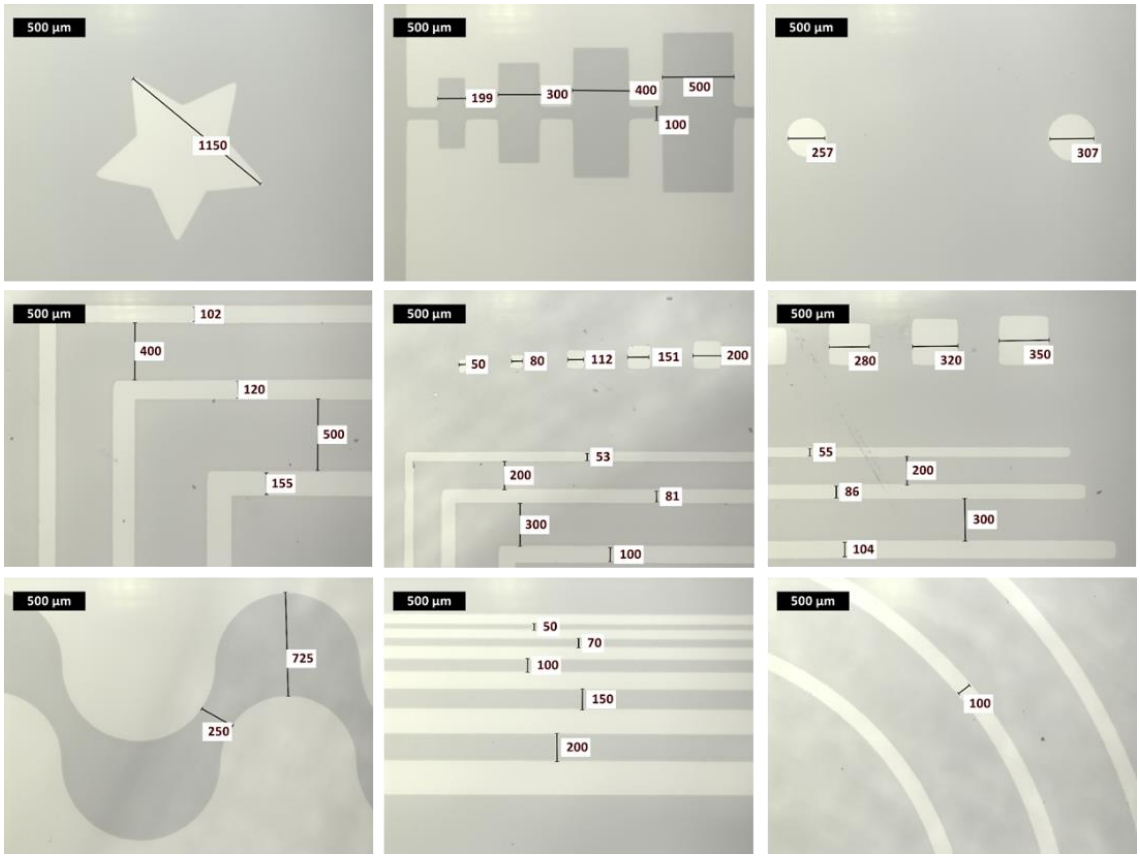

***Figure S3.5**: Detailed margins of O_2-patterned PEDOT:PSS.*

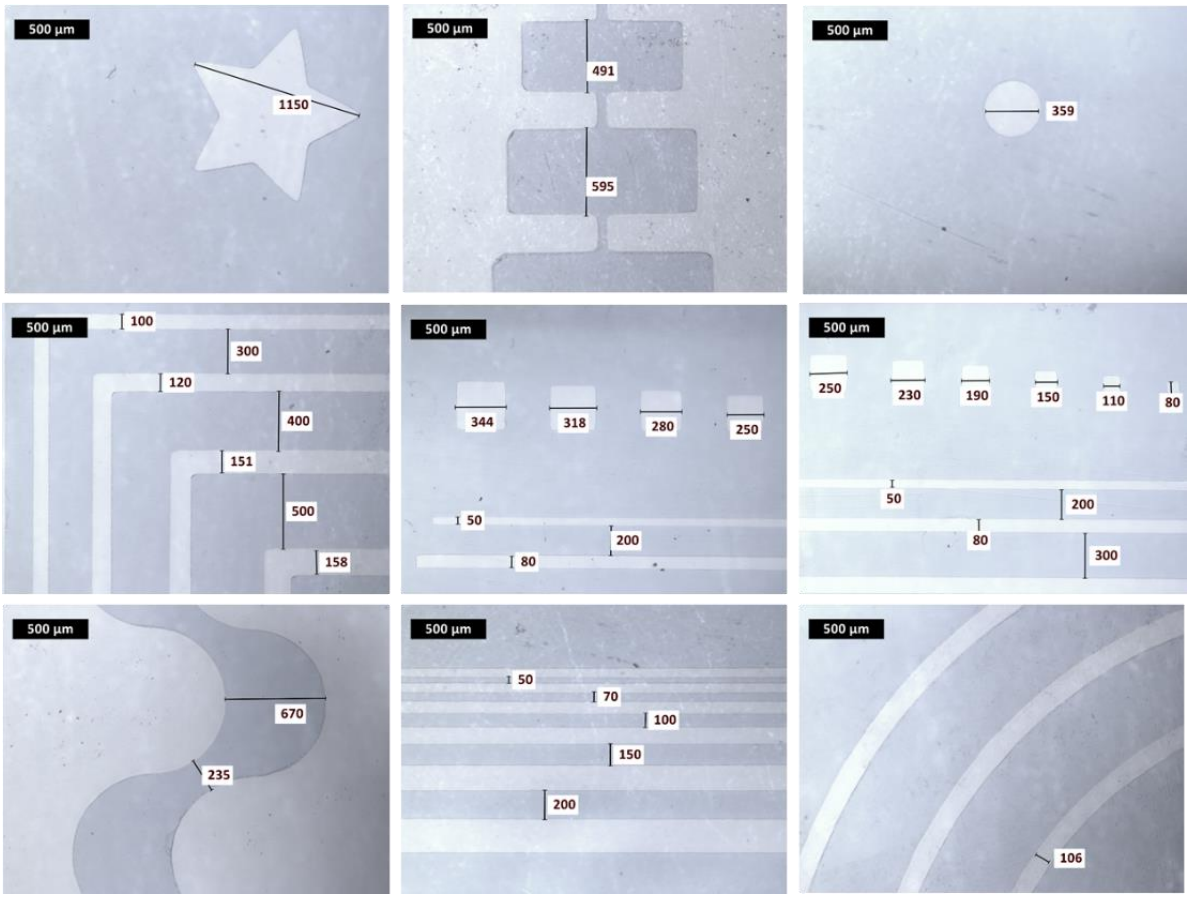

***Figure S3.6**: Detailed margins of O_2-patterned and subsequently transfer-printed PEDOT:PSS on PVA:glycerol (25 wt%) substrates.*

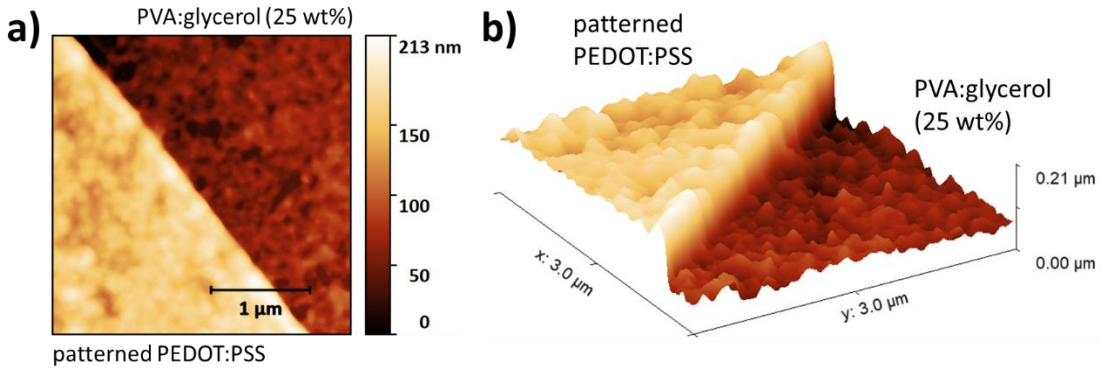

***Figure S3.7**: Scanning Force Microscopy recordings (3 µm x 3 µm) of patterned and transfer-printed PEDOT:PSS o PVA:glycerol (25 wt%). a) Topography image and b) 3D representation.*

4. Enhanced Electrical Performance and Stretchability by Plasticizer-Facilitated PEDOT:PSS Self-Alignment

Chapter details

Authors:

Carla Volkert, Mateusz Brzezinski, Pablo Gomez Argudo, Renan Colucci, Sapun H. Parekh, Pol Besenius, Jasper J. Michels, Ulrike Kraft

Reproduced with minor changes from:

C. Volkert, M. Brzezinski, P. G. Argudo, R. Colucci, S. H. Parekh, P. Besenius, J. J. Michels, U. Kraft, 'Enhanced Electrical Performance and Stretchability by Plasticizer-Facilitated PEDOT:PSS Self-Alignment'; *Adv. Sci.* **2025**, 2502853; https://doi.org/10.1002/advs.202502853

Author contributions:

C. Volkert: Conception, planning and execution the experiments. Interpretation of the results and writing of the manuscript.

R. Colucci: Support in performing electrical measurements. M. Brzezinski and P. G. Argudo: Measuring Raman spectroscopy and analyzing the respective results. J. J. Michels: Conceptualizing of the model and performing of the calculations. P. Besenius and S. H. Parekh: Discussion on the concept and the results. U. Kraft: Supervision of the project. Discussion on the concept and the results and editing of the manuscript.

4.1 Abstract

Stretchable, soft electronics have high potential for wearable healthcare applications and biointerfacing. One approach to render inherently brittle conductive polymers such as poly(3,4-ethylenedioxythiophene):poly(styrenesulfonate) (PEDOT:PSS) stretchable are organic plasticizers. However, little is known on how they affect the morphology and in result the electrical properties of conductive thin-films. This study fundamentally explores this relationship using a bilayer model of transfer-printed PEDOT:PSS on stretchable, biocompatible poly(vinyl alcohol) substrates infused with glycerol (15 – 55 wt%). The diffusion of the plasticizer leads to a reorganization of PEDOT and PSS, which is investigated using a multicomponent diffusion model. This approach correctly predicts the (plasticizer-dependent) increase in conductivity that followed plasticizer diffusion and is attributed to the reorganization towards more interconnected PEDOT domains. In result, the system shows an improved electrical response to strain as well as crack-free elongation. Simultaneously, the electrical resistance decreases to one-fifth of its initial value, which is attributed to chain-alignment upon strain.

4.2 Introduction

Significant potential lies in flexible and stretchable electronics with applications ranging from portable electronics over wearable devices on-skin electronics and neuroprosthetics to personalized healthcare. As a result, extensive research efforts are directed towards the development of conformable devices, including biosensors[10], optoelectronic devices[2], organic field effect transistors (OFETs)[3,4], light-emitting diodes (LEDs)[6] and organic electrochemical transistors (OECTs)[7–9,11,97]. As flexible and stretchable electronics advance, particularly in healthcare applications, the quest for materials capable of maintaining their electrical properties under deformation becomes increasingly crucial. Various materials, including poly(3,4-ethylenedioxythiophene):poly(styrenesulfonate) (PEDOT:PSS), have shown promise in creating devices for bioelectronics and personalized healthcare[16,105]. Beyond its biocompatibility, PEDOT:PSS offers high and tunable conductivity, transparency and commercial availability[37,49]. However, the inherent brittleness[7,42] and limited elongation capabilities of pristine PEDOT:PSS (2 %[62]) pose challenges for meeting the requirement of tolerating up to 30 % strain for applications in healthcare electronics[9]. To transform PEDOT:PSS from a brittle into a stretchable organic semiconductor, various PEDOT:PSS-plasticizing approaches have been explored. These include the incorporation of plasticizing chemicals such as ionic liquids[41,63–67], Triton-X 100[42,69–71] and/ or low molecular weight organic compounds[40,42,68]. Additionally, blends of PEDOT:PSS with non-conductive polymers as well as the addition of one or more additives to these blends have been investigated in previous reports[41,42,57,75,76]. Efforts to stretch pristine PEDOT:PSS have been reported as well[80,81,89]. The presented strategies enable PEDOT:PSS to maintain its conductivity to varying degrees during elongation and pave the way towards stretchable electronics. However, the underlying mechanism for PEDOT:PSS plasticization remains poorly understood. In addition to modifying the PEDOT:PSS formulation to enhance stretchability, diverse supporting substrates have been explored. These include polyimide (PI)[80,81], poly(dimethylsiloxane) (PDMS)[64,65,80,88] and styrene ethylene butylstyrene (SEBS)[40,52,63,66,89]. In the pursuit of stretchable healthcare electronics, we recently reported the usage of poly(vinyl alcohol) (PVA) as an attractive polymer for supporting substrates[211] (**Chapter 3**). It offers biocompatibility, mechanical softness and high water content, making it suitable for medical applications[196].

The striking need for novel approaches towards deformable conducting materials and supporting substrates is underlined by crucial material limitations such as insufficient stretchability and toxicity, which makes current systems unsuitable for medical applications. Furthermore, ensuring stable electronic properties is essential for bridging current technological gaps in deformable electronics. In addition,

although plasticizers have been shown to allow PEDOT:PSS to better adapt to strain, little is known about the underlying mechanisms. In this work, using our previously presented transfer-printing method[211] (**Chapter 3**), we fabricate a biocompatible bilayer system with pristine transfer-printed PEDOT:PSS films on PVA:glycerol substrates. Within this system, glycerol is found to be capable of permeating into the conductive layer, triggering morphological rearrangement and subsequently inducing stretchability. Through a comprehensive analysis including multicomponent diffusion modelling on the plasticizer-induced PEDOT:PSS rearrangement, electrical characterization, microscopic imaging, Raman spectroscopy and scanning force microscopy (SFM), we find that the diffusion-active glycerol in the PVA substrate facilitates crack-free elongation of PEDOT:PSS films (up to 160 %). Furthermore, through chain-alignment in PEDOT:PSS, its ability to maintain its electronic properties upon strain is significantly increased.

4.3 Results and Discussion

As described above, the underlying mechanism and plasticizer-triggered rearrangements of PEDOT and PSS remain poorly understood. This is partly because these rearrangements usually take place in the liquid state during processing, but also because plasticized systems are inherently more mobile and therefore more difficult to study. Hence, we employed a model system consisting of PEDOT:PSS films on PVA substrates loaded with 15 – 55 wt% glycerol to study the effect of an organic plasticizer on PEDOT:PSS in detail. We select this range as it balances capturing loading-dependent effects on PEDOT:PSS while avoiding potential system interference from excessively high plasticizer concentrations.

The PEDOT:PSS films were uniformly spin-coated on glass slides and subsequently transfer-printed onto the PVA:glycerol substrates using our previously reported methodology[211] (**Chapter 3**). Since the glycerol is not covalently bound by either the PVA or the PEDOT:PSS, we hypothesized that after transfer-printing of PEDOT:PSS films onto PVA:glycerol substrates, glycerol would partially diffuse from the substrate into the conducting thin film and partition across these two layers. This diffusion should be driven by a gradient in the glycerol's chemical potential between the substrate and the PEDOT:PSS thin film (schematically depicted in **Fig. 4.1a**). Due to the ingress of glycerol in the PEDOT:PSS film, we expected an increase in the conductivity[40,212,213] (or decrease in resistance, respectively). Assuming that glycerol acts as a plasticizer we also anticipated an increased PEDOT:PSS polymer-chain mobility, which would allow enhanced mechanical adaptation during stretching. We tested these hypotheses on increasingly glycerol-loaded PVA substrates with data recorded for substrates containing 15 wt% glycerol displayed in green, 25 wt% in red, 35 wt% in blue, 45 wt% in yellow and 55 wt% in purple throughout this study. Since the vapor pressure of glycerol is very low at room temperature[214], we can safely neglect any evaporation-related changes in the glycerol content of the substrates.

First, the sheet resistance of the static PEDOT:PSS films is recorded as a function of time over a period of 24 h after transfer-printing (**Fig. 4.1c** upper panel) to equilibrate the system and to study the response of the PEDOT:PSS films to the partitioning of the glycerol. The Methods and Materials section and the Supplementary Information (SI: *Diffusion of Glycerol*) contain a detailed description of the sample preparation, as well as the absolute resistance plotted against the time for each set of films (**Fig. S4.1**). Except for the 15 wt% glycerol films, the sheet resistance indeed slowly decreases over time, levelling off at lower values (higher conductivity) with higher glycerol percentages. This observation confirms the hypothesis that non-conductive molecular plasticizers can diffuse from an underlying substrate into the conductive polymer layer thereby affecting its conductivity. Fitting the sheet resistance vs time data to an empirical exponential function (see SI, **Fig. S4.2**) yields an apparent diffusivity of the order 10^{-18} - 10^{-19} m^2/s. Since this very low value is not consistent with the diffusion of a molecule as small as glycerol (see SI: *Experimental Curve Fitting*), the rate in the decrease in sheet

resistance is much more likely determined by a redistribution of the bulky polymer chains within the PEDOT:PSS film, which occurs on significantly longer timescales, however facilitated by fast initial ingress of glycerol. Furthermore, the dependence of the plateau value on the glycerol loading (**Fig. 4.1c**) suggests that the final sheet resistance represents a thermodynamic equilibrium.

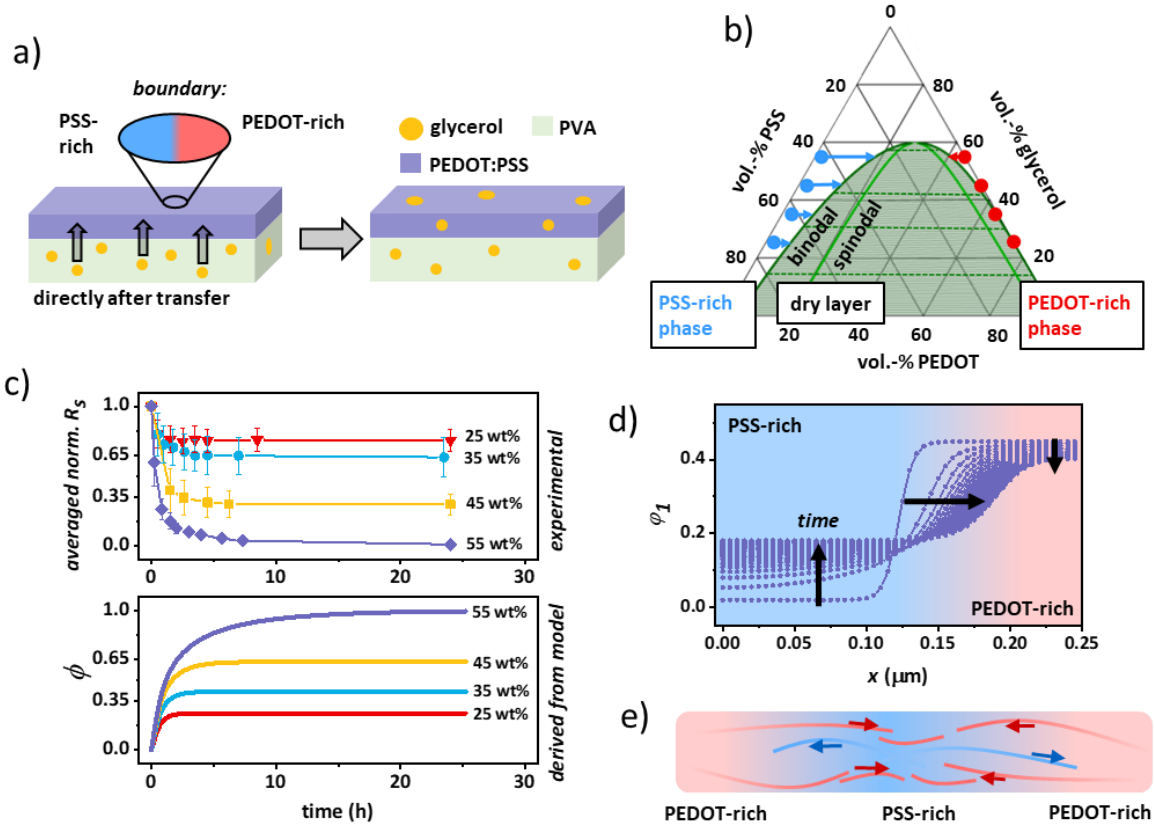

Figure 4.1: *Diffusion-active substrates:* ***a)*** *Schematic depicting glycerol diffusion from the substrate into the conducting PEDOT:PSS thin film. Magnified: Simplified boundary between PEDOT- and PSS-rich areas in core-shell structure.* ***b)*** *Calculated ternary phase diagram for the mixture PEDOT:PSS:glycerol. The grey lines are tie-lines that connect compositions of coexisting phases. The blue and red dots indicate the initial out-of-equilibrium compositions after glycerol ingress. The arrows show the change in composition during polymer redistribution. The dashed green lines are tie-lines connecting the compositions of coexisting phases.* ***c)*** *Top: Experimentally obtained decrease of the averaged normalized sheet resistances over time of transfer-printed PEDOT:PSS on glycerol-loaded PVA substrates. Bottom: Normalized fraction of PEDOT in the PSS rich phase (Φ).* ***d)*** *Concentration profiles of normalized PEDOT concentration versus spatial coordinate in a 250 nm 1-dimensional domain at different points in time for substrates containing 55 wt% glycerol.* ***e)*** *Schematic drawing of the intermixing of PEDOT and PSS triggered by glycerol: More PEDOT migrates into the PSS-rich phase than vice versa, which leads to better connected PEDOT grains.*

To better understand the reorganization of PEDOT and PSS triggered by the plasticizer glycerol, as well as and its dependence on the glycerol loading, a generalized 1D multicomponent diffusion model based on mixing thermodynamics was employed, while making the following assumptions: i) the PEDOT:PSS morphology consists of nanoscopic well-conducting PEDOT-rich and poorly conducting PSS-rich domains[79–81], of which the latter are the limiting factor for the overall conductivity of the blend, ii) PEDOT and PSS are mutually immiscible but glycerol acts as a compatibilizer that enhances intermixing and iii) the average concentration of glycerol in the PEDOT:PSS film increases with the loading of the PVA-substrate, assuming a 1:1 partitioning. This last assumption is based on the fact that

glycerol is highly polar and capable of both accepting and donating hydrogen bonds, which will form with either of the three media, be it PVA, PEDOT or PSS. It is hence reasonable to assume a high and similar glycerol uptake capacity for these substances, which is consistent with glycerol doping levels in PEDOT:PSS reported in the literature[212,213]. Furthermore, due to the fact that the PEDOT:PSS film is about 1000 times thinner than the substrate, the change in glycerol concentration in the latter due to diffusion into the former is negligible. In our calculations we consider the redistribution of PEDOT, PSS and glycerol inside a nanoscopic "unit cell" containing a single interface (schematically depicted in **Fig. 4.1a**). As we will show, with this coarse-grained representation we can explain both the time-dependence and the saturation of the normalized sheet resistance as a function of glycerol content without having to make speculations concerning the details of the PEDOT:PSS morphology. Within our model, the rate of change of the local volume fractions of PEDOT (ϕ_1), PSS (ϕ_2) and glycerol (ϕ_3) is given by:

$$\frac{\partial \phi_1(x)}{\partial t} = \frac{\partial}{\partial x}\Lambda_{11}\frac{\partial}{\partial x}\left(\frac{\delta \mathcal{F}}{\delta \phi_1}\right) + \frac{\partial}{\partial x}\Lambda_{12}\frac{\partial}{\partial x}\left(\frac{\delta \mathcal{F}}{\delta \phi_2}\right) \tag{4.1}$$

$$\frac{\partial \phi_2(x)}{\partial t} = \frac{\partial}{\partial x}\Lambda_{21}\frac{\partial}{\partial x}\left(\frac{\delta \mathcal{F}}{\delta \phi_1}\right) + \frac{\partial}{\partial x}\Lambda_{22}\frac{\partial}{\partial x}\left(\frac{\delta \mathcal{F}}{\delta \phi_2}\right) \tag{4.2}$$

, with $\mathcal{F}$ the free energy, $\frac{\delta \mathcal{F}}{\delta \phi_i}$ the exchange chemical potentials and Λ_{ij} the elements of the Onsager mobility matrix. The definition of the latter is given in the SI: *Onsager Mobility Matrix*. The model is incompressible, which means that we may treat the glycerol fraction ϕ_3 as a dependent variable, given by $\phi_3 = 1 - \phi_1 - \phi_2$. Following earlier work[215–217], we write the free energy of the PEDOT:PSS:glycerol mixture as a summation of local and non-local contributions:

$$\mathcal{F}[\phi_1, \phi_2] = \int \mathrm{d}x [f_{\mathrm{loc}}(\phi_1, \phi_2) + f_{\mathrm{nonloc}}(\partial_x \phi_1, \partial_x \phi_2)] \tag{4.3}$$

, where we define the local contribution based on Flory-Huggins theory[218] :

$$\beta f_{\mathrm{loc}}(\phi_1, \phi_2) = \frac{\phi_1}{N_1}\ln\phi_1 + \frac{\phi_2}{N_2}\ln\phi_2 + \phi_3\ln\phi_3 + \chi_{12}\phi_1\phi_2 + \chi_{13}\phi_1\phi_3 + \chi_{23}\phi_2\phi_3 \tag{4.4}$$

, and $f_{\mathrm{nonloc}}(\nabla\phi_1, \nabla\phi_2)$ the free energy penalty associated with the formation with concentration gradients:

$$\beta f_{\mathrm{nonloc}}(\partial_x \phi_1, \partial_x \phi_2) = \frac{1}{2}\kappa_{11}(\partial_x \phi_1)^2 + \kappa_{12}\partial_x \phi_1 \partial_x \phi_2 + \frac{1}{2}\kappa_{22}(\partial_x \phi_2)^2 \tag{4.5}$$

, with $\beta = 1/k_B T$. In **Eq. 4.4** N_i is an effective molecular size, normalized by that of the solvent, and χ_{ij} represent mean-field binary interaction parameters. In **Eq. 4.5**, κ_{ij} are gradient energy coefficients[219], assumed concentration-invariant for simplicity.

Based on **Eq. 4.4**, we calculate an approximate ternary phase diagram (**Fig. 4.1b**) for the PEDOT:PPS:glycerol-mixture, using the following parametrization: N_1 = 40, N_2 = 200, χ_{12} = 0.065, and χ_{13} = χ_{23} = 0. These parameters are consistent with the notion that i) the PEDOT chains are shorter than the PSS chains, ii) the effective repulsion between PEDOT and PSS is high enough to make sure the components are (mostly) phase separated in the absence of glycerol and iii) the glycerol indeed acts as a compatibilizer by interacting favorably with both PEDOT and PSS. For simplicity, we assume the net interaction of the glycerol between both the PEDOT and the PSS to be athermal by taking χ_{13} = χ_{23} = 0. This choice is consistent with the fact that PEDOT:PSS is capable of accommodating substantial amount of glycerol[212,213]. A possible difference in the interaction (so $\chi_{13} \neq \chi_{23}$) would, given the fact that the total solids content is high, only result in a marginal tilt in the tie-lines in **Fig. 4.1b**. In other words, it would leave the results of the calculations, as well as the conclusions unaffected. We obtain the binodal curve (dark green) of coexisting compositions in the usual way by applying a Maxwell construction based on equalizing the chemical potentials and the osmotic

pressures in the coexisting phases[219], which themselves are connected by the tie-lines (grey). The spinodal curve (green), *i.e.* the limit of thermodynamic stability, is obtained through the condition: $\det(\mathbf{H}) = 0$, with $\mathbf{H}$ the Hessian matrix of second derivatives of the free energy with respect to the independent volume fractions. The (approximate) position of the critical point (light green) is obtained by interpolation.

The blue (PSS-rich) and red (PEDOT-rich) dots in **Fig. 4.1b** indicate the out-of-equilibrium situation right after the initial glycerol ingress, but before the diffusive redistribution of the polymeric components (*i.e.* PEDOT and PSS), that takes place to set a new equilibrium. From top to bottom, the dots indicate exemplary average glycerol volume fractions of $\bar{\phi}_3$ = 0.55, 0.45, 0.35 and 0.25 in the PEDOT:PSS, for simplicity deemed the same as the fractions in the PVA, as mentioned above. As the system slowly relaxes towards the new equilibrium (represented by the binodal), the arrows show how the phase compositions change during the redistribution. Due to the asymmetry in the phase diagram, the PSS-rich phase will during this process accommodate a significant amount of PEDOT, in particular at high glycerol content. In contrast, almost no PSS enters the PEDOT-rich phase, represented by the fact that the red arrows are very short. Within our model, it is exactly the enrichment of PEDOT in the PSS-rich phase which leads to an enhanced connectivity between the PEDOT-rich domains that we deem responsible for the increase in conductivity.

To demonstrate the actual dynamics of the change in composition in adjacent PEDOT- and PSS-rich domains, we numerically integrate **Eq. 4.1** and **4.2** on a 250 nm wide box, comprising a PSS-rich domain at the left side interfacing a PEDOT-rich domain on the right (see **Fig. 4.1d**), with initial compositions represented by the blue and red symbols in **Fig. 4.1b**. We detail the exact calculation procedure in SI: *Calculation Procedure Polymer Concentration Profiles*. **Fig. 4.1d** shows the result for $\bar{\phi}_3$ = 0.55, plotting the normalized PEDOT concentration as a function of spatial coordinate and time. The results for the other values for $\bar{\phi}_3$ are given in the SI, **Fig. S4.3**. As mentioned, more PEDOT migrates into the PSS-rich phase than the other way around. Concomitantly, mass conservation causes the position of the interface between the domains, roughly indicated by the inflection point in the spatial profile of the PEDOT volume fraction across the domain, to shift from left to right. We schematically indicate this in **Fig. 4.1e**.

To make a comparison with the measured sheet resistance transients in the upper panel of **Fig. 4.1c**, we calculate the total amount of PEDOT in the PSS-rich phase at each time step by integrating the PEDOT concentration profile between x = 0 and the position of the inflection point. The normalized (see SI: *Improving Accuracy and Determining PEDOT Content in the PSS-rich Phase*) results are then plotted as a function of time in the lower panel of **Fig. 4.1c**. Comparing the two panels shows that the decrease in the sheet resistance scales with time in nearly exactly the same way as the increase in the PEDOT content in the PSS-rich phase and confirm a linear correlation after saturation (after 24 h) by plotting (1- ϕ) against the normalized sheet resistance (see **Fig. S4.4**). This strongly supports our mechanistic hypothesis behind the conductivity increase. Moreover, the fact that we reproduce the curvature in the transient stage across the range in glycerol content with only one single value for the fundamental (monomeric) diffusivity (see SI: *Onsager Mobility Matrix*), means that the theory we invoke to describe the inter-diffusion between the three blend components correctly captures the composition-dependence of the plasticization of the PEDOT:PSS matrix.

In summary, we demonstrate that a plasticizer that ingresses a PEDOT:PSS film from an underlying substrate enhances the conductivity of the former in a thermodynamically controlled way. Using a multicomponent diffusion model based on Flory-Huggins free energy we show that this increase in conductivity is established by a slow rearrangement and interdiffusion of both the PEDOT and the PSS after fast initial ingress of the plasticizer. This reorganization leads to an enhanced connectedness of

the PEDOT-rich domains, where the time dependence of the fraction of PEDOT in the PSS-rich phase is similar to that of the sheet resistance.

After allowing PEDOT:PSS to reorganize in response to the glycerol diffusion, the change in electrical performance upon strain is studied. Accordingly, the films are clamped into an in house-built stretch station and elongated in 2 %-steps at a speed of 0.06 mm/s to reach 100 – 200 % strain in total. In contrast to other studies[64,173,186,220,221], we do not apply any kind of pre-stretching to either the substrates or the PEDOT:PSS films. **Fig. 4.2a** depicts the change in min.-max. normalized sheet resistance R_s parallel to the direction of strain. Please see the Methods and Materials section and SI for a detailed description of the sample analysis as well as the absolute R_s and change in absolute resistance R/R_0 plotted against the strain (**Fig. S4.6** and **S4.7**). Consistent with previous reports, we observe a decrease in sheet resistance upon strain. It is noteworthy that a decrease in resistance when stretching pristine spin-coated PEDOT:PSS films has been reported to depend on the substrate[80,81,89]. Using polyimide (PI) substrates, Lee et al.[80,81] attributed this observation to an irreversible growth of PEDOT grains and using SEBS substrates, Vijay et al.[89] linked the slight decrease in resistance for up to 15 % strain to a promoted adhesion to the substrate via van der Waals forces.

***Table 4.1**: Strain at which the minimum sheet resistance R_s and crack-onset strain for PEDOT:PSS on PVA:glycerol (15 – 55 wt%) substrates (average over ≥ 5 films.) are observed.*

glycerol amount	min. R_s at strain	crack-on-set strain
15 wt%	65 %	60 %
25 wt%	84 %	88 %
35 wt%	97%	126 %
45 wt%	130 %	140 %
55 wt%	141 %	160 %

Looking at the normalized R_s in dependence of the strain (**Fig. 4.2a**), the following observations can be summarized: i) Independently of the amount of glycerol incorporated into the substrates (15 - 55 wt%), all curves share the same principle shape, which can be divided into three regimes. In the first regime they exhibit an increase in sheet resistance up until 10 % – 20 % strain. In the second regime they reach a minimum sheet resistance at 65 % – 144 % strain, depending on the glycerol amount (see also **Tab. 4.1**). And in the third regime after the minimum the sheet resistance is increasing with further elongation. ii) The observed minima shift to higher strains with increasing glycerol amounts. iii) The overall decrease in sheet resistance upon stretching becomes more pronounced with an increasing glycerol amount (**Fig 4.2b**). The glycerol-loading dependent effects indicate that the degree of glycerol penetration and plasticization varies within PEDOT:PSS. These observations are in line with the above findings. By incorporating a plasticizer into the underlying substrate, the mechanical properties of the substrate can be adjusted and, as a result of the mobility of the plasticizer between the systems, the ability of the conductive thin film to adapt to strain is improved. This approach provides dual benefit by improving both the flexibility of the substrate and the electrical performance of the thin film under strain simultaneously. In stark contrast to this approach, literature reports of impurities that potentially migrate from the substrate into the conductive layer, decreasing its electrical performance[7]. **Fig. 4.2b** depicts the averaged initial and minimum sheet resistances (R_S) extracted from the data displayed in **Fig. S4.8**. Not only does the initial R_s decrease (consistent with the results presented and discussed in **Fig. 4.1** and **4.2a**), but additionally the minimum R_S shifts to lower values meaning that a higher glycerol loading leads to a higher conductivity at higher strains. The most substantial changes are observed for films containing 55 wt% glycerol: Upon stretching R_s reduces to one fifth of its initial value at 142 % strain. In addition, films containing 55 wt% glycerol show stable electrical properties when cyclically stretched within their elastic range (**Fig. S4.9**).

To better understand how changes in the sheet resistance of PEDOT:PSS relate to the rearrangement of the substrate during elongation, we conduct tensile tests on the pristine PVA:glycerol substrates (**Fig. 4.2c** and **Fig. S4.10**). These tests reveal typical elastomeric behavior, starting with an elastic regime, transitioning to a plastic regime, followed by strain hardening and ultimately leading to sample failure. Interestingly, we observe that the initial increase in R_s upon stretching (up to approx. 20 %, **Fig. 4.2a**) aligns with the elastic deformation regime of the substrates. Within this regime, the PVA polymer chains remain unchanged in their arrangement. However, at higher strains in the plastic regime, the chains are expected to rearrange, forming new hydrogen bonds. The arrangement of the substrate during the plastic deformation regime may contribute to aligning the PEDOT:SS chains, potentially leading to a decrease in R_s both parallel and perpendicular to the direction of strain.

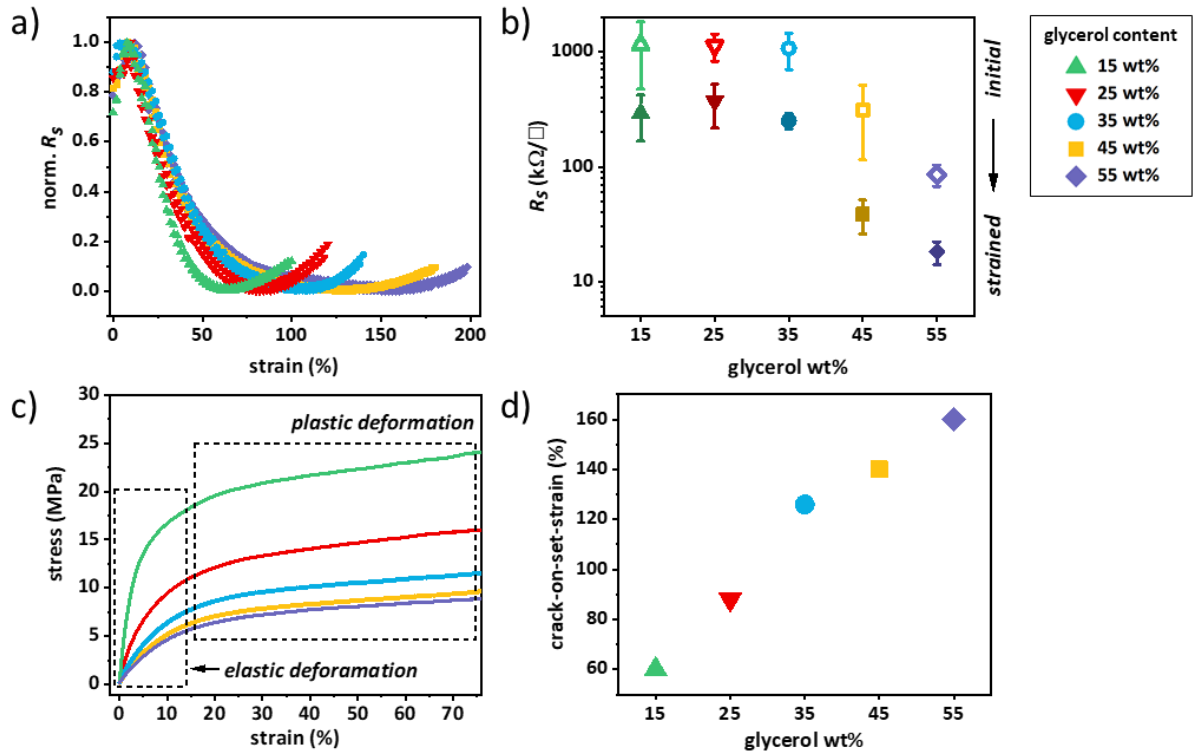

***Figure 4.2**: Electrical performance under strain: **a)** Normalized sheet resistance R_s of PEDOT:PSS films plotted against strain on PVA substrates containing 15 – 55 wt% glycerol. **b)** Initial R_s (open symbols) compared to the minimum R_s in the strained state (filled symbols; 15 wt% glycerol: 65 % strain; 25 wt%: 84 %; 35 wt%: 97 %; 45 wt%: 130 %; 55 wt%: 140 %). **c)** Tensile tests conducted on pristine PVA:glycerol substrates. **d)** Crack-on-set-strain for 15 - 55 wt% glycerol.*

When stretching conductive materials, cracks often lead to a decrease in electrical performance, limiting their maximum elongation[7,9,64–66,80,88]. Furthermore, crack formation may be dependent on the underlying substrate[9,80]. To address this issue, plasticizing surfactants and ionic liquids are frequently added to PEDOT:PSS[64–66]. To study the crack formation (crack-on-set-strain) we use optical microscope imaging and examine the films at different strains on a micrometer scale (see **Tab. 4.1**, **Fig. 4.2d** and **4.3**). Due to the glycerol's plasticizing effect within the PEDOT:PSS, cracks only emerge at higher strains with increasing glycerol content. In all substrates, the emergence of cracks is linked to the observed minimum in sheet resistance during stretching. This is expected, as crack formation leads to an increase in the sheet resistance. Slight variations in the onset strain of cracks and the percentage of strain at which a minimum in sheet resistance is observed may be attributed to slight irregularities in the films. Cracks, typically 2 – 5 µm in size and distributed evenly, increase in size and quantity after

their initial appearance with increasing strain. An optical comparison of the cracks reveals an edge softening with increasing glycerol amount. The retention of conductivity despite cracking can be explained by the presence of sufficient intact conductive pathways, a phenomenon previously reported in the literature[7,63]. Finally, we would like to point out that using our glycerol-loaded substrates no additional surfactant is needed to realize crack-free elongation of PEDOT:PSS of up to 160 %.

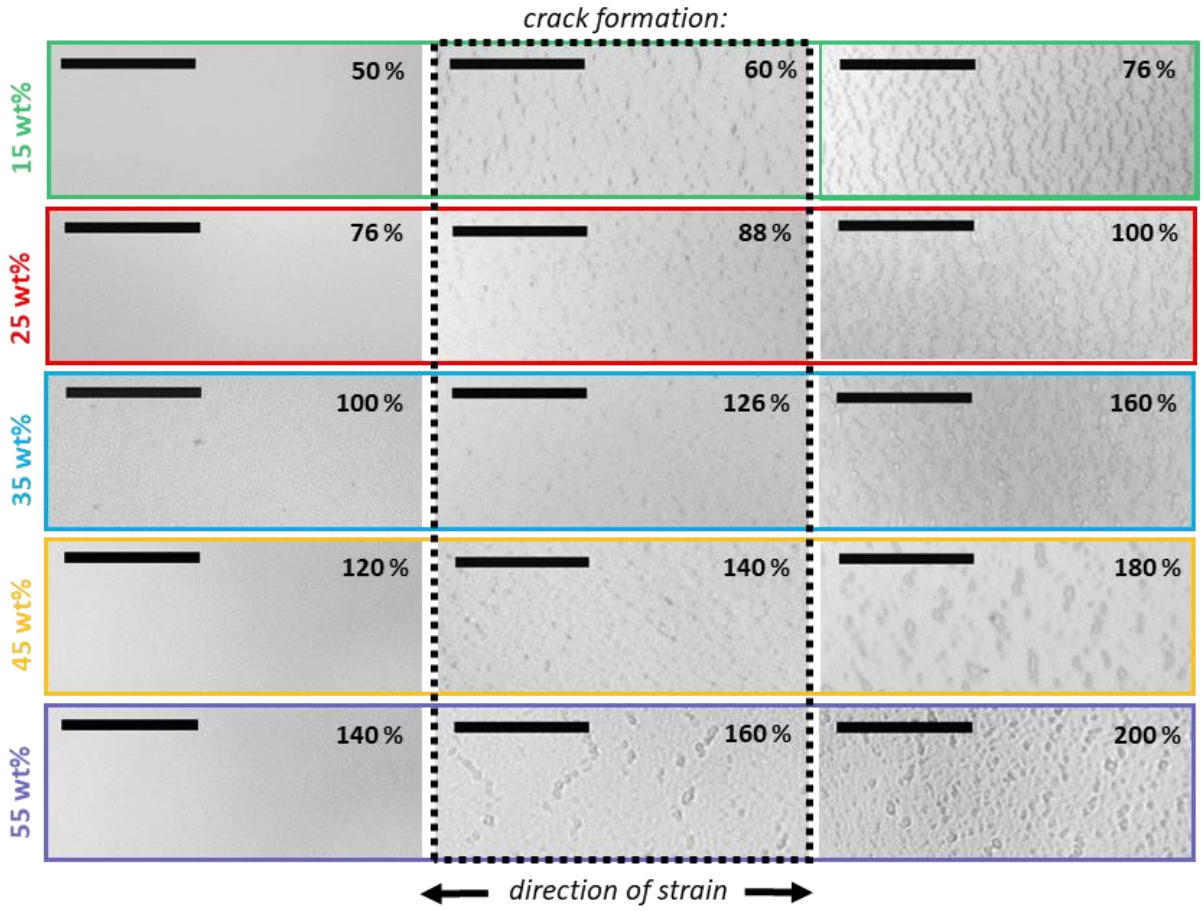

***Figure 4.3**: Crack formation of PEDOT:PSS on PVA:glycerol (15 – 55 wt%) substrates at different strain percentages. All scale bars are 25 µm.*

Scanning force microscopy (SFM) is employed in PeakForce Quantitative Nanomechanical mapping mode to investigate microscale changes. **Fig. 4.4a** depicts 3D topography images within three differently-sized areas of PEDOT:PSS films on PVA:glycerol (55 wt%) and elongated to 120% strain. Please note that the films are kept strained while being examined. 2D topography images can be found in **Fig. S4.11**. The images reveal a valley-like structure aligned with the direction of strain. In line with the microscope images in **Fig. 4.3** (bottom row), no cracks are observed. Upon comparing these images with topography recordings of the pristine PVA:glycerol substrates (55 wt%) under strain, minimal differences are observed (see **Fig. S4.12** for 2D as well as 3D recordings). This suggests that the underlying substrate is primarily responsible for the observed topography.

To investigate changes on a molecular level, we record Broadband Coherent Anti-Stokes Raman Scattering (BCARS) spectra of PEDOT:PSS on PVA: glycerol (45 wt%) substrates at various strains. Please see the SI for a detailed description of the data analysis as well as all related figures (**Fig. S4.14**, **S4.15** and **Tab. S4.2**). In brief, we first analyze blank PVA:glycerol (45 wt%) films, followed by those with transfer-printed PEDOT:PSS. The spectra were then deconvoluted based on the characteristic peaks of

the incorporated components (PEDOT:PSS, PVA and glycerol). PEDOT:PSS was identified through the vibrational modes of its aromatic thiophene rings, corresponding to the quinoid (1438 cm^{-1}) and benzoid (approx. 1443 cm^{-1}) structures. PVA and glycerol were evidenced by their respective peaks at 1443 cm^{-1} and 1463 cm^{-1} (see also **Tab. S4.2**)[222,223,232,233,224–231]. And lastly, to isolate PEDOT-specific changes, spectra were subtracted to eliminate overlapping contributions from PVA and glycerol.

For the PEDOT:PSS-transfer-printed film (**Fig. 4.4b**), at lower strains (16%), we observe an initial blue shift of the main peak (approx. 1440 cm^{-1}) and an increase in the right shoulder (approx. 1460 cm^{-1}), which aligns with changes detected in pristine PVA:glycerol films (**Fig. S4.14a**). However, at higher strains (≥74%), this trend is reversed, with a redshift of the main peak from 1443 cm^{-1} to 1438 cm^{-1} and a reduction in the right shoulder (1443 cm^{-1} and 1463 cm^{-1} sub-peaks). Subtracting the spectra, as described above, reveales a shift in PEDOT's resonant structure: a decrease in the benzoid fraction (1443 cm^{-1}) and an increase in the quinoid fraction (1438 cm^{-1}; red arrows in **Fig. 4.4c**)[224]. This change is typically associated with enhanced charge transport due to the extended-coil arrangement of the quinoid structure[49,69,225] (see **Fig. 4.4d** for chemical structures). While this change is not immediately visible in **Fig. 4.4b** due to overlapping contributions from PVA and glycerol, it becomes evident upon in **Fig. 4.4c**. The change in resonant structure most likely is supported by the PVA chain-alignment, which is identified when examining blank PVA films (**Fig. S4.14a-c**). Additionally, it is noteworthy that the above-described effects become more pronounced with higher glycerol content, e.g. when incorporating 45 wt% glycerol compared to 15 wt% (comparing **Fig. S4.14** and **S4.15**). In conclusion, these measurements reveal molecular-level changes in PEDOT:PSS under strain, driven by diffusion and glycerol-induced plasticization.

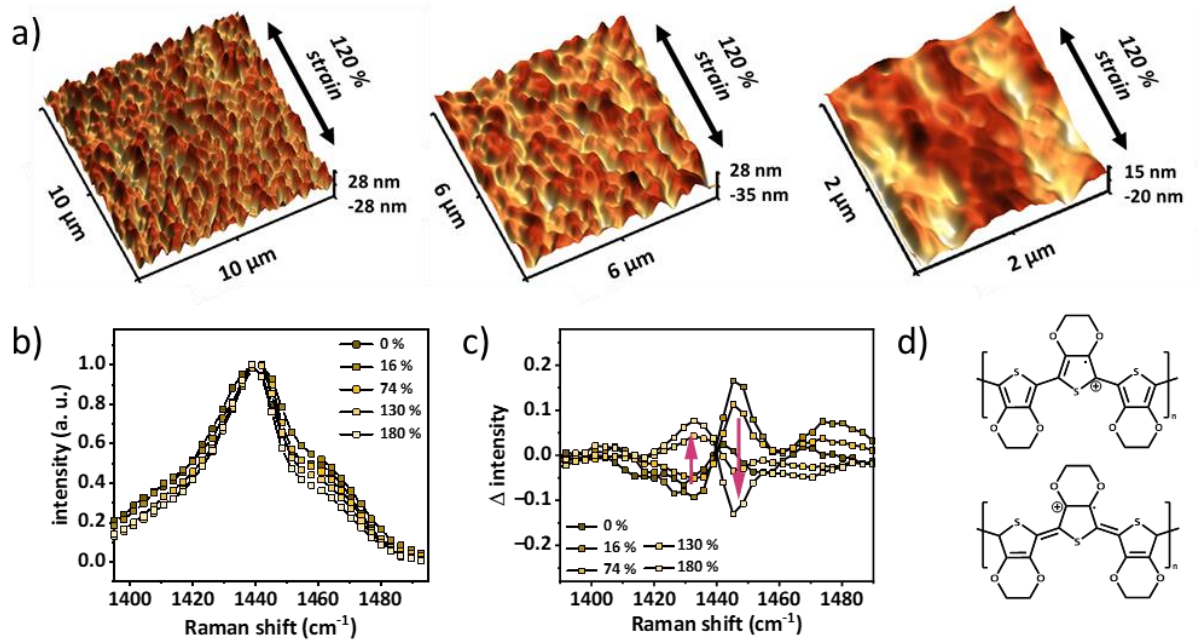

***Figure 4.4**: Properties of strained PEDOT:PSS thin films: **a)** SFM topography images of PEDOT:PSS on top of PVA:glycerol (55 wt%) substrates, strained to 120 %. **b)** BCARS spectra of PEDOT:PSS on PVA:glycerol (45 wt%) at various strains. **c)** Subtracting BCARS spectra of blank PVA:glycerol (45 wt%) from PEDOT:PSS on top of PVA:glycerol (45 wt%) at different strains. **d)** Chemical structures of benzoid and quinoid resonant structures of PEDOT.*

4.4 Conclusions

In conclusion, we introduce a novel, straight-forward and broadly applicable approach for stretchable electronic materials and devices by utilizing the ability of a plasticizer incorporated into the polymer substrate to diffuse into a conductive polymer film (PEDOT:PSS). We closely investigate the interaction between the conductive polymer thin film (PEDOT:PSS), a plasticizer (glycerol) and a supporting substrate (PVA) in a stretchable bilayer system. Detailed insights into how a diffusion-active organic plasticizer induces structural reorganization within PEDOT:PSS, which subsequently leads to increased conductivity and improved strain adaptability, is gained using a multi-component diffusion model incorporating a Flory-Huggins free energy of mixing. A loading-dependent enhanced intermixing effect is found to be responsible for the observed effects. The effect of plasticization is then investigated in detail using various techniques such as electrical characterization, microscopic imaging, SFM and Raman spectroscopy. The improved adaptability to strain leads to a decrease in resistance upon stretching, which is accompanied by a higher onset strain for crack formation and strain-induced PEDOT chain-alignment. With increasing glycerol loading the effects become more pronounced. Incorporating 55 wt% glycerol into the underlying substrate we are able to remarkably decrease the sheet resistance to 20 % of its initial value while simultaneously shifting the crack-onset-strain to 140 %. This fundamental study provides insights into plasticization of PEDOT:PSS and its resulting effects on electrical and morphological properties. Furthermore, it establishes novel approaches towards ductile conducting materials which are applicable in stretchable devices such as OECTs.

4.5 Supplementary Information

Experimental

Materials: PEDOT:PSS (Clevios PH1000, Hereaus Deutschland GmbH), glycerol (PanReac AppliChem, 99 % for synthesis), *iso*-propanol and acetone (honeywell riedel-de haën), PVA (M_w= 31000 – 50000 g/mol, 99 % hydrolyzed; Sigma Aldrich) were used without further purification.

Sample preparation: All samples were prepared and examined under controlled humidity (R_H = 40 – 45 %) and temperature (T = 22 °C) conditions. Sample preparation involved cleaning glass slides (2.5 x 7.5 cm) in an ultrasonic bath with deionized water (5 min), acetone (10 min) and iso-propanol (10 min), followed by drying at 140 °C for 10 min. Subsequently, the slides were treated in an UV/ozone oven for 20 min. Prior to spin-coating, the PEDOT:PSS suspension was kept in an ultrasonic bath for 20 min and filtered (45 µm filter). Spin-coating was performed at 750 rpm for 60 s, and the resulting thin films were dried at 120 °C for 10 min. PVA:glycerol substrates were prepared by combining the components in DI water, stirring at 90 °C for 3 h and subsequent cooling to room temperature. The mixture was then filtered, treated in an ultrasonic bath (10 min) and 1.5 mL of the solution was drop casted onto pre-cleaned glass slides, allowing it to dry. The PEDOT:PSS thin films then were transfer-printed heatless as described in detail in [211] (**Chapter 3**), the average thickness of the PEDOT:PSS thin films was determined to be 70 - 75 nm using a surface profilometer (Bruker, DektakXT Stylus Profiler) and an average over six films.

Electrical characterization: The conductivity (σ) was calculated using the equation $\sigma = l/(R \cdot w \cdot t)$ with the length l, the resistance R, the width w and the thickness t. The sheet resistance was calculated using the following equation: $R_s = 1/(\sigma \cdot t) = R \cdot w/l$. Before stretching, the films were repeatedly contacted to measure the resistance over a period of up to 48 hours. Electrical measurements upon stretching were performed using a home-built set up based on a motorized stretch station synchronized with a Keithley 2000 Multimeter. Gold-coated clamps were utilized for enabling good electrical and mechanical contact during stretching. The films were elongated in ramps with 2 % strain at each step with respect to the initial length and in both directions uniformly. The stretching time was set to 10 s, resulting in a speed of 0.06 mm/s. The wait time at each ramp was 30 s (see **Fig. S4.5** for graphical visualization). Depending on the supporting substrate, 50 – 100 ramps were performed, resulting in an overall strain of 100 – 200 % with the initial length being set to 0 %. One second after the beginning and one second before the end of each performed stretching and waiting period a resistance value was recorded. Data was normalized using a min-max normalization.

Imaging: Optical Microscopy: Microscopic images were recorded in bright field mode and edited using a confocal microscope (Leica DM6000 M) and the according software (Leica Application Suite Version 4.12.0). The strained films were secured on glass slides using double-sided tape. SFM: PeakForce-Quantitative Nanomechanical Mapping (PF-QNM) SFM measurements were performed using a Bruker Dimension ICON platform using OLTESPA NanoAndMore cantilevers (frequency: 70 KHz, spring constant: 2 N/m, back/ tip side coating: Al). Images recorded in strained state were subject to Fourier transformation to eliminate the periodicity induced by the film's vibration during the measurement.

Tensile tests were performed on a materials testing machine Z005 (Zwick/Roell, Germany). Bone shape films with 4.5 mm width, 32 mm length and thicknesses of around 0.1 mm were elongated with a rate of 20 mm/min at room temperature. A pre-load of 0.1 N was used in all experiments and stress vs strain characteristics were recorded.

Diffusion of Glycerol

The set of data showed in **Fig. S4.1** was collected and analyzed to understand the glycerol-triggered PEDOT and PSS re-arrangement. To achieve this, the sheet resistance of all eight films within each dataset was averaged and then min-max normalized ($x' = (x - x_{min})/(x_{max} - x_{min})$) relative to the averaged minimum of the film containing 55 wt% glycerol. The obtained data is displayed on the bottom right (**Fig. S4.1f**; identical to **Fig. 4.1c**).

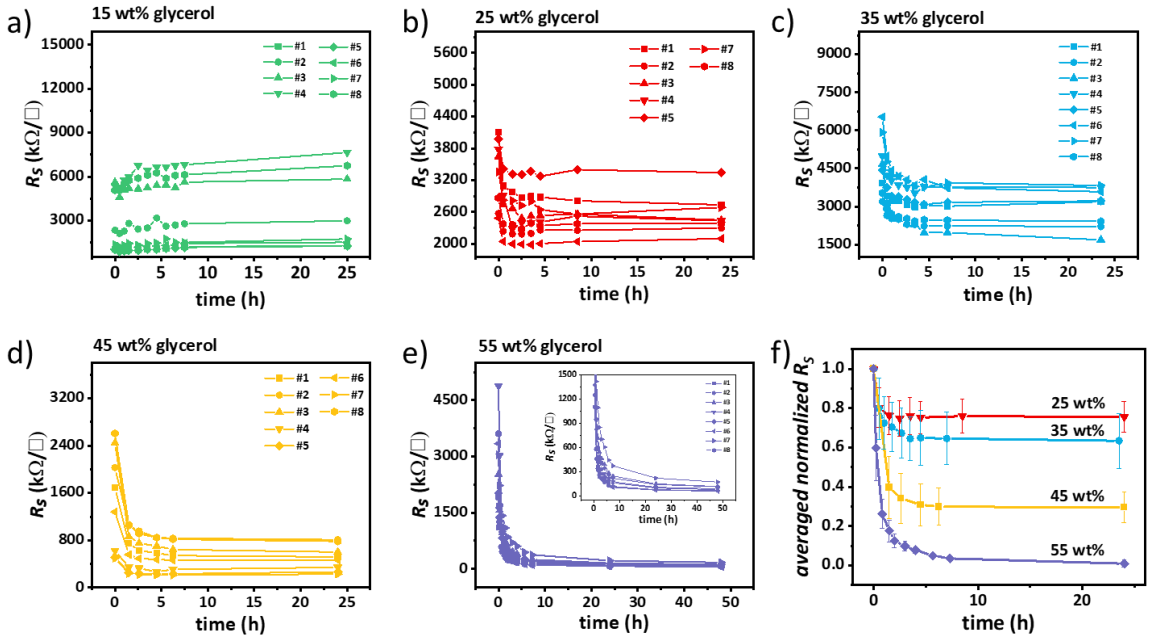

***Figure S4.1**: **a-e)** Time-dependent change in sheet resistance R_S of PEDOT:PSS on PVA substrates containing 15, 25, 35, 45 and 55 wt% glycerol (0 % strain). **f)** Averaged normalized sheet resistances over time of transfer-printed PEDOT:PSS on glycerol-loaded PVA substrates.*

Experimental Curve Fitting

To test whether the transient increase in conductivity of the PEDOT:PSS could be directly related to actual diffusion of glycerol from the PVA substrate into the PEDOT:PSS film, we fitted the normalized resistivity versus time data to the following empirical exponential function to extract a characteristic resistivity decay time τ:

$$f(t) = (1 - y_0)\exp\left(-\frac{t}{\tau}\right) + y_0 \qquad \text{(S4.1)}$$

, with *t* indicating time and y_0 a constant off-set. The experimental data and fits are shown in **Fig. S4.1**. The obtained values for y_0 and τ are listed in **Tab. S4.1**. As mentioned in the main text, despite the fact that the fits have reasonable quality, the obtained values for τ is for all glycerol loading orders of magnitude higher than what would be expected if the decrease in resistivity were dominated by the actual diffusive ingress of glycerol from the PVA into the PEDOT:PSS. Illustratively, if we, for simplicity, assume an effective film thickness of the order $\bar{l}$ = 10^2 nm, we find effective diffusivities $D_{EFF} = \bar{l}^2/\tau$ in the range: 10^{-18} – 10^{-19} m^2/s. Indeed, this fast ingress causes an initial swelling of the PEDOT:PSS film, which occurs too fast to allow for measurement.

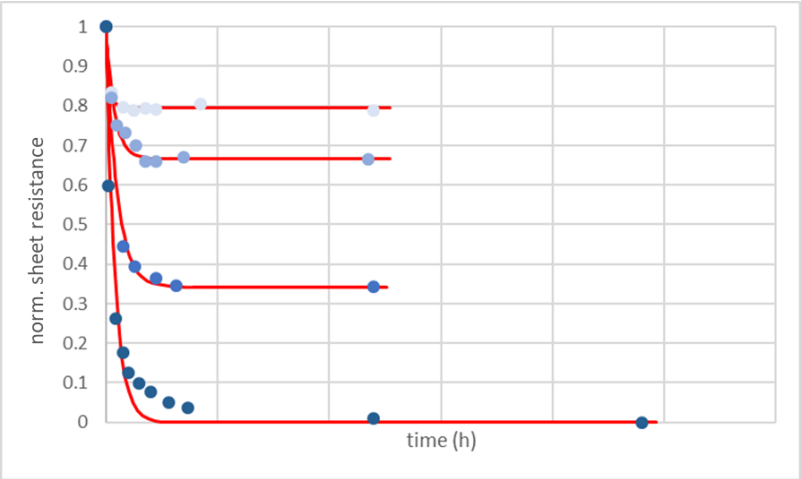

Figure S4.2. *Normalized sheet resistance plotted as a function of time. Points are measured data and lines are fits based on* ***Eq. S4.1****. The shades of blue correspond to substrate glycerol loadings of 25%, 35%, 45% and 55% from light to dark.*

Table S4.1: *Fit values obtained from fitting* ***Eq. S4.1*** *to the experimental resistivity versus time data.*

glycerol loading	τ (hours)	y_0
25%	0.3	0.795
35%	0.75	0.666
45%	1.0	0.342
55%	0.8	0

Onsager Mobility Matrix

As in previous work[215,216,234], the Cahn-Hilliard simulations in this work utilize the fast mode diffusion formalism[235] to correctly implement mass transport under the constraint of incompressibility. For an n-component mixture the mobility coefficients are given by:

$$\Lambda_{ij}(\mathbf{r},t) = \phi_i(\mathbf{r},t)\phi_j(\mathbf{r},t)\sum_{k=1}^{n}\lambda_k + \left(\delta_{ij} - \phi_i(\mathbf{r},t)\right)\lambda_j - \phi_j(\mathbf{r},t)\lambda_i \quad \text{(S4.2)}$$

, with $\lambda(\mathbf{r},t)$ the diagonal elements of the Onsager mobility matrix. For component i we write:

$$\lambda_i(\mathbf{r},t) = \phi_i(\mathbf{r},t)N_i D_i \quad \text{(S4.3)}$$

, with N_i and D_i molecular size and tracer diffusivity. Assuming free draining, Rouse-like mass transport, the latter is related to that of a fundamental monomeric diffusivity D_0 according to: $D_i = D_0/N_i$. As before, we neglect the off-diagonal contributions of the Onsager mobility matrix[217]. With a fixed value of D_0 = 2×10^{-4} µm^2/s, we reproduce the experimentally observed kinetics for the increase in conductivity with time.

Calculation Procedure Polymer Concentration Profiles

We evolved the concentration profiles of PEDOT ($\phi_1(x,t)$) and PSS ($\phi_2(x,t)$) in time by numerically solving the Flory-Huggins-Cahn-Hilliard Equations (1) and (2) (main text) in one space dimension on a domain $\tilde{X}$ containing 50 grid points $0 \leq \tilde{x} \leq 49$, with a grid spacing of 5 nm (so in dimensional units: $0 \leq x \leq 250$ nm). The initial concentration profiles of PEDOT (component 1), PSS (component 2) and glycerol (component 3) are predefined by the following expressions:

$$\phi_{i=1,2}(\tilde{x},0) = \frac{1}{2}\left[\phi_i^{(\infty)}(0) - \phi_i^{(-\infty)}(0)\right]\left\{1 + \tanh\left[a\left(\tilde{x} - \frac{1}{2}\tilde{X}\right)\right]\right\} + \phi_i^{(-\infty)}(0) \quad \text{(S4.4)}$$

$$\phi_3(\tilde{x},0) = 1 - \phi_1(\tilde{x},0) - \phi_2(\tilde{x},0) = \text{const} \quad \text{(S4.5)}$$

, with $\phi_i^{(\infty)}(0)$ and $\phi_i^{(-\infty)}(0)$ the initial volume fractions in the two phases, *i.e.* right after swelling. These are given by:

$$\phi_{i=1,2}^{(-\infty)}(0) = \left(1 - \phi_3^{(-\infty)}(0)\right)\phi_i^{(\alpha)} \quad \text{(S4.6)}$$

$$\phi_{i=1,2}^{(\infty)}(0) = \left(1 - \phi_3^{(\infty)}(0)\right)\phi_i^{(\beta)} \quad \text{(S4.7)}$$

, with $\phi_3^{(\mp\infty)}(0)$ the initial (given) volume fractions of glycerol in the PEDOT- and PSS rich phase, taken as $\phi_3^{(-\infty)}(0) = \phi_3^{(\infty)}(0) \epsilon \{0.2, 0.3, 0.4, 0.5\}$, as explained in the main text. $\phi_i^{(\alpha)}$ and $\phi_i^{(\beta)}$ represent the binodal volume fractions of PEDOT and PSS before swelling with glycerol in, respectively, the PSS- and PEDOT rich phases. The composition of the 'dry' phases is given by the ternary phase diagram for ϕ_3 = 0. We have: $\phi_1^{(\alpha)}$ = 0.054; $\phi_2^{(\alpha)}$ = 0.946; $\phi_1^{(\beta)}$ = 0.996; $\phi_2^{(\beta)}$ = 0.004. The stiffness coefficients are taken sufficiently high to ensure that the interface between the coexisting phases is described by a minimum of ~5 grid points. We assume that only the two polymers contribute measurably to the stiffness in the concentration fields due to the typically large entropic penalty near the interface, which does not occur for small molecular species. For simplicity we assume the same stiffness parameter for both polymers: $\frac{\kappa_{11}}{k_B T}$ = $\frac{\kappa_{22}}{k_B T}$ = 1.0 nm^2 and $\frac{\kappa_{12}}{k_B T}$ = 0.

Starting with the initial conditions given above, the materials are allowed to redistribute upon relaxation to equilibrium. The numerical simulations are performed on a time domain of 128000 s, using a time step of 0.05 s. To solve **Eq. S4.1** and **S4.2** we used a forward-time-central-space (FTCS) explicit finite difference scheme. Every 64 s, the concentration fields are stored. To determine the total amount of PEDOT in the PSS-rich phase as a function of time, we integrate each stored PEDOT concentration profile $\phi_1(\tilde{x},t)$ in the interval $0 \leq \tilde{x} \leq \tilde{x}_s(t)$, with $\tilde{x}_s(t)$ the position of the inflection point. The latter is determined by the maximum in the numerical derivative of composition with respect to coordinate.

Improving Accuracy and Determining PEDOT Content in the PSS-rich Phase

In order to improve the accuracy in the determination of the position of the inflection point, as well as the spatial integration of the concentration profile (see below) without having to increase the number of calculated points against considerable computational cost, we interpolate additional points between each pair of adjacent calculated compositions using the Matlab cubic spline interpolation routine spline().m. **Fig. S4.3** shows for $\phi_3^{(-\infty)}(0) = \phi_3^{(\infty)}(0) = 0.25, 0.35, 0.45, 0.55$ the bare calculated concentration profiles (points), as well as the interpolated curves as a function of time (lines). To obtain the amount of PEDOT in the PSS-rich phase, we numerically integrate the interpolated PEDOT concentration profiles between position x = 0 and $x = x_I(t)$, with $x_I(t)$ the position of the inflection point as a measure for the position of the interface between the PSS- and PEDOT-rich phase. This position coincides with the maximum in the first spatial derivative (orange curves). The latter is determined using the Matlab function diff().m. To facilitate the comparison with the experimentally measured conductivity curves, we normalized the integrated time profiles for the different glycerol levels by the value obtained for the dry film (*i.e.* 0% glycerol). The data was then normalized by the plateau (equilibrium) value of the film with the highest (55%) glycerol content.

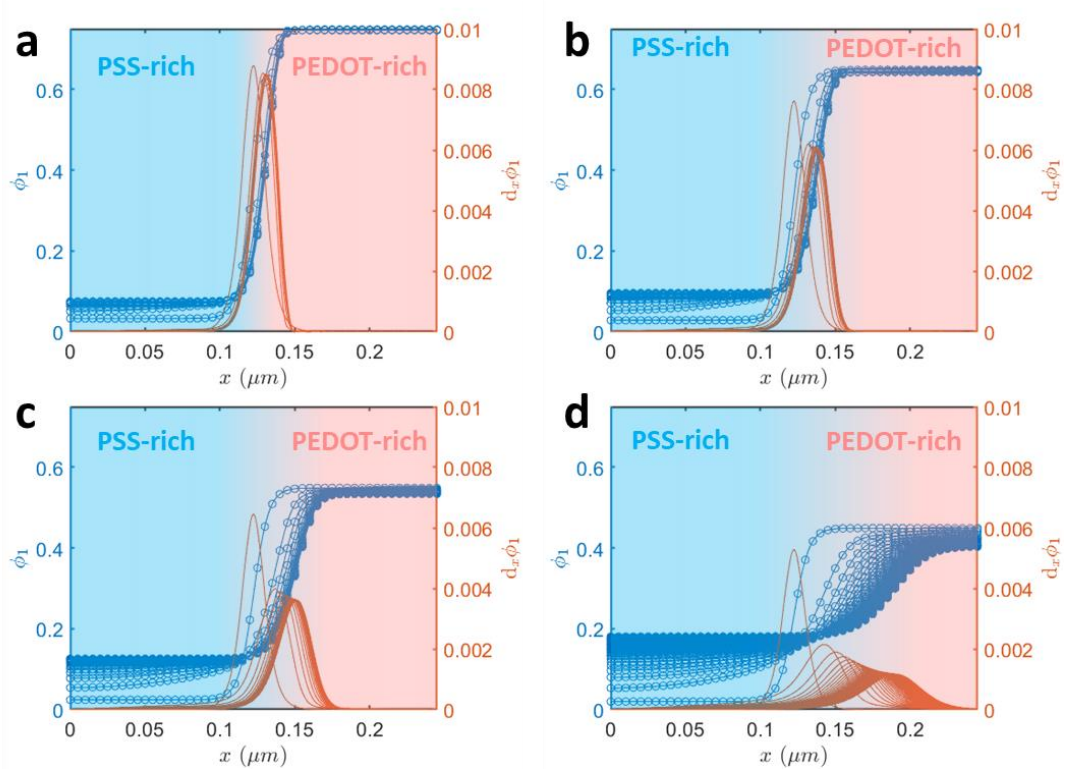

Figure S4.3. *Calculated and interpolated PEDOT volume fractions, plotted as a function of time and lateral coordinate, assuming* $\phi_3^{(-\infty)}(0) = \phi_3^{(\infty)}(0) = 0.25, 0.35, 0.45, 0.55$ *(panel* ***a – d****). The open circles represent the calculated data, obtained by numerically solving Cahn-Hilliard* ***Eq. 4.1*** *and* ***4.2*** *(see main text) on a 50-point grid. The blue lines are obtained by a cubic spline interpolation. The inflection point in the concentration profiles is given by the maximum of the first spatial derivative of the interpolated curves (orange curves).*

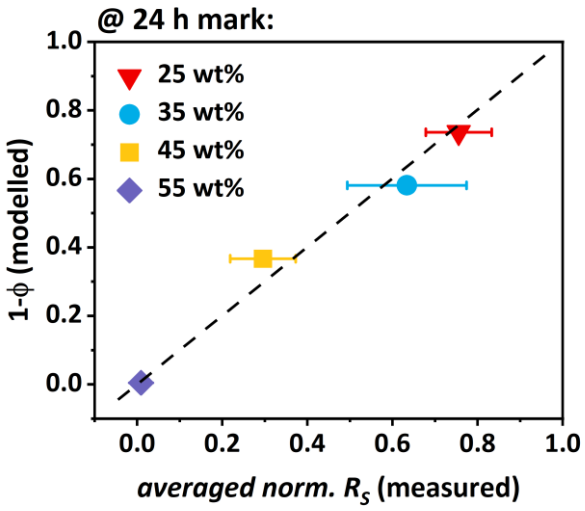

Figure S4.4: *Normalized fraction of PEDOT in the PSS rich phase (derived from modelling) vs. averaged normalized sheet resistances (measured) for PEDOT:PSS on PVA-substrates containing 25 – 55 wt% glycerol. Both sets of values were extracted from the data presented in* ***Fig. 4.1c*** *at the 24-hour time mark. For improved clarity, the data derived from modelling (ϕ) is plotted as (1- ϕ).*

Electrical Characterization

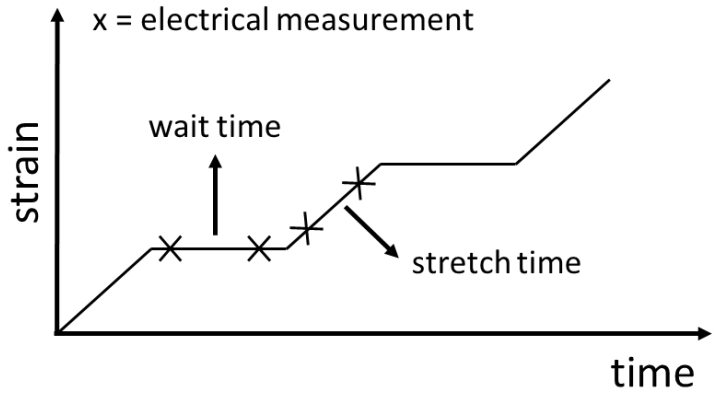

***Figure S4.5**: Graphical illustration of elongation process. 'x' indicates the recording of electrical data. This means that for each straining step two data points were recorded. Furthermore, we only strained in the forward direction.*

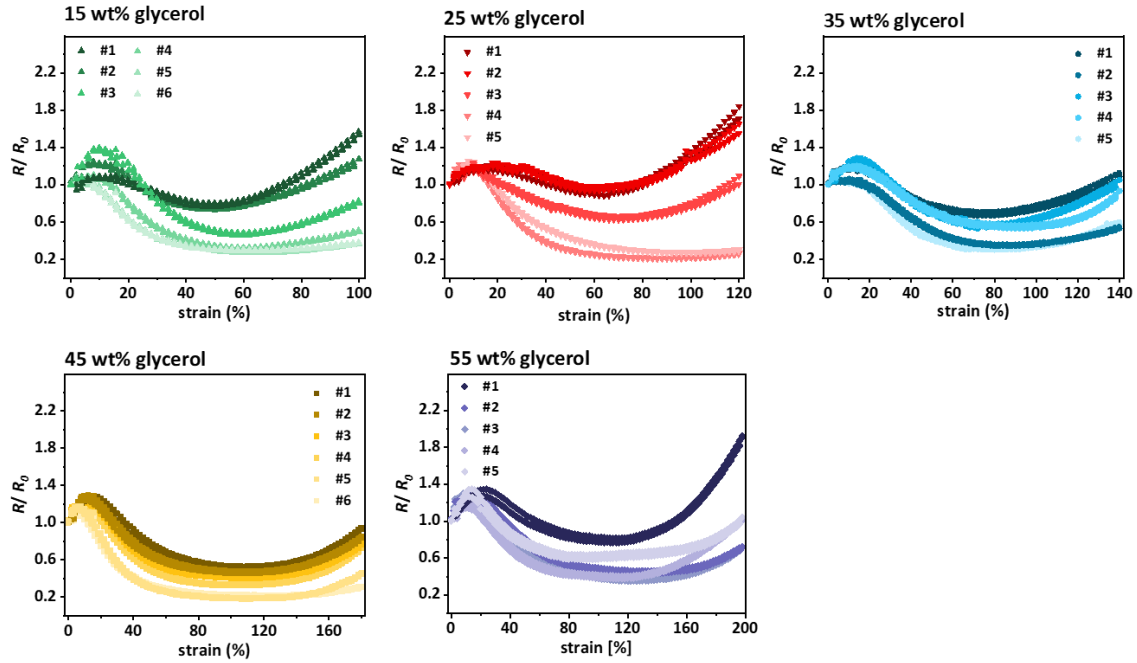

***Figure S4.6**: Change in resistance (R/R_0) upon stretching of PEDOT:PSS on PVA substrates containing 15, 25, 35, 45 or 55 wt% glycerol.*

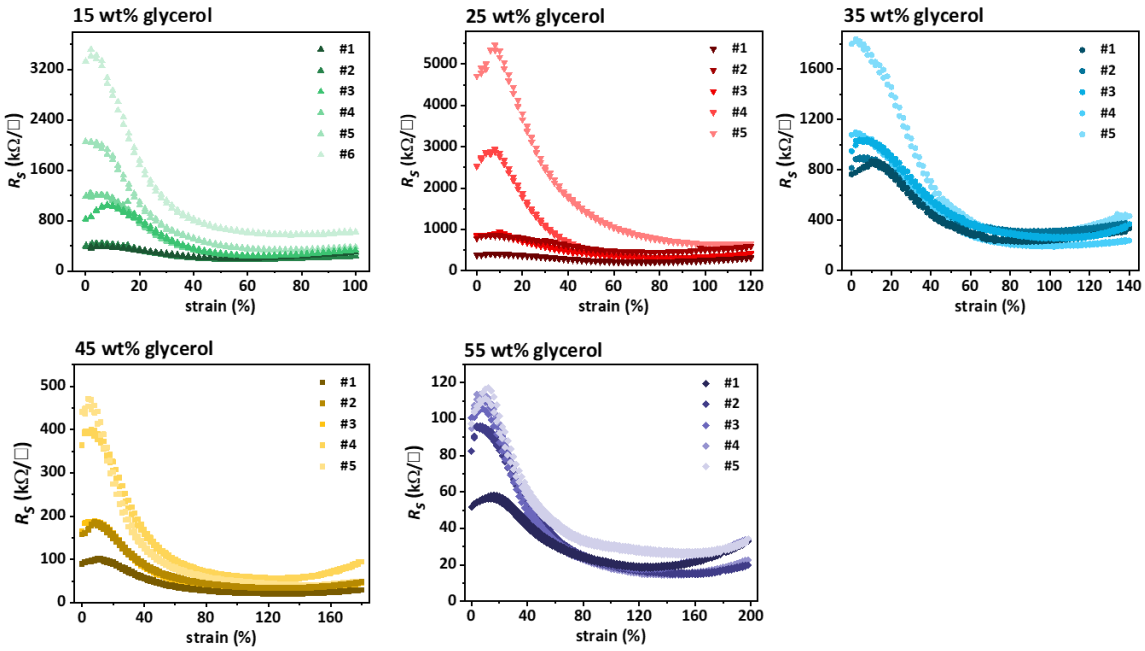

***Figure S4.7**: Sheet resistance (R_s) upon stretching of PEDOT:PSS on PVA substrates containing 15, 25, 35, 45 or 55 wt% glycerol.*

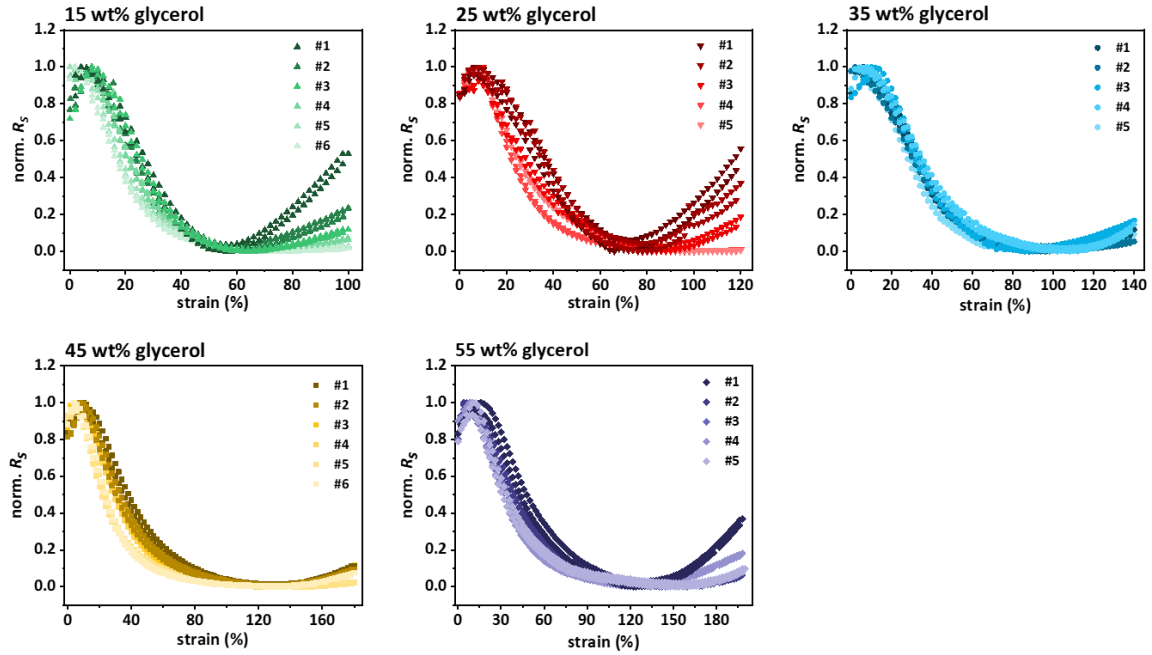

***Figure S4.8**: Min.-max. normalized sheet resistance (R_s) upon stretching of PEDOT:PSS films on PVA substrates containing 15, 25, 35, 45 or 55 wt% glycerol.*

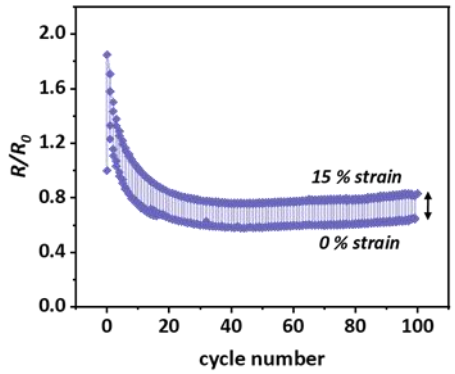

Figure S4.9: *R/R_0 for repeated stretching cycles in the elastic range of PVA:glycerol (55 wt%) substrates. The films were stretched 100 times to 15% elongation (speed: 0.15 mm/s; wait time in elongated and returned state: 30 sec).*

Tensile Tests

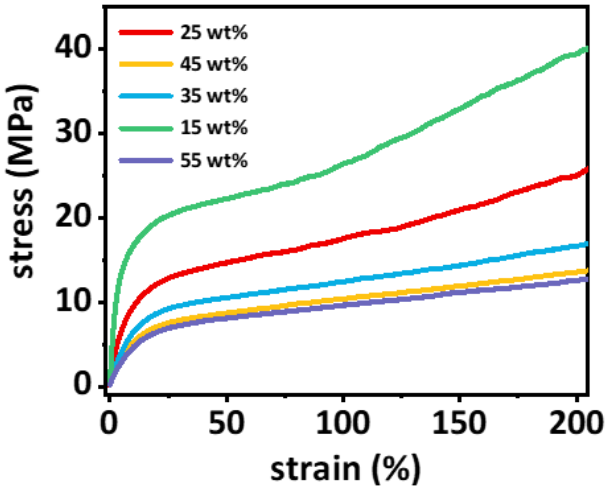

Figure S4.10: *Stress-strain curves for PVA:glycerol substrates at different weight percentages of glycerol (15, 25, 35, 45 and 55 wt%).*

Scanning Force Microscopy

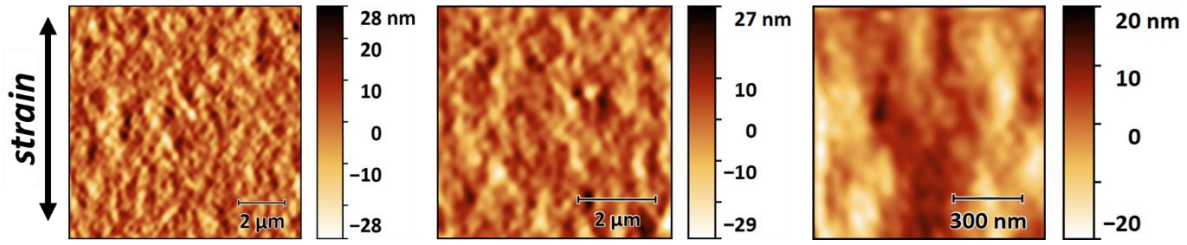

***Figure S4.11**: 2D topography images of PEDOT:PSS films on PVA:glycerol (55 wt%) substrates at 120 % strain. Areas from left to right: 10 x 10 µm, 6 x 6 µm and 2 x 2 µm.*

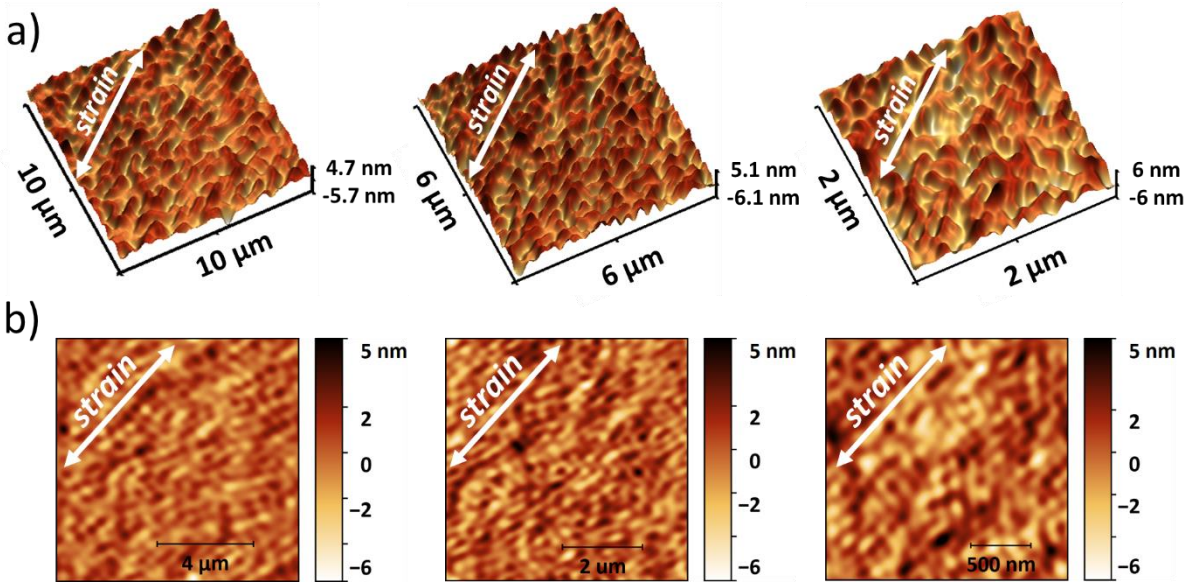

***Figure S4.12**: a) 2D and b) 3D topography images of PVA:glycerol (55 wt%) substrates at a strain of 120 %. Areas from left to right: 10 x 10 µm, 6 x 6 µm and 2 x 2 µm.*

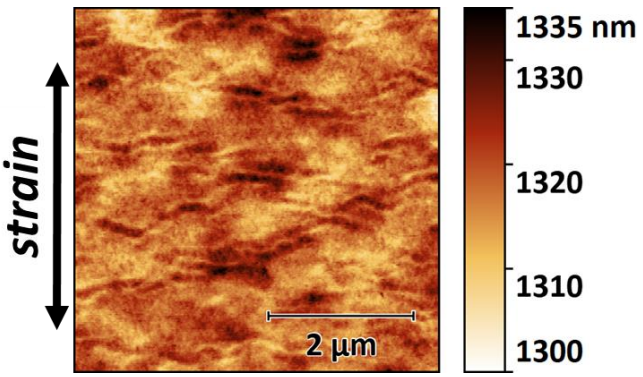

***Figure S4.13**: 2D topography images of PEDOT:PSS films transfer-printed onto PVA:glycerol (45 wt%), strained to 108 % and examined after release.*

Raman Spectroscopy

*Data acquisition and analysis***:** Raman measurements were performed using a home-built broadband coherent anti-Stokes Raman scattering (BCARS) microscope, described in detail elsewhere.[236] Briefly, the pump/probe and Stokes pulses are generated in a dual-output subnanosecond laser source (CARS-SM-30, Leukos). These pulses are then synchronously superimposed in space and time at the sample plane of an inverted microscope (Eclipse Ti-U, Nikon) and tightly focused onto the sample using a 0.85 NA air objective (LCPlan N, Olympus). The BCARS signal, once isolated from the excitation pulses, is focused onto the slit of a spectrograph (Shamrock 303i, Andor). And the dispersed spectral components finally reach a cooled CCD camera (Newport DU920P-BR-DD, Andor). Samples were positioned with the coverslip facing the collector and scanned using a piezo stage (Nano-PDQ 375 HS, Mad City Labs) controlled by LabView 2015 software (National Instruments). The collected hyperspectral data were processed in IgorPro (WaveMetrics). The Raman-like spectra were retrieved through a modified Kramers-Kronig transform.[237] All spectra presented here were phase-retrieved using glass alone, without macromolecules as a reference spectrum and any background phase is removed using a Savitzky-Golay filter with a 2nd order polynomial and a window size of approximately 400 cm^{-1}. This protocol allowed the acquisition and interpretation of high-quality spectral data. For the final spectra analysis and deconvolution in the 1390 to 1490 cm^{-1} range, a custom Python script was developed. This script was instrumental in generating initial parameter seeds for the Lorentzian sub-peaks, derived from the normalized spectra within the specified range. To obtain these initial parameters, characteristic peaks specific to PEDOT:PSS, PVA and glycerol were manually identified, fed into the peak analysis module of the OriginLab Pro software and further refined for the deconvolution process, thereby achieving the final resolution of each peak. Details of the deconvolution process, including the parameters used, are given in **Tab. S4.2**.

*Experimental setup***:** Blank PVA:glycerol samples containing either 15 wt% or 45 wt% glycerol and samples with attached PEDOT:PSS were elongated and affixed to glass slides using double-sided tape. Considering that the PEDOT:PSS film is substantially thinner (approximately 1:1000) than the supporting PVA:glycerol substrate and both layers exhibit signals in the Raman broadband range (1380 - 1480 cm^{-1}), a comprehensive sample analysis was conducted. For each sample, spectra were obtained, deconvoluted and classified into five sub-peaks, representing PVA, glycerol and PEDOT:PSS if present. The assignments are as follows: artificial sub-peak positions collectively describing aromatic thiophene rings of PEDOT: 1412 cm^{-1} and 1434 cm^{-1}, PEDOT:PSS-quinoid structure: 1438 cm^{-1}, PEDOT:PSS-benzoid structure as well as PVA (vibration mode): 1443 cm^{-1} and glycerol (vibration mode): 1463 cm^{-1} [222,223,232,233,224–231] (see also Table S2). Following deconvolution, the peaks were integrated, subtracted from one another and plotted against the strain. Please note that spectra recorded at 0 % strain were omitted from analysis due to substantial material transformations at minimal strains, not allowing for a reliable data analysis. This finding might provide an additional explanation for the initially observed dip in conductivity for up to 20 % strain in **Fig 4.2a**. Nevertheless, we believe that the exclusion of unstrained samples from our analysis does not compromise the validity or the integrity of the observed trends. **Fig. S4.14** summarizes the obtained spectra for samples with 45 wt% glycerol, while spectra for samples with 15 wt% are provided in **Fig. S4.15**.

Analyzing blank strained PVA:glycerol (both 15 wt% and 45 wt%) substrates resulted in a blue shift of the maximum and left concave-upwards Raman band. This led to a decrease in the area of sub-peaks at 1412 cm^{-1} and 1434 cm^{-1}, coupled with an increase in the area of sub-peaks at 1438 cm^{-1} and 1443 cm^{-1} (**Fig. S4.14 a-c** and **S4.15 a-c**).

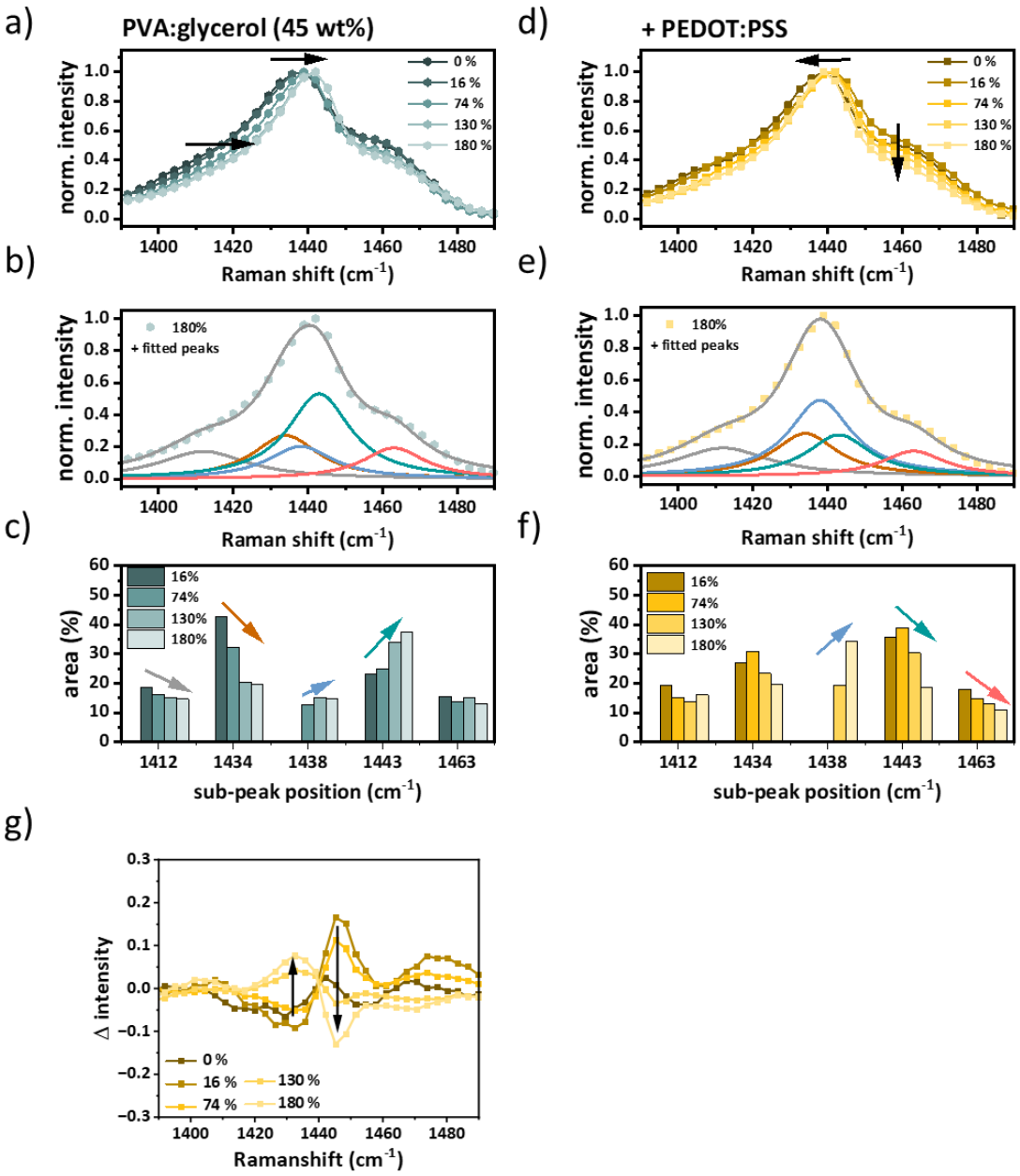

Figure S4.14*: BCARS studies of PEDOT:PSS on PVA:glycerol (45 wt%) substrates.* ***Left****: Examining the blank PVA:glycerol (45 wt%) substrates:* ***a)*** *BCARS spectra of blank PVA:glycerol (45 wt%) at various strains.* ***b)*** *fitted and deconvoluted spectra at 180 % strain.* ***c)*** *Area changes in deconvoluted sub-peak position for each strain.* ***Right****: Examining PEDOT:PSS atop PVA:glycerol (45 wt%) substrates:* ***d)*** *BCARS spectra of PEDOT:PSS atop PVA:glycerol (45 wt%) at various strains.* ***e)*** *fitted and deconvoluted spectra at 180 % strain.* ***f)*** *Area changes in deconvoluted sub-peak position for each strain.* ***Bottom****:* ***g)*** *Subtracting BCARS spectra of blank PVA:glycerol (45 wt%) from PEDOT:PSS on top of PVA:glycerol (45 wt%) at different strains.*

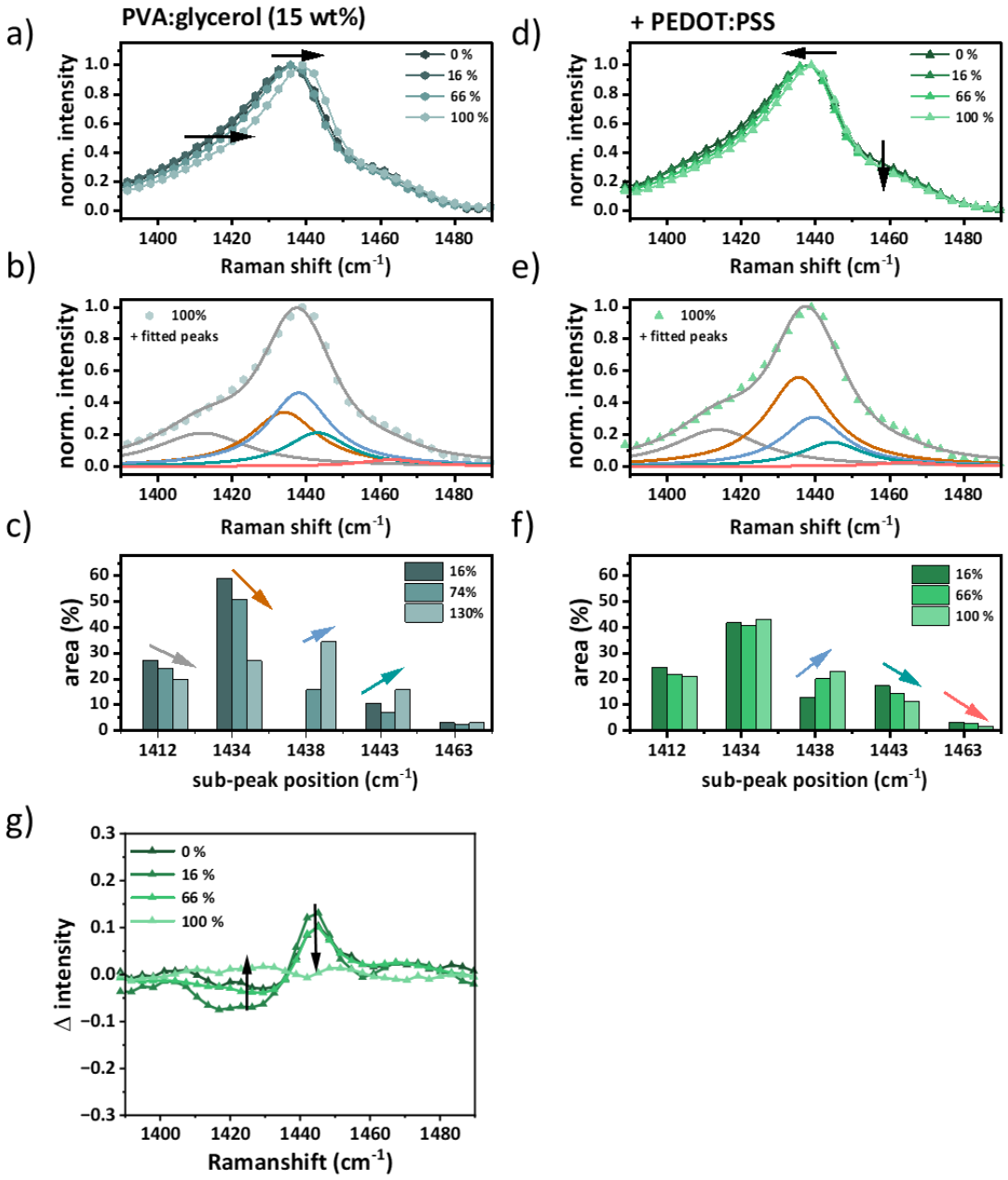

Figure S4.15*: BCARS studies of PEDOT:PSS on PVA:glycerol (15 wt%) substrates.* ***Left****: Examining the blank PVA:glycerol (15 wt%) substrates:* ***a)*** *BCARS spectra of blank PVA:glycerol (15 wt%) at various strains.* ***b)*** *fitted and deconvoluted spectra at 100 % strain.* ***c)*** *Area changes in deconvoluted sub-peak position for each strain.* ***Right****: Examining PEDOT:PSS atop PVA:glycerol (15 wt%) substrates:* ***d)*** *BCARS spectra of PEDOT:PSS atop PVA:glycerol (15 wt%) at various strains.* ***e)*** *fitted and deconvoluted spectra at 100 % strain.* ***f)*** *Area changes in deconvoluted sub-peak position for each strain.* ***Bottom****:* ***g)*** *Subtracting BCARS spectra of blank PVA:glycerol (15 wt%) from PEDOT:PSS on top of PVA:glycerol (15 wt%) at different strains.*

***Table S4.2**: Seed parameters for BCARS peak deconvolution with initial position, initial FWHM and initial area plus freedom each.*

sub-peak number	**1**	**2**	**3**	**4**	**5**
initial position	1412 cm^{-1}	1434 cm^{-1}	1438 cm^{-1}	1443 cm^{-1}	1463 cm^{-1}
position freedom	± 0 cm^{-1}	± 0 cm^{-1}	± 0 cm^{-1}	± 0 cm^{-1}	± 0 cm^{-1}
initial FWHM	35 cm^{-1}	25 cm^{-1}	25 cm^{-1}	25 cm^{-1}	25 cm^{-1}
freedom of initial FWHM	± 0 cm^{-1}	± 0 cm^{-1}	± 0 cm^{-1}	± 0 cm^{-1}	± 0 cm^{-1}
initial area	0 %	0 %	0 %	0 %	0 %
area freedom	∞ %	∞ %	∞ %	∞ %	∞ %

5. On the Effects of Strain in Intrinsically Stretchable Organic Electrochemical Transistors

Chapter details

Authors:

Carla Volkert, Renan Colucci, Pol Besenius, George G. Malliaras and Ulrike Kraft

Author contributions:

C. Volkert: Conception, planning and execution the experiments. Interpretation of the results and writing of the manuscript.

R. Colucci: Support in modelling and analyzing the OECT data. P. Besenius and G. G. Malliaras: Discussion on the concept and the results. U. Kraft: Supervision of the project. Discussion on the concept and the results and editing of the manuscript.

5.1 Abstract

Organic electrochemical transistors (OECTs) are mixed conductor devices that operate through the coupling of electronic and ionic transport. When OECTs are subjected to strain, changes in the geometry and morphology of the organic polymer semiconductor affect device performance, including both types of charge transport. However, detailed studies on these fundamental relationships are lacking. To address this gap, we developed a fully stretchable OECT in two configurations: with strain applied either parallel or perpendicular to the channel and hence the direction of the current. We study how strain-induced geometric changes influence transfer characteristics, electrolyte resistance, turn-off voltage and charge time, finding that both configurations display opposite trends for all parameters. Notably, the parallel configuration demonstrates a 51 % increase in the normalized transconductance under maximum strain, along with a decrease in turn-off voltage and the device charge time. Strain-induced morphological changes of PEDOT:PSS on hole mobility and ion uptake are also investigated, revealing anisotropic behavior in hole mobility under strain: mobility increases in the parallel configuration and decreases in the perpendicular configuration. Independently of the configuration, film capacitance, which measures ion uptake in the channel, decreases under strain. However, in the parallel configuration, the mobility increase outweighs the capacitance reduction, resulting in enhanced OECT transconductance. These findings emphasize the need to consider all factors affecting OECT performance to optimize functionality under strain.

5.2 Introduction

The field of bioelectronics aims to develop and study electronic devices that integrate and monitor biological processes[19]. Since a large number of fundamental biological mechanisms—such as cellular signaling, molecular interactions and ion transport—depend on ionic charge movement[21], electronic devices capable of mixed ionic-electronic transport, like organic electrochemical transistors (OECTs), hold great promise for bioelectronic applications. OECTs are three-terminal devices recognized for their high signal amplification, low operating voltages and easy processability[116,118]. In an OECT, the organic semiconductor channel, positioned between the source and drain electrodes, interacts with an electrolyte that connects it to the gate electrode. The ion migration between the electrolyte and the channel modulates the channel current. By modifying the gate electrode's surface with specific materials, OECTs can detect analytes by measuring voltage changes, making them powerful sensors[11,238]. Furthermore, their soft, biocompatible channels allow them to connect smoothly with cells and tissues and thus monitor, for example, cell layer integrity[239] and brain activity[125]. To enhance these interactions and ensure seamless integration into the human body—while also minimizing scar tissue formation, which is often associated with rigid materials like glass—stretchable OECTs have gained increasing attention. Leveraging their flexibility, stretchable OECTs have been explored in diverse applications, including soft implants[16], health monitoring devices[105] and biosensors[124].

However, achieving fully stretchable OECTs remains a challenge, as reliable device performance under mechanical deformation requires careful optimization of each component. This involves both material selection and fundamental performance studies. The choice of materials includes investigating both conducting and insulating components, such as different supporting substrates (insulating)[7–9,173], organic mixed ionic-electronic conductors (OMIECs)[58,105,107,173] and various OMIEC morphologies, such as honeycomb and continuous films[58,107]. Among the studied OMIECs, poly(3,4-ethylenedioxythiophene):poly(styrenesulfonate) (PEDOT:PSS) stands out as a particularly popular choice. However, its inherent brittleness[7,42] (< 5 % strain tolerance[62]) needs addressing prior to its usage in stretchable OECTs. To that end, various PEDOT:PSS-plasticizing approaches have been explored. These include the incorporation of plasticizing chemicals such as ionic liquids[41,63,66,67,174],

small organic molecules[40,42] and insulating organic polymers[42,69–71]. Recently, we reported employing poly(vinyl alcohol) (PVA) substrates infused with a diffusion-active organic plasticizer to achieve stretchability and conductivity within PEDOT:PSS[240] (**Chapter 4**).

Research on stretchable OECTs extends beyond material selection to encompass innovative device designs and architectures. Various strategies have been explored, including modifications to interconnects, such as wavy structures[173,175] and intentional microcracks in metal electrodes to enhance stress distribution[106]. Additionally, tailoring the supporting substrate plays a crucial role, with approaches like 3D-patterned substrates[172–174] and pre-straining. In the latter, either the entire device[7,9] or only the supporting substrate is pre-strained to induce buckling in the organic semiconductor[8,173,186,189], improving its stretchability. However, buckling may compromise seamless contact between the device and the area of interest.
Combining material and engineering strategies has also been explored. For instance, Chen et al.[107] utilized a honeycomb-structured channel material alongside a pre-strained substrate, while Nguyen et al.[172] employed 3D-patterned substrates, leveraging pre-strain to induce buckling in the channel. Meanwhile, Dai et al.[157] introduced intrinsically stretchable vertical OECTs, allowing charge carriers to move vertically and bypass strain-induced cracks rather than propagating through them laterally. These examples underscore the importance of integrating morphological and engineering approaches to achieve truly stretchable OECTs.

Despite recent progress, a fundamental understanding of how device performance correlates with geometric and morphological changes under strain remains scarce. However, this understanding is crucial to establish design rules for next-generation stretchable OECTs. Mechanical strain is known to influence the morphology of organic polymeric semiconductors[63,105], which in turn affects both electronic and ionic charge transport—key factors in OECT functionality. Additionally, the device performance is strongly linked to its geometry[22,116], which is inevitably altered under strain. While the impact of geometrical changes in stretchable electronics have been pointed out before[4,58,106,107,174,188,190], they have yet to be systematically investigated in a stretchable OECT. To address the aforementioned fundamental gaps, we developed a simple, fully stretchable all-solid PEDOT:PSS-based OECT. This was achieved using a substrate made from a mix of biodegradable PVA infused with the plasticizer diglycerol, along with a solid state electrolyte compromising 1-ethyl-3-methylimidazoliumbis(trifluormethylsulfonyl)amide (EMIM:TFSI). To unravel how the morphological and geometrical changes under strain affect the OECT performance, we conduct a comprehensive set of electrical measurements, and the data was analyzed using the Bernards-Malliaras model. Our findings underscore that rational design is critical for ensuring optimal function in intrinsically stretchable OECTs. When carefully engineered, factors such as electrolyte resistance, turn-off voltage and strain-induced chain alignment in PEDOT:PSS can be optimized to enhance OECT performance under strain.

5.3 Results

Intrinsically Stretchable OECTs

PEDOT:PSS-based OECTs operate in depletion mode, i.e. the device is in the 'ON' state by default. When a positive bias voltage is applied to the gate, cations from the electrolyte are pushed into the channel and compensate the negatively charged PSS^-. This in turn leads to a de-doping of $PEDOT^+$ and thus to the switching off of the device[18,20]. The intrinsically stretchable OECTs designed for this study consist of a stretchable substrate onto which two equally-sized PEDOT:PSS squares were transfer-printed[211] (**Fig. 5.1a**; methodology: **Chapter 3**). The fabrication process is shown in **Fig. S5.1** and the

chemical structures of the used materials in **Fig. S5.2**. For the stretchable substrate, we use biodegradable PVA infused with diglycerol as a plasticizer; an approach we introduced previously[211] (**Chapter 3**). Within a previous study that utilized glycerol instead of diglycerol, glycerol was found to diffuse from the substrate into the conducting layer and modify the PEDOT and PSS arrangement. This reorganization led to better-connected PEDOT-domains, resulting in an increased conductivity. Furthermore, the system showed an improved adaptability to strain[240] (**Chapter 4**). Discovering that the chemically similar plasticizer diglycerol has a higher ability to increase the PEDOT conductivity or, conversely, to reduce the sheet resistance (R_S; see **Fig. S5.3**: saturation after approx. 10 h), we employ it for our stretchable OECTs. As a solid state electrolyte, EMIM:TFSI is embedded in a poly(vinylidene fluoride-*co*-hexafluoropropylene) (PVDF-HFP) matrix. The electrolyte is cut using a custom-built stencil with precise margins to ensure reproducibility. Since the (de)doping of PEDOT:PSS film occurs in the region covered by the electrolyte (see the electrochromic effect in **Fig. 5.1b**), the dimensions of the channel and the gate (width and length) defined by the electrolyte, are visible in **Fig. 5.1b**. The functionality of the OECTs is demonstrated in **Fig. 5.1c** and **d**, where the transfer and output characteristics of a stretchable but unstrained OECT are shown. The first derivative of the transfer curves is determined to obtain the transconductance (g_m), which represents the ability of an OECT to translate an ionic signal into an electrical one (**Fig. 5.1c**, green curve). In agreement with literature-reports on stretchable OECTs based on PEDOT:PSS, the peak transconductance ($g_{m,max}$) of the devices is approx. 1.2 mS, peaking around V_{GS} = 0 V[90,97,174,186,189].

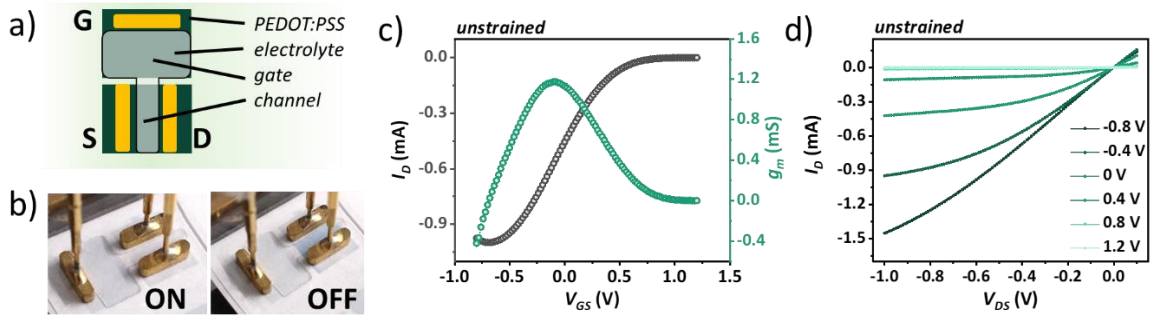

***Figure 5.1**: **a)** 2D representation of the OECT architecture: transfer-printed PEDOT:PSS, solid state electrolyte as well as configuration of source (S), drain (D) and gate (G). **b)** Photographs of the fully stretchable OECTs when switched on and off. **c)** Transfer curve and transconductance (at V_{DS} = -0.8 V) and **d)** output curves of a fully stretchable OECT at 0 % strain.*

Once the full functionality of the OECTs is confirmed, we investigate them under strain. To investigate possible anisotropy, two different OECT configurations are studied: parallel and perpendicular, which refers to the orientation of the strain relative to the direction of the channel and hence the electrical current (indicated in **Fig. 5.2a** and **b**). To ensure reproducibility, the electrolyte is removed while straining and attached to the strained devices. The devices are strained to 80 % strain in total in 20 % increments. We did not strain further since at 90 % strain cracks started to emerge (**Fig. 5.2c**). Besides that, unlike in other studies[7–9,173,186,189] there is no pre-strain applied to the substrates or devices. For each strain increment, three devices were tested. Sets of transfer curves for both the parallel and perpendicular OECTs are presented in **Fig. 5.2d** and **e**, with the remaining transfer and output curves available in **Fig. S5.4** - **S5.7**. Throughout this study, data recorded for the parallel configuration is shown in blue, while data for the perpendicular configuration is shown in red. We would also like to point out that all the data shown below originates from the same set of OECTs. **Fig. 5.2d** shows that with strain the on current (I_{ON}) remains nearly unchanged in the parallel devices (see also **Fig. S5.8**). However, the

saturation drain voltage slightly decreases and the slope of the linear regime slightly increases. Combined, these changes lead to an increase in $g_{m,max}$ with strain. In contrast, the perpendicular configuration shows the opposite behavior, which results in a lower $g_{m,max}$ upon strain. Plotting $g_{m,max}$ as a function of strain (**Fig. 5.2f**) confirms these visual observations. In the parallel configuration, $g_{m,max}$ increases by roughly 26 %, rising from 1.2 ± 0.1 mS to 1.51 ± 0.2 mS at 60 % strain on average. Beyond this point, $g_{m,max}$ decreases slightly but still is well above the initial value at 0 % strain. In contrast, the perpendicular configuration experiences a dramatic 84 % loss in performance, with $g_{m,max}$ decreasing from 1.22 ± 0.08 mS to 0.4 ± 0.2 mS at 80 % strain. In summary, the parallel OECTs show improved performance under strain even without the use of techniques such as pre-straining, which are typically applied.

According to the Bernards and Maillaras[133] model (B-M-model), the drain current (I_D; **Eq. S5.1**) depends on the device geometry (width (*W*), length (*L*) and thickness (*t*)), as well as on intrinsic material parameters like the mobility (μ) and volumetric capacitance (C^*). Therefore, the transfer characteristics are a reflection of any changes in these parameters[18,22,53,118]. To better understand how strain affects these parameters and, in turn, the electrical behavior of our OECTs, we will examine them more closely in the next two sections.

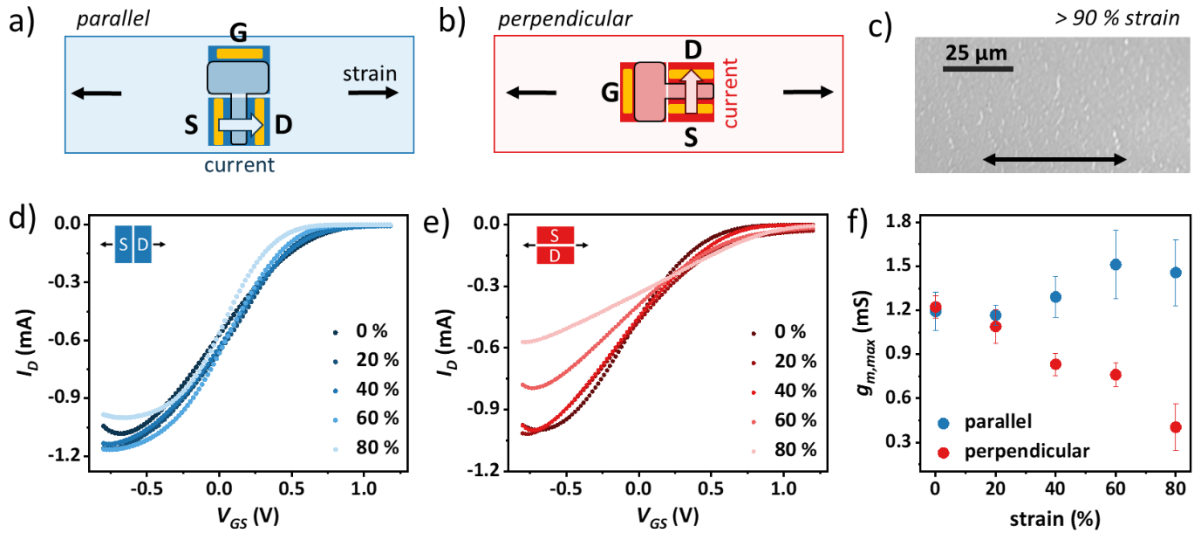

***Figure 5.2**: **a)** and **b)** Schematic of OECT configurations aligned parallel and perpendicular to the direction of strain, with strain and current direction indicated (dimensions are not to scale). **c)** Cracks emerging at > 90 % strain. **d)** and **e)** transfer curves (drain current) of stretchable OECTs for parallel and perpendicular configuration at 0, 20, 40, 60 and 80 % strain. **f)** Peak transconductance $g_{m,max}$ with strain.*

Strain-Induced Geometrical Changes

The OECT dimensions discussed herein are depicted and indicated in **Fig. 5.3a**, **S5.9** and **S5.10**. First, it is important to keep in mind that the channel length (*L*, indicated in **Fig. 5.3a**) remains constant during straining as it is defined by the electrolyte, which is attached on top of the strained devices and removed while straining (see also **Fig. 5.1a** and **S5.1**). Another important geometrical factor to consider within OECTs is the thickness (*t*) of the organic semiconductor[18,118]. Typically, the thickness for a uniform thin film is expected to decrease during stretching[105–107]. Using scanning force microscopy (SFM) in PeakForce mode, we examine the PEDOT:PSS film thickness at various strains (**Fig. 5.3b**, **S5.11** - **S5.13** and **Tab. S5.1**). Surprisingly, we observe no change in film thickness up to 80 % strain. Summarizing, the channel length and PEDOT:PSS thickness (of both gate and channel) remain constant

during stretching. Moving forward, the distance between the channel and gate ($d_{ch\text{-}g}$) and the channel width (W, both indicated in **Fig. 5.3a**) are investigated in detail. The distance between gate and channel ($d_{ch\text{-}g}$) becomes relevant when looking at the electrolyte resistance (R_{el}) which has been reported to increase with increasing distance and vice versa[142]. Within the parallel configuration, $d_{ch\text{-}g}$ shrinks upon strain by roughly 20 %, while it increases in the perpendicular configuration by approx. 82 % (**Fig. 5.3d**, left). To verify effects arising from the change in $d_{ch\text{-}g}$, we perform impedance spectroscopy (IS) on the strained OECTs. The data analysis is performed assuming the equivalent circuit illustrated in **Fig. S5.14**. R_{el} was extracted at high frequencies, where the phase angle approaches 0° (**Fig. S5.15** and **S5.16**). In this region, the impedance of the capacitors becomes negligible, effectively behaving as a short circuit. **Fig. 5.3d**, right, shows that R_{el} decreases upon strain in the parallel configuration (by approx. 21 %), whereas it increases significantly in the perpendicular configuration (~ 100 %). The magnitude of these findings align with the change in $d_{ch\text{-}g}$.

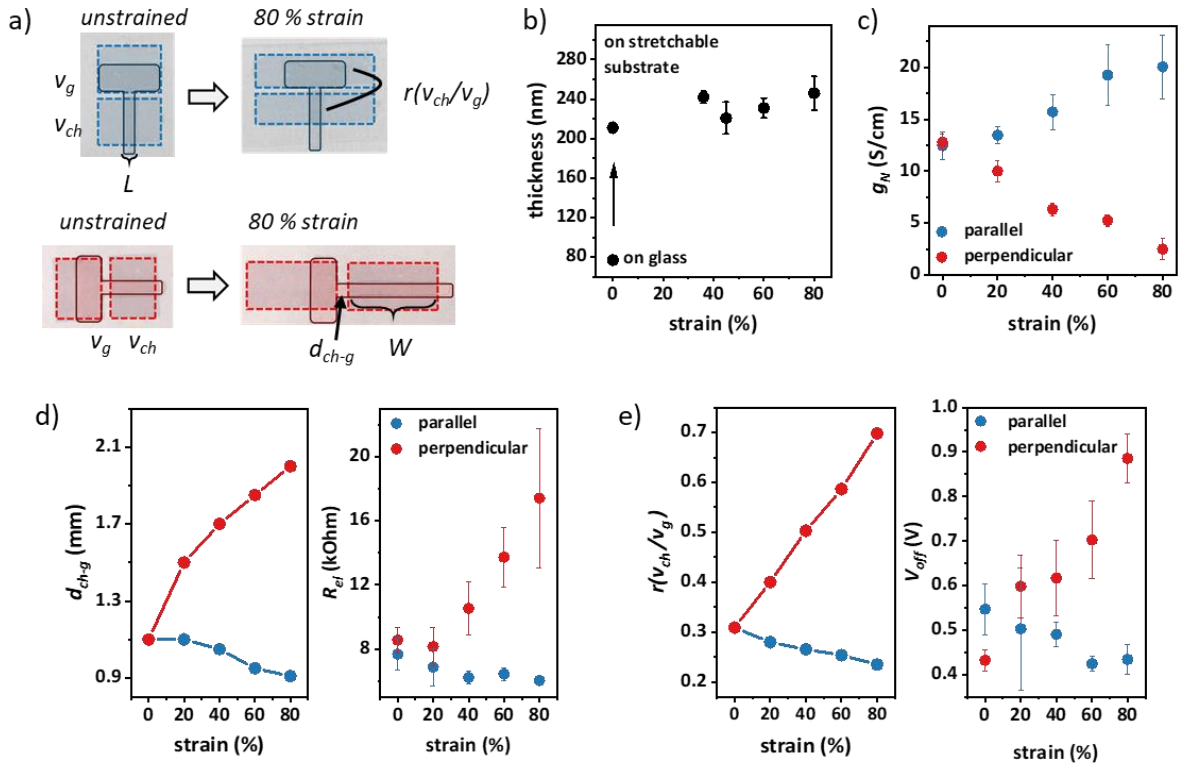

***Figure 5.3**: **a)** Photographs of the parallel and perpendicular OECTs at 0 % and 80 % strain. The gate volume (v_g), channel volume (v_{ch}), ratio between the gate volume and channel volume ($r(v_{ch}/v_g)$) and distance between the gate and the channel ($d_{ch\text{-}g}$) are indicated. **b)** Film thickness on glass and after transfer-printing at various strains. **c)** Normalized transconductance (g_N) against strain. **d)** Left: change in distance between gate and channel ($d_{ch\text{-}g}$) and right: electrolyte resistance (R_{el}) against strain. **e)** Left: ratio between volume of the channel and the gate ($r(v_{ch}/v_g)$) and right: turn-off voltage (V_{off}) against strain.*

The channel width (W) shows opposite trends depending on the configuration: it decreases with a parallel configuration and increases with a vertical configuration (**Fig. 5.3a**, **S5.17**). An important effect of the change in channel width lies in the overall capacitance of the channel. Organic mixed conductors such as PEDOT:PSS are known to have a volumetric capacitance, which means that changes in channel geometry also affect their capacitance. The same applies to the gate electrode, which also consists of PEDOT:PSS. According to the findings of Koutsouras et al.[159], the ratio between the channel and gate capacitance determines the portion of applied gate voltage that effectively drops at the

electrolyte/channel interface. This voltage is relevant for the OECT performance, as it influences the drain current modulation efficiency; for example, a higher voltage at the electrolyte/channel interface results in a steeper transfer curve, which in turn decreases the saturation drain voltage[159]. Since in this work, both channel and gate consist of PEDOT:PSS, the ratio of the capacitances can be defined as the ratio of the volume ($r(v_{ch}/v_g)$, **Fig. 5.3e**, left). Analogously to the width, $r(v_{ch}/v_g)$ decreases in the parallel and increases in the perpendicular configuration. In other words, in the parallel configuration the volume of the channel shrinks relative to the volume of the gate, while in the perpendicular, this trend is reversed (see also **Fig. S5.9**, **S5.10**). To study the impact of these changes, we can calculate the turn-off voltage (V_{off}), which is the gate voltage required to reduce the drain current to zero (**Eq. S5.4**)[11,137]. **Fig. 5.3e** (right) shows that in the parallel configuration, V_{off} decreases with strain as $r(v_{ch}/v_g)$ decreases, indicating a higher voltage at the electrolyte/channel interface. Conversely, the perpendicular configuration exhibits the opposite behavior. Again, the magnitude of the change in V_{off} aligns well with the magnitude of the geometrical change.

As $g_m = -(W \cdot t)/L \cdot \mu \cdot C^* \cdot V_D$ depends on geometric factors, the transconduction-strain relationship ($g_{m,max}$ vs strain) in **Fig. 5.2f** is a direct reflection of the above-discussed changes. To isolate material changes from geometric contributions, we calculate the normalized transconductance g_N ($= g_m(L/(W \cdot t))$ and plot it against the strain in **Fig. 5.3c**. At 0 % strain, both configurations show a g_N of approx. 13 S/cm. Under strain, the normalized transconductance significantly increases by 51 % (20 ± 3 S/cm) in the parallel configuration at 80 % strain. In contrast, in the perpendicular configuration, it decreases by approx. 80 %, plummeting to 3 ± 1 S/cm at full strain. By factoring out the geometric influence, it becomes clear that the strain-induced morphological changes in PEDOT:PSS significantly contribute to the OECT performance. This, in turn, ought to be reflected in the μC^*-product[118] (**Eq. S5.5**) which takes into account the electronic mobility (μ) and volumetric capacitance (C^*) of an organic semiconductor. Naturally, they are heavily influenced by the organic semiconductor's morphology and, therefore, will be discussed next.

Strain-Induced Morphological Changes

The μC^*-product is extracted by fitting the OECT transfer curves as proposed in [133] and taking into consideration the above-discussed geometrical changes (see **Fig. S5.4**, **S5.5** and SI: *Electrical circuit*). **Fig. 5.4a** shows that both configurations exhibit an almost identical initial μC^*-product of approx. 15 F/(cm·V·s) at 0 % strain. With increasing strain, the configurations show opposing trends, with the μC^*-product increasing to 23 ± 3 F/(cm·V·s) (+53 %) in the parallel and decreasing to 3 ± 1 F/(cm·V·s) (-80 %) in the perpendicular configuration. The change in the μC^*-product corresponds well to the in/decrease in g_N (**Fig. 5.3c**) and thus shows the anticipated trend. The number of ions penetrating the channel (volumetric capacitance (C^*)) is determined using chronoamperometry. Please, see SI: *chronoamperometry* for a detailed description of the data analysis (**Fig S5.18** and **S5.19**, **Eq. S5.6** - **S5.11** and **Tab. S5.2**). The obtained values for C^* against the strain are depicted in **Fig. 5.4b**. First, it is important to mention that the values obtained for C^* (approx. 22 F/cm³, before strain) are within the range of literature values[138,241]. Independently of the OECT configuration, a decrease in C^* is observed, indicating that upon stretching less ions are penetrating the channel. At 80 % strain both configurations show a C^* of approx. 13 F/cm^3, loosing almost half their initial volumetric capacitance. Since C^* is a property inherent to the material[242] and the uptake of ions happens in the out-of-plane direction, it stands to reason that the trend with elongation is the same for both configurations. From the μC^*-product and C^* we are able to determine the hole carrier mobility (μ) of PEDOT:PSS within our stretchable OECTs (**Fig. 5.4c**). The hole mobility is approx. 0.7 cm^2/(Vs) prior to stretching, in agreement with literature[51,118,243]. Upon stretching, a clear anisotropy becomes apparent. In the parallel devices,

the hole mobility nearly triples (1.9 ± 0.3 cm^2/(Vs)) at 80 % strain. In the perpendicular devices, however, it decreases to 0.2 ± 0.1 cm^2/(Vs). And finally, from the electrolyte resistance (**Fig. 5.3d**, right) and the channel capacitance (C_{ch}) extracted from chronoamperometry (**Fig. S5.20**), we calculate the charge time of the stretchable OECTs (t_{charge}= R_{el}·C_{ch}). Again, both configurations show an identical initial value (approx. 0.65 s at 0 % strain; **Fig. 5.4d**). With strain, the charge time of the channel current to the gate voltage step decreases in the parallel OECT (0.21 ± 0.05 s), while it increases significantly in the perpendicular OECT (1.6 ± 0.4 s).

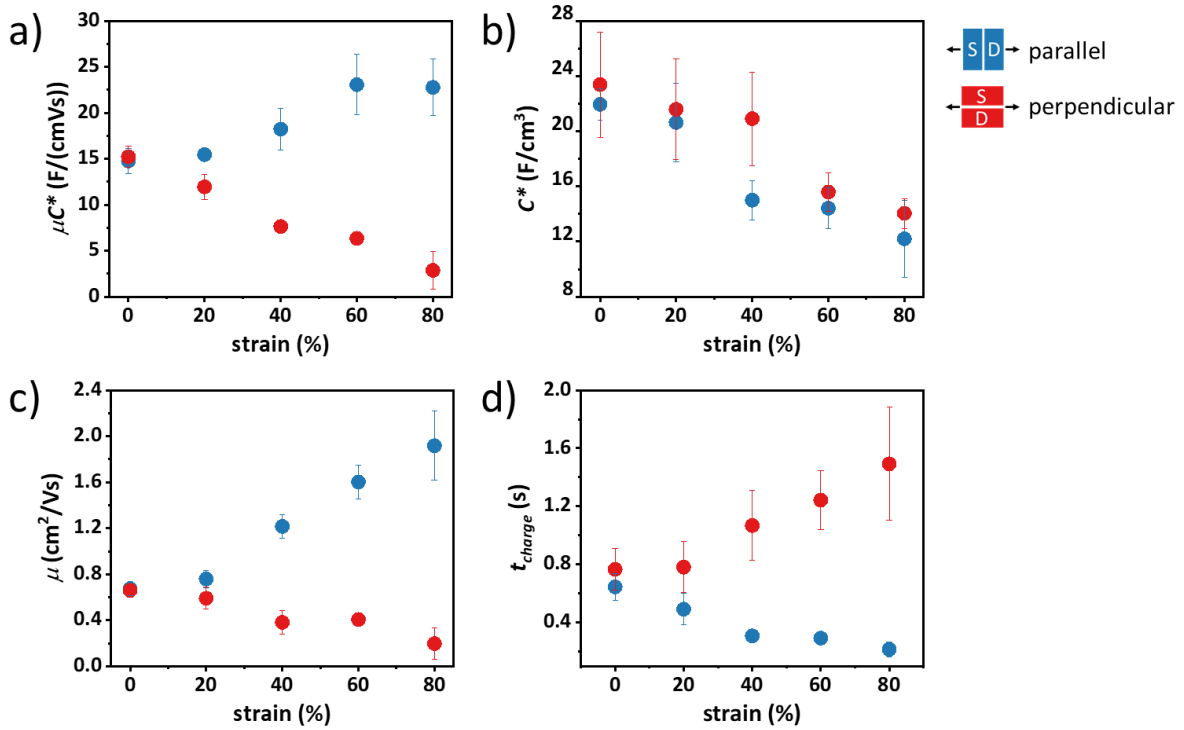

***Figure 5.4**: **a)** μC*-product, **b)** volumetric capacitance (C*), **c)** hole mobility (μ) and **d)** charge time (t_{charge}) upon strain for the parallel and perpendicular OECT configuration.*

5.4 Discussion

To advance next-generation stretchable OECTs, it is crucial to explore the fundamental relationships between device geometry, strain-induced morphological changes and performance. From these fundamental relationships, reliable OECT design principles can be derived. In our study, we compare two configurations for fully PEDOT:PSS-based stretchable OECTs: parallel, where the strain aligns with the current, and perpendicular, where strain is applied orthogonally (**Fig. 5.2a** and **b**). Importantly, the devices are tested without pre-strain, allowing for a fundamental analysis of morphological effects.

The impact of strain is immediately evident in the transfer curves: in the parallel configuration, the curves steepen, resulting in a lower turn-off voltage and higher transconductance. In contrast, the perpendicular configuration causes the curves to flatten with strain, increasing the turn-off voltage and reducing transconductance (**Fig. 5.2d**, **5.2e**, **5.3e**). Based on these observations, the parallel configuration is adapting to strain better than the perpendicular one, which is confirmed by a 26 % increase in maximum transconductance (**Fig. 5.2f**). Since transfer curves and transconductance are influenced by both geometrical and morphological factors, we investigate the effects of strain on these

factors in detail (summarized in **Tab. 5.1**). Geometrically, strain can either enhance or impair device performance. We would like to point out that 'enhance' herein is defined as maintained or improved device performance. An unfavorable configuration can increase the turn-off voltage (**Fig. 5.3e**), partially negating the advantage of low operating voltages—a key feature of OECTs[20]. Additionally, if strain increases the distance between the gate and channel, the electrolyte resistance increases, which, together with the capacitance, affects the device's charge time (**Fig. 5.3d** and **5.4d**). In the perpendicular configuration, this charge time increases significantly, a critical consideration for applications requiring minimal strain-induced delays[22,146,147]. This result is unexpected, as transconductance and charge time typically exhibit an inverse relationship: increasing the channel volume to enhance transconductance generally leads to a slower response to an applied voltage[22,53]. In our study, however, the transconductance increases alongside a decreasing device charge time.

***Table 5.1**: Changes observed within the OECTs under strain and their effect on device parameter such as the (normalized) transconductance, μC*-product, the ratio between the gate and channel volume, the distance between gate and channel, volumetric capacitance and hole mobility in the parallel and perpendicular configuration.*

parameter	*effect of strain*	
	parallel	*perpendicular*
transconductance (g_m)	↑	↓
normalized transconductance (g_N)	↑	↓
μC^*-product	↑	↓
channel to gate volume ratio ($r(v_{ch}/v_g)$)	V_{off} ↓	V_{off} ↑
channel-gate distance ($d_{ch\text{-}gate}$)	R_{el} ↓	R_{el} ↑
chain-alignment: hole mobility	μ ↑ and I_{ON} =	μ ↓ and I_{ON} ↓
polymer packing: volumetric capacitance	C^*↓	C^*↓
charge time	t_{charge} ↓	t_{charge} ↑

To differentiate between geometrical and morphological contributions, we calculate the normalized transconductance (**Fig. 5.3c**), revealing a 51% performance increase in the parallel OECT at maximum strain. This underscores the critical role of morphological changes under strain. A similar trend is observed in the μC^*-product (**Fig. 5.4a**). By decoupling volumetric capacitance from hole mobility, we identify a strain-induced decrease in volumetric capacitance, independent of the OECT configuration. This, in turn, reveals anisotropy in hole mobility: in the parallel configuration, the mobility increases under strain, whereas in the perpendicular configuration, the mobility decreases (**Fig. 5.4b** and **c**). An increase in charge carrier mobility upon strain is typically associated with chain alignment and has been reported for organic polymeric conductors[105,244]. Moreover, in a previous study, we demonstrated this exact chain alignment in a similar PEDOT:PSS system[240] (**Chapter 4**). Additionally, an inverse relationship between volumetric capacitance and hole mobility has been reported for PEDOT:PSS: as the mobility increases, the volumetric capacitance decreases[51]. Concluding, we propose that in our OECTs, the polymeric chains in the channel undergo morphological rearrangement under strain, adopting a more compact structure. Along the strain direction, this leads to enhanced charge carrier mobility while simultaneously restricting the overall ion uptake. In the parallel OECTs, the increased hole mobility countervails the decrease in volumetric capacitance, ultimately enhancing overall performance under strain.

In summary, we demonstrate that the interplay between device geometry, strain-induced morphological changes and performance in OECTs becomes evident under strain, with each factor influencing the others. When designing next-generation stretchable OECTs, it is crucial to consider the impact of strain on the operational regime and charge time. Additionally, morphological changes—

which may either enhance or hinder charge transport and ion uptake—need careful examination to ensure a device that operates reliably under strain.

5.5 Supplementary Information

Experimental

Materials: PEDOT:PSS (Clevios PH1000, Hereaus Deutschland GmbH), diglycerol (isomers,), *iso*-propanol and acetone (honeywell riedel-de haën), PVA (M_w= 31000 – 50000 g/mol, 99 % hydrolyzed; Sigma Aldrich), EMIM:TSI, PVDF-HFP were used without any further purification.

Material analysis: *Optical Microscopy*: Microscopic images were recorded in bright field mode using a confocal microscope (Leica DM6000 M) and the according software (Leica Application Suite Version 4.12.0). The strained films were secured on glass slides using double-sided tape. *SFM measurements*: PeakForce-Quantitative Nanomechanical Mapping (PF-QNM) SFM measurements were performed using a Bruker Dimension ICON platform using OLTESPA NanoAndMore cantilevers (frequency: 70 KHz, spring constant: 2 N/m, back/ tip side coating: Al). The film thickness was determined using the NanoScope Analysis 1.9 software plane fit and section tool.

OECT fabrication: OECTs were prepared following the patterning and transfer-printing process described in [211] (**Chapter 3**) and depicted in **Fig. S5.1**. Briefly, glass slides were cleaned in an ultra-sonic bath (5 min in DI water, 10 min acetone and 10 min in IPA) and dried at 120 °C for 10 min. Prior to spin-coating PEDOT:PSS at 750 rpm for 60 s the glass slides were UV/ ozone-treated for 20 min. The resulting thin-films were hard-backed for 10 min at 120 °C, patterned attaching a custom-designed mask and using an oxygen plasma treatment and subsequently transfer-printed on PVA:diglycerol (65 wt%) substrates. All transfer-printed OECTs were allowed to rest for at least 48 h to ensure full saturation and PEDOT:PSS re-arrangement. The electrolyte gel was prepared by combining EMIM:TFSI, PVDF-HFP and acetone. Once fully mixed, the solution was drop-cast onto glass slides, dried and then cut into shape using in-house-built stencils. Finally, the OECT was placed in a self-built stretching station and the cut electrolyte was applied to the designated areas.

OECT analysis: OECT transfer curves were recorded using a Keithley 4200A-SCS. V_{GS} ranged from -0.8 V to 1.2 V, while V_{DS} was consistently set to -0.8 V. A hold time of 4 s and a delay time of 1 s were utilized, taking into consideration the slower movement of the electrolyte embedded in a solid-state matrix. The OECTs were stretched in both directions simultaneously to 80 % strain in total in 20 % increments (speed: 0.55 mm/s) and analyzed in stretched state. The electrolyte was removed for each straining step. In-house-built contact probes, contacting source, drain and gate, were applied onto the PEDOT:PSS. For chronoamperometry measurements (V_G = -0.5 V, t = 10 - 20 sec) and impedance spectroscopy were performed with a PalmSens 4 EIS potentiostat with connected source and drain contacts. Please see SI for a detailed description.

Fabrication Process and Materials

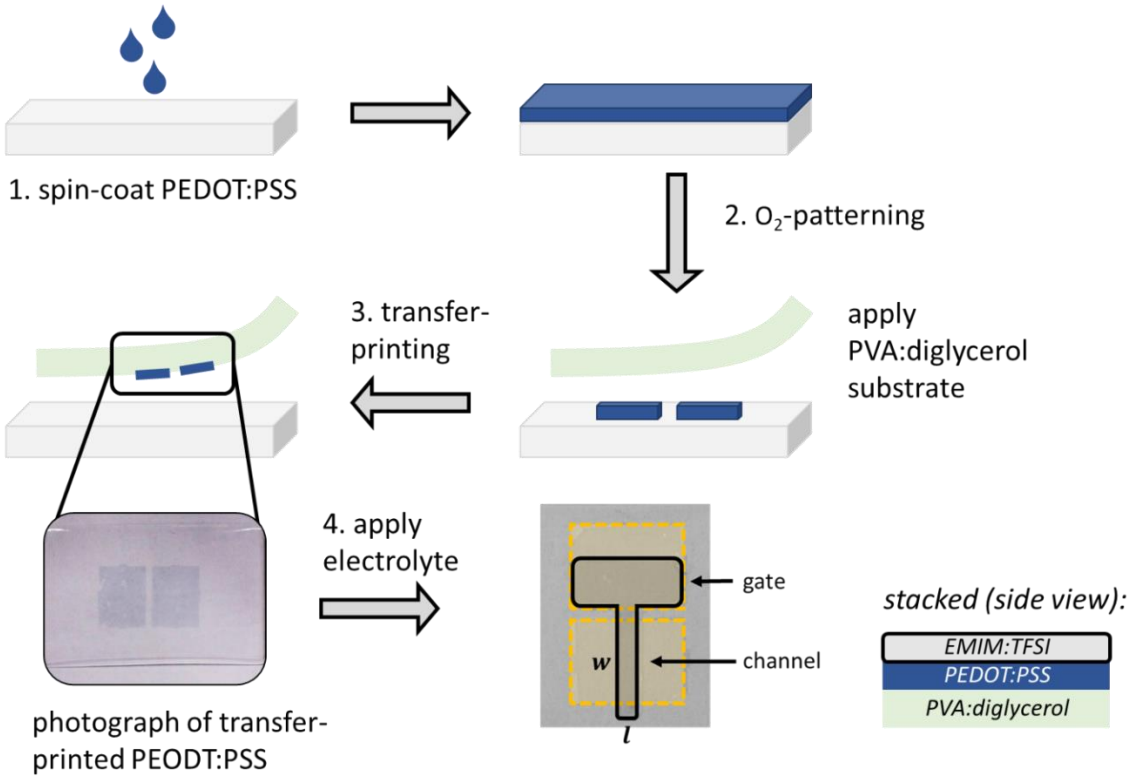

***Figure S5.1**: OECT fabrication process: Transfer-printing and patterning as described in detail in*[211] *(**Chapter 3**).*

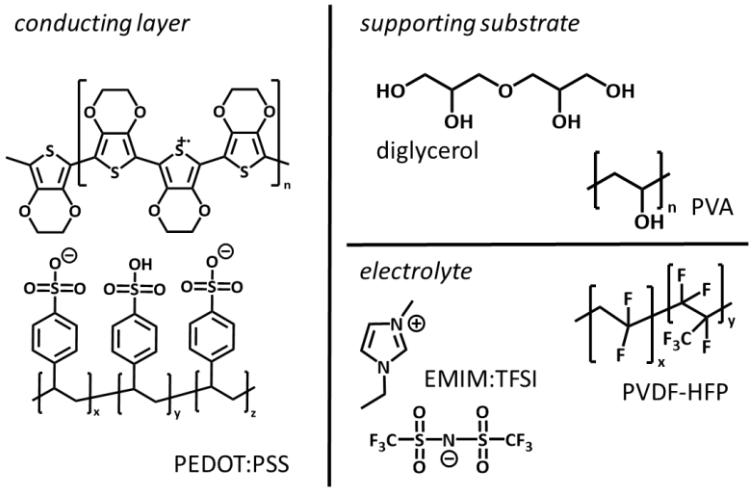

***Figure S5.2**: Chemical structures of: PEDOT:PSS (conducting layer), PVA:diglycerol (stretchable substrate) and EMIM:TFSI in PVDF-HFP (solid-state electrolyte).*

PEDOT:PSS Saturation with Diglycerol

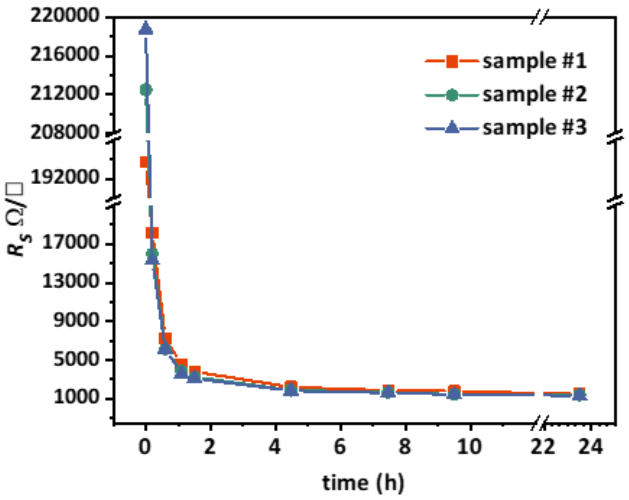

***Figure S5.3**: Sheet resistance of PEDOT:PSS against time after transfer-printing onto PVA:diglycerol substrates.*

OECT Characteristics

The same color coding of main text of **Chapter 5** (**5.3**) was applied: Blue indicates the parallel OECT arrangement, while red represents the perpendicular arrangement.

Transfer Curves

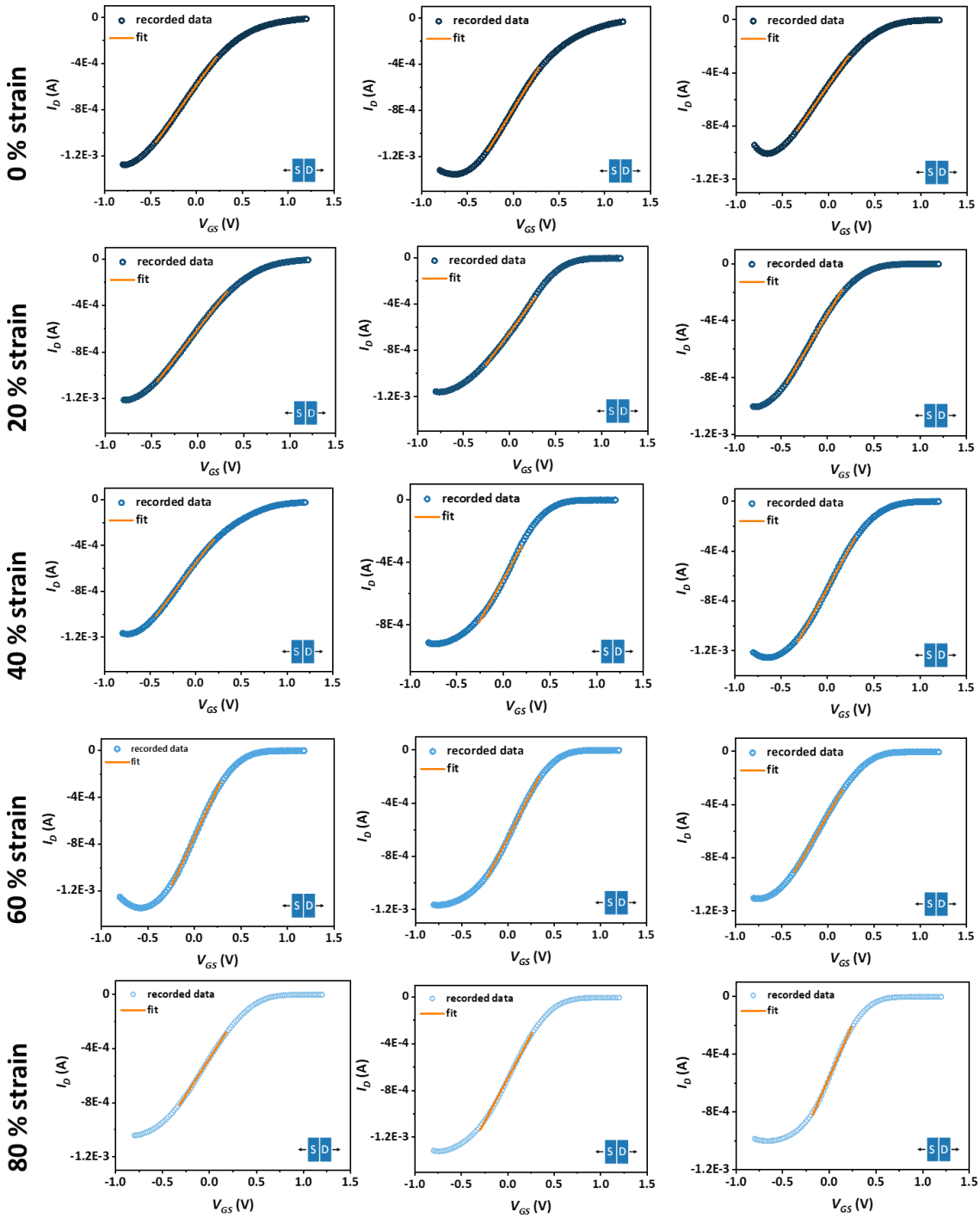

***Figure S5.4**: Transfer curves at V_{DS} = -0.8 V of the fully stretchable OECTs in parallel arrangement, including the fits performed using the Bernards and Malliaras model*[133] *(orange line).*

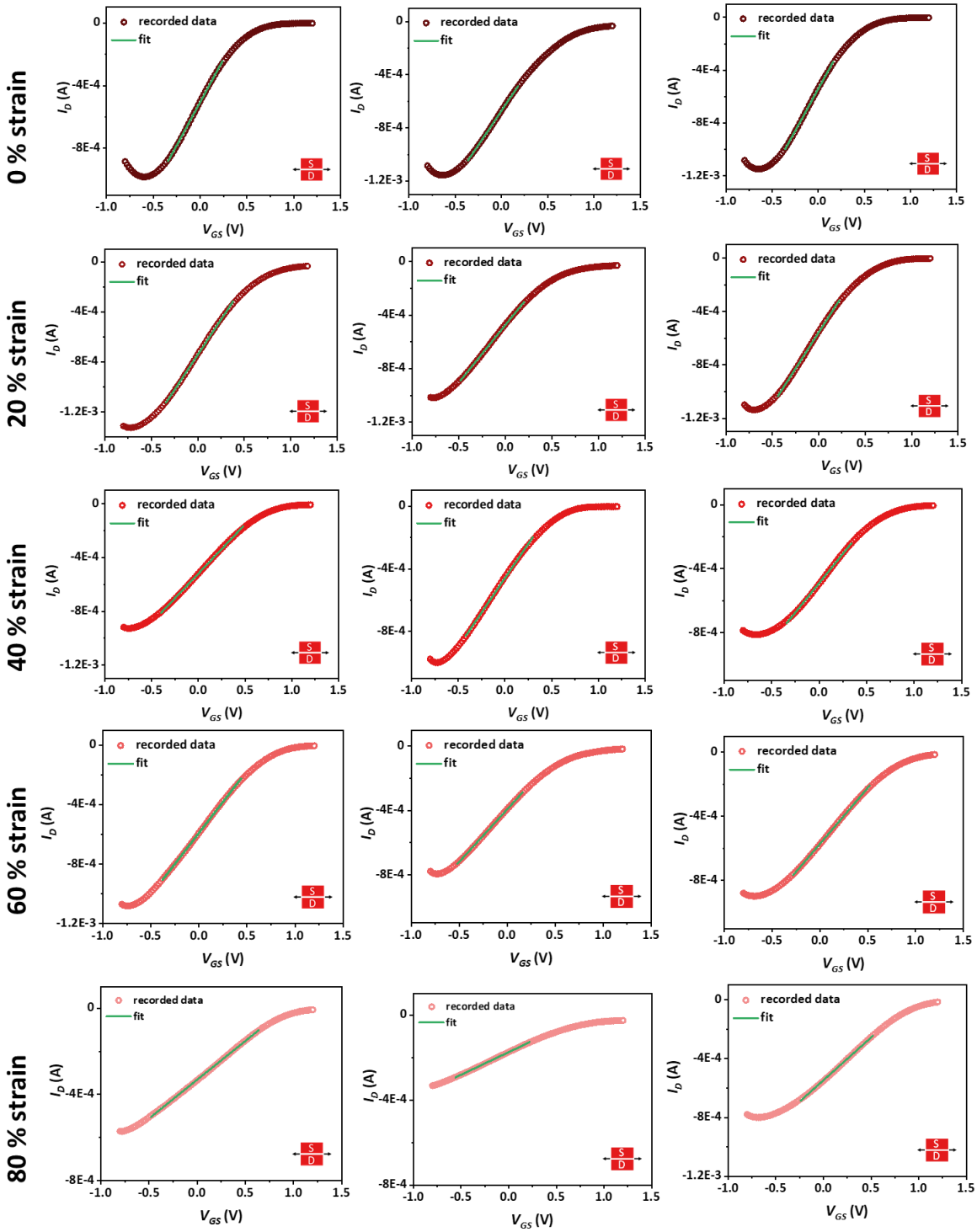

***Figure S5.5**: Transfer curves at V_{DS} = -0.8 V of the fully stretchable OECTs in perpendicular arrangement, including the fits performed using the Bernards and Malliaras model*[133] *(green line).*

Output Curves

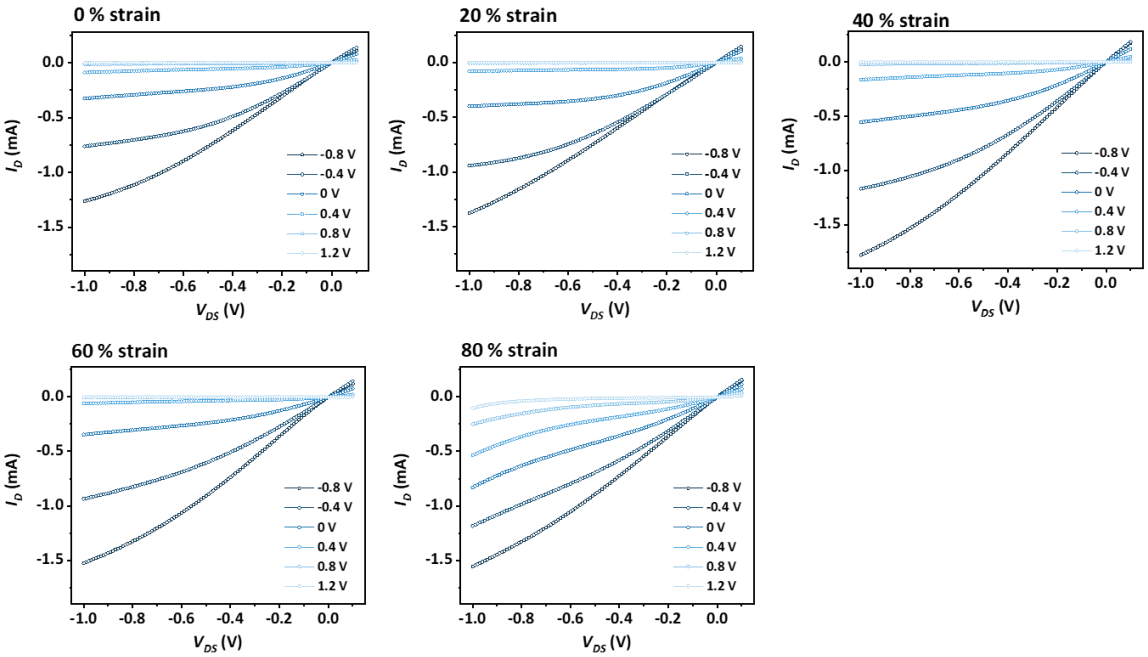

***Figure S5.6**: OECT output curves at V_{GS} = -0.8, -0.4, 0, 0.4, 0.8, 1.2 V of the fully stretchable OECTs in parallel arrangement at various strains.*

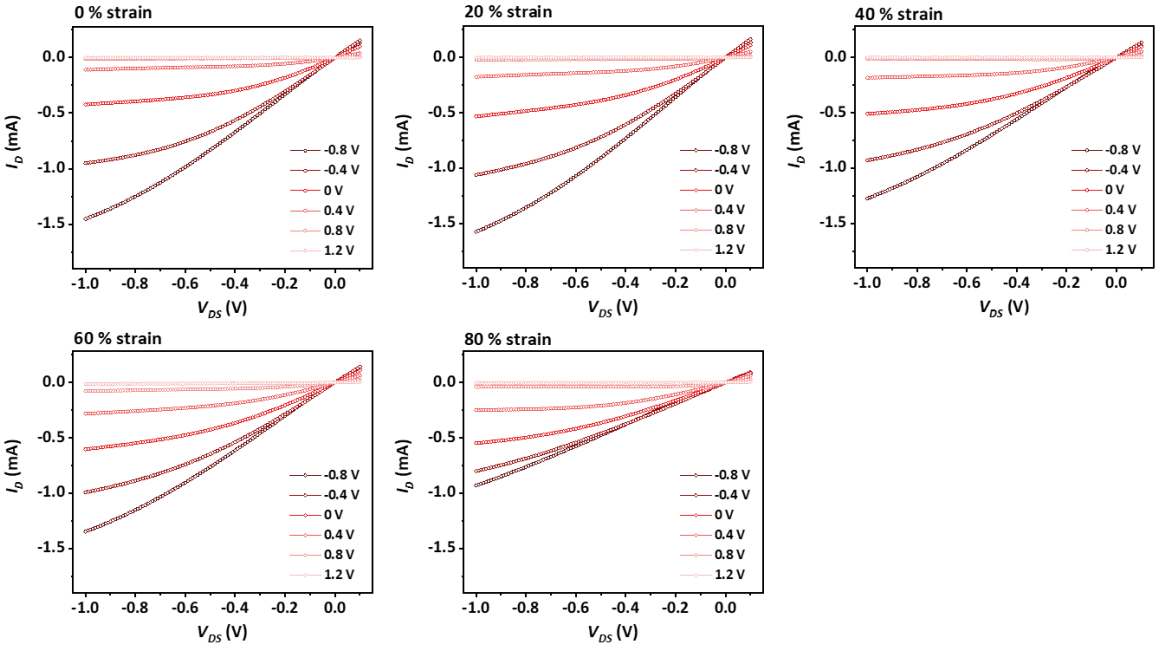

***Figure S5.7**: OECT output curves at V_{GS} = -0.8, -0.4, 0, 0.4, 0.8, 1.2 V of the fully stretchable OECTs in perpendicular arrangement at various strains.*

ON Current

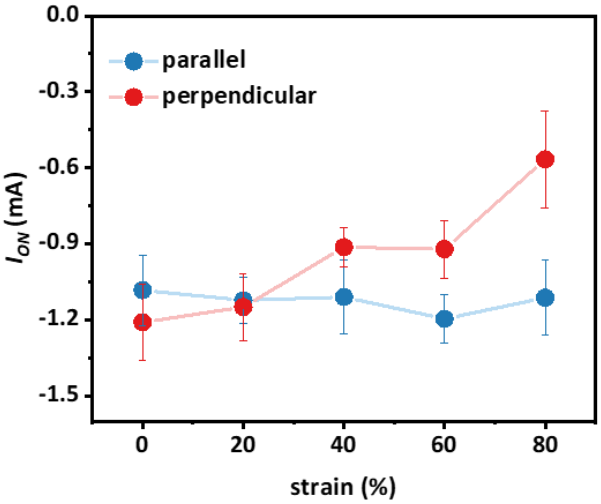

***Figure S5.8**: I_{ON} of parallel and perpendicular OECT arrangement against strain at V_{GS} = -0.8 V.*

Photographs of Stretched OECTs

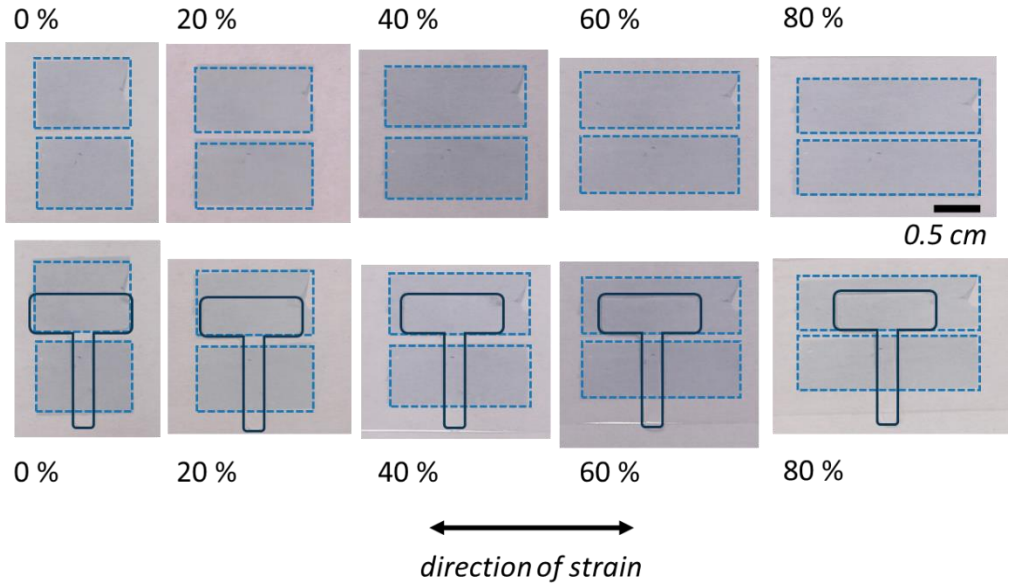

***Figure S5.9**: Straining OECTs parallel to the direction of strain. Top: Strained transfer-printed PEDOT:PSS only. Bottom: with applied electrolyte. Electrolyte and PEDOT:PSS are highlighted.*

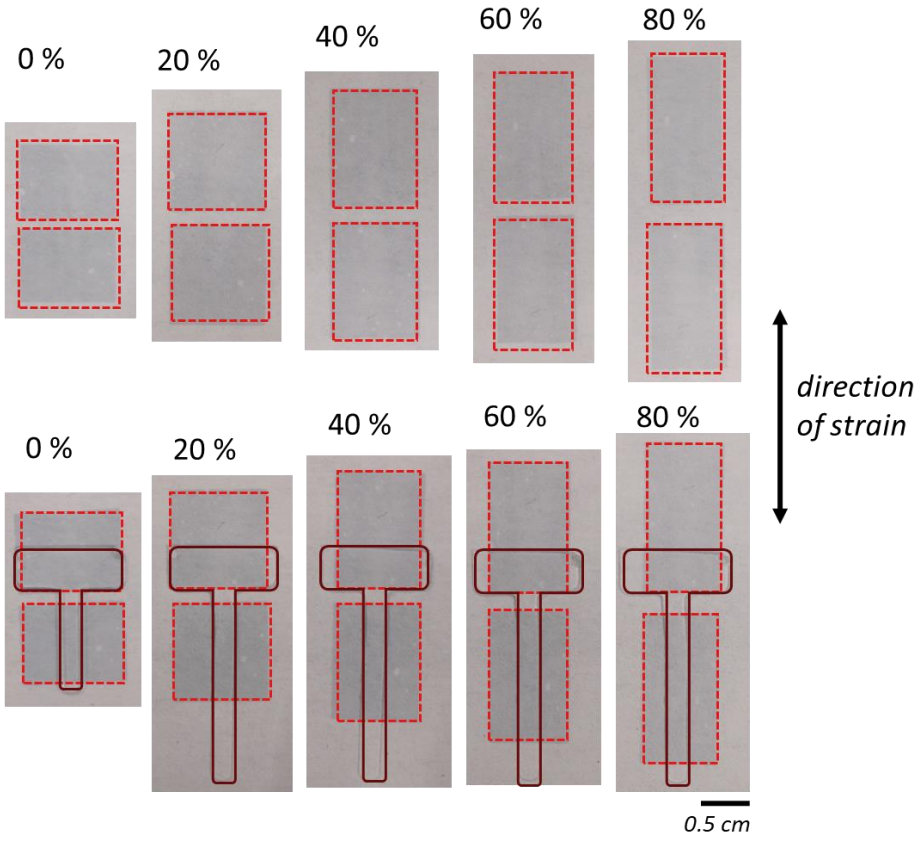

***Figure S5.10**: Straining OECTs perpendicular to the direction of strain. Top: Strained transfer-printed PEDOT:PSS only. Bottom: with applied electrolyte. Electrolyte and PEDOT:PSS are highlighted.*

Film Thickness under Strain

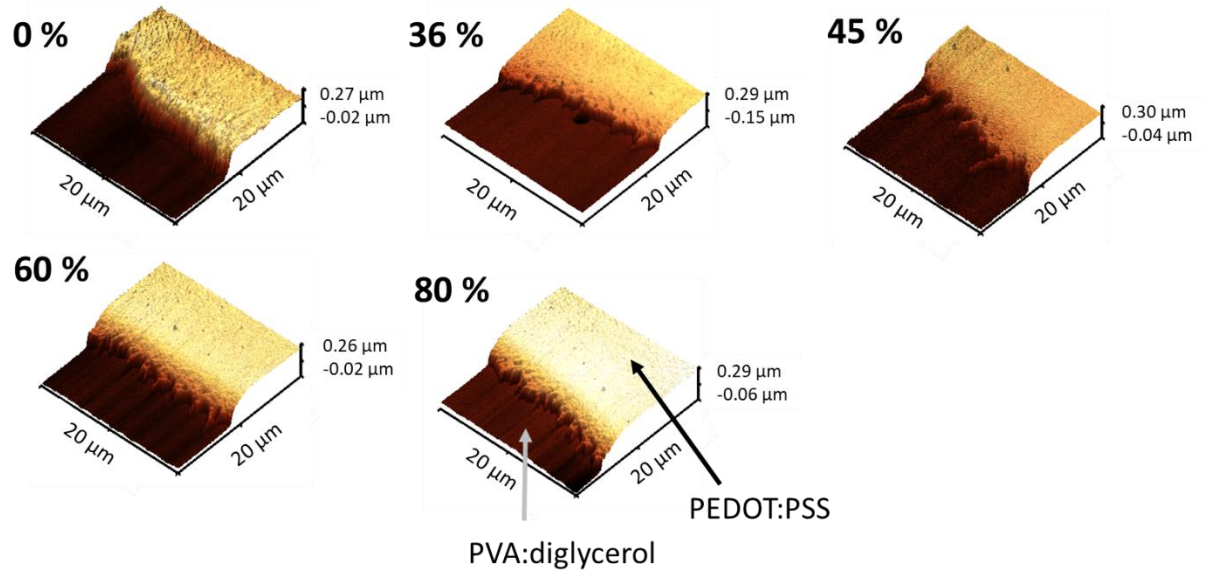

***Figure S5.11**: 3D scanning force microscopy (SFM)-topography images of transfer-printed PEDOT:PSS (bright orange) on PVA:diglycerol substrates (dark orange) at various strains.*

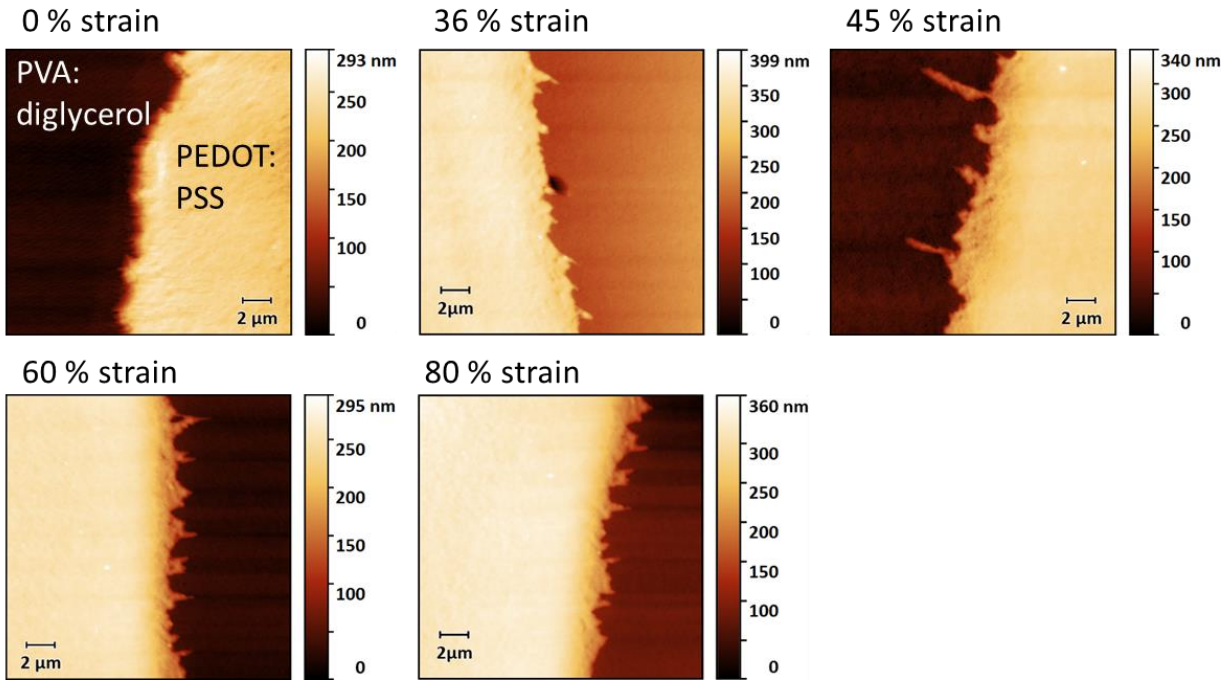

***Figure S5.12**: 2D scanning force microscopy (SFM)-topography images of transfer-printed PEDOT:PSS (bright orange) on PVA:diglycerol substrates (dark orange) at various strains.*

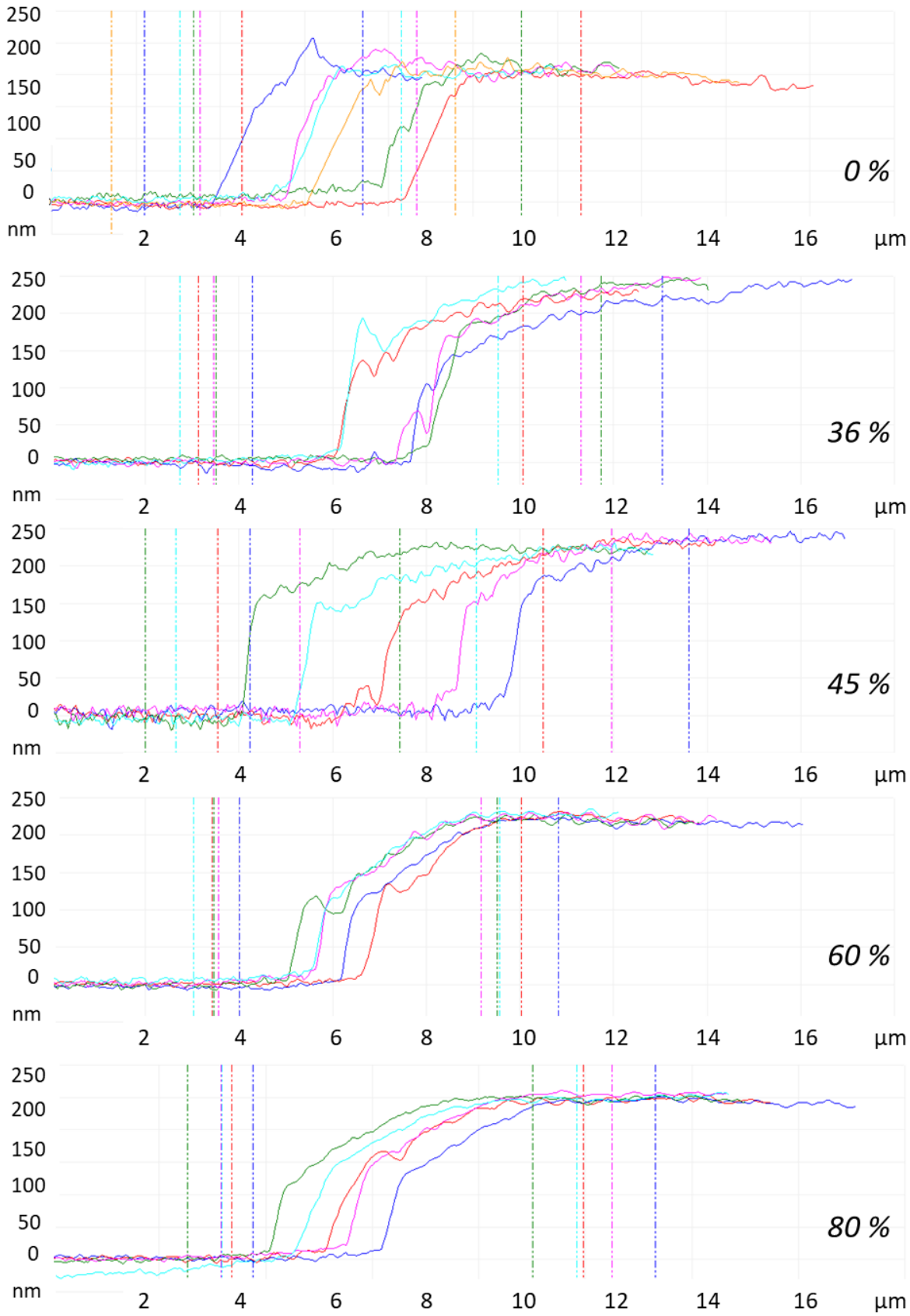

***Figure S5.13**: Cross-sections of **Fig. S5.12**. The thicknesses were determined by averaging the extracted values (see **Tab. S5.1**).*

Table S5.1: *Film thicknesses determined analyzing the cross-sections shown in* ***Fig. S5.12*** *and* ***S5.13****.*

strain (%)	**PEDOT:PSS thickness (nm)**
0	210 ± 10
36	220 ± 10
45	226 ± 4
60	226 ± 6
80	250 ± 60

Electrical Circuit

The Bernards-Malliaras (B-M) model describes the drain current (I_D) in depletion-mode OECTs for both steady and transient-state[133]. In this study, we will focus on the steady-state behavior. The model assumes that the device consists of two circuits: an electronic circuit and an ionic circuit. The electronic circuit represents the current between the drain and the source, which is modeled using Ohm's Law. The ionic circuit represents the current between the gate and the source. Applying this to our OECT architecture, the equivalent circuit depicted in **Fig. S5.14** was derived. Of the two capacitors, one represents the gate capacitance (C_g) and the other represents the channel capacitance (C_{ch}). A resistor positioned between these two capacitors accounts for the resistance imposed by the electrolyte (R_{el}). Both circuits are linked through the charge carrier density, which changes as ions accumulate in the channel.

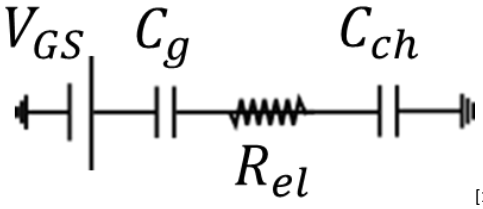

[133,142]

***Figure S5.14**: Equivalent circuit employed throughout this study: V_{GS}: gate voltage, C_g: gate capacitance, C_{ch}: channel capacitance, R_{el}: electrolyte resistance.*

The mathematical derivations are not presented here but can be found in detail in [132,133]. The final equation for the drain current I_D of the depletion-mode OECT is:

$$I_D = \begin{cases} \frac{G}{V_P}\left(V_P - V_{GS} + \frac{1}{2}V_{DS}\right)V_{DS}, & linear\ regime \\ \frac{G}{2V_P}(V_P - V_{GS})^2, & saturation\ regime \end{cases} \quad (S5.1)$$

with the conductance G, pinch-off voltage V_P, gate voltage V_{GS} and the drain voltage V_{DS}. G and V_P are defined as:

$$G = \frac{Wt}{L} q\mu\rho \quad (S5.2)$$

and

$$V_P = \frac{q\rho}{C_{eq}/_V} \quad (S5.3)$$

with the channel width W, channel thickness t, channel length L, elementary charge q, charge carrier mobility μ, initial charge carrier density p_0, equivalent capacitance C_{eq} and the volume V. For a detailed description of how C_{eq} was defined and experimentally determined, please refer to the chronoamperometry section. Using **Eq. S5.1**, we can calculate the voltage required to reduce the drain current to zero (V_{off}):

$$V_{off} = V_P + \frac{1}{2}V_{DS} \quad (S5.4)$$

with the drain-source voltage V_{DS}. And finally, from the first derivative of **Eq. S5.1** we can determine the transconductance g_m:

$$g_m = \frac{\partial I_D}{\partial V_{GS}} = \begin{cases} -\frac{Wt}{L}\mu C^* V_{DS}, & linear\ regime \\ \frac{Wt}{L}\mu C^* (V_P - V_{GS}), & saturation\ regime \end{cases} \quad (S5.5)$$

We fitted the experimental transfer curves to the B-M model, focusing on the linear regime, using Origin 2022 software. From the fitting results, we obtained the values for G and V_P. Using these values, along with the channel dimensions, we then calculated the μC^*-product (**Eq. 1.8**).

Impedance Spectroscopy

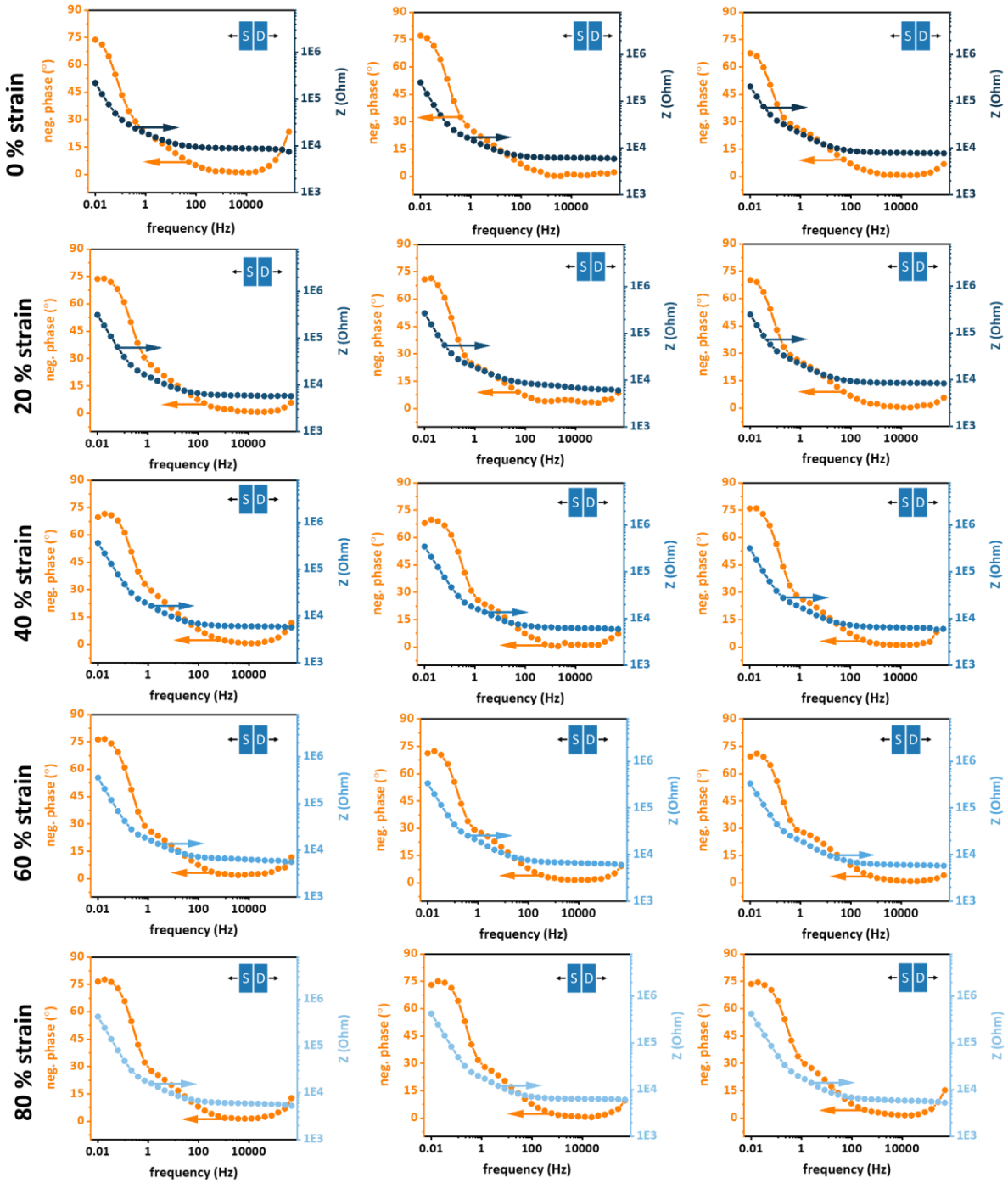

***Figure S5.15**: Impedance spectroscopy: Bode plot for the parallel OECT arrangement at different strains.*

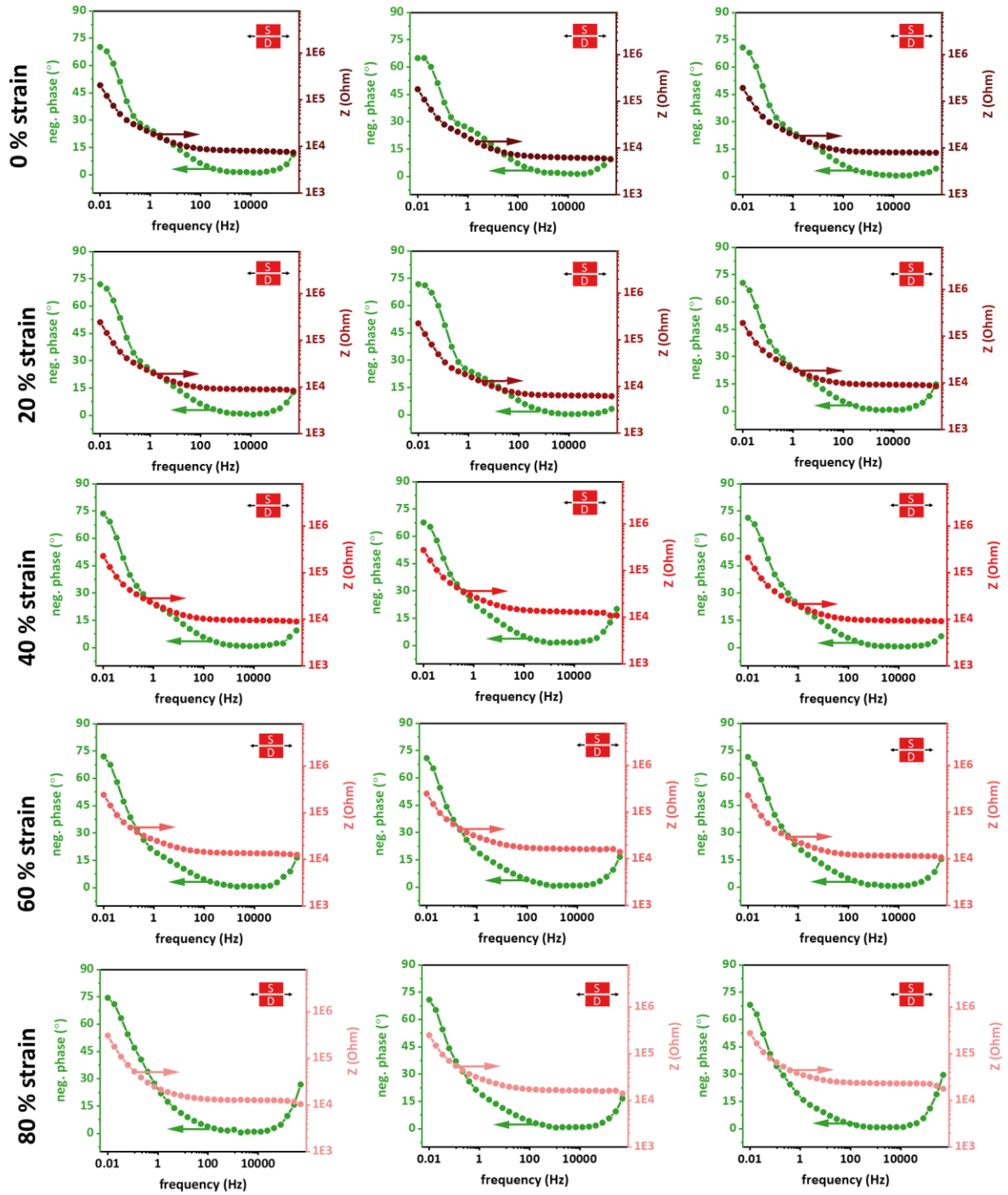

***Figure S5.16**: Impedance spectroscopy: Bode plot for the perpendicular OECT arrangement at different strains.*

Geometrical Changes

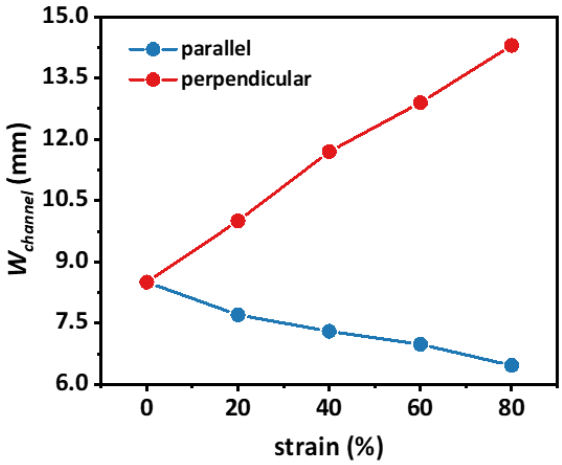

***Figure S5.17**: Change in channel width $W_{channel}$ upon strain for the parallel and perpendicular OECT arrangement.*

***Table S5.2**: Ratio between gate and channel volume (H(v(gate)/v(channel))), gate volume (v(gate)) and channel volume (v(channel)) for the parallel and perpendicular arrangement with strain.*

	parallel			perpendicular		
strain	*H(v(gate)/v(channel))*	*v(gate)*	*v(channel)*	*H(v(gate)/v(channel))*	*v(gate)*	*v(channel)*
%		cm^3 ($x10^{-5}$)	cm^3 ($x10^{-6}$)		cm^3 ($x10^{-5}$)	cm^3 ($x10^{-6}$)
0	3.23	1.2375	3.825	3.23	1.2375	3.825
20	3.57	1.2375	3.465	2.50	1.125	4.5
40	3.77	1.2375	3.285	1.99	1.046	5.27
60	3.94	1.2375	3.141	1.71	0.99	5.81
80	4.26	1.2375	2.907	1.43	0.821	6.435

Chronoamperometry

To determine the (volumetric) capacitance of the PEDOT:PSS films (under strain), we employed chronoamperometry. This technique includes applying a fixed potential at the gate electrode and recording the current as a function of time. By integrating the gate current I_G over time, we can determine the ionic charge Q accumulated within the gate and the channel:

$$Q = \int I_G dt \qquad (S5.6)$$

Q can also be expressed as the product of the applied gate voltage V_{app} and the equivalent capacitance C_{eq} of the circuit depicted in **Fig S5.13**:

$$Q = V_{app} C_{eq} \qquad (S5.7)$$

To determine C_{eq}, the ratio between gate and channel capacitance (C_g, C_{ch}, $H\left(\frac{v(gate)}{v(channel)}\right)$) is taken into account. Since channel and gate are made of the same material, their relation can be expressed using this ratio as a proportionality factor:

$$C_g = H\left(\frac{v(gate)}{v(channel)}\right) C_{ch} \qquad (S5.8)$$

For simplicity reasons $H\left(\frac{v(gate)}{v(channel)}\right)$ is re-written as:

$$H\left(\frac{v(gate)}{v(channel)}\right) \equiv x \qquad (S5.9)$$

Please see **Table S5.1** for x for both arrangements at 0 - 80 % strain.
The equivalent capacitance, taking in consideration **Eq. S5.8** and **S5.9**, can be expressed as:

$$C_{eq} = \frac{C_{ch} \cdot xC_{ch}}{C_{ch} + xC_{ch}} = \left(\frac{x}{1+x}\right) C_{ch} \qquad (S5.10)$$

Inserting this into **Eq. S5.7** and rearranging gives:

$$C_{ch} = \frac{Q}{V_{app}}\left(\frac{1+x}{x}\right) \qquad (S5.11)$$

In combination with the values listed in **Tab. S5.1**, **Eq. S5.11** was used to determine the channel capacitance (**Fig. S5.20**) as well as the volumetric capacitance of the channel. For this, the data shown in **Fig. S5.18** and **S5.19** was analyzed. To calculate the charge time, the capacitance was multiplied by the electrolyte resistance ($t_{charge} = R_{el} \cdot C_{ch}$; **Fig. 5.3d**, **S5.15** and **S5.16**). The error was determined employing a Gaussian error distribution.

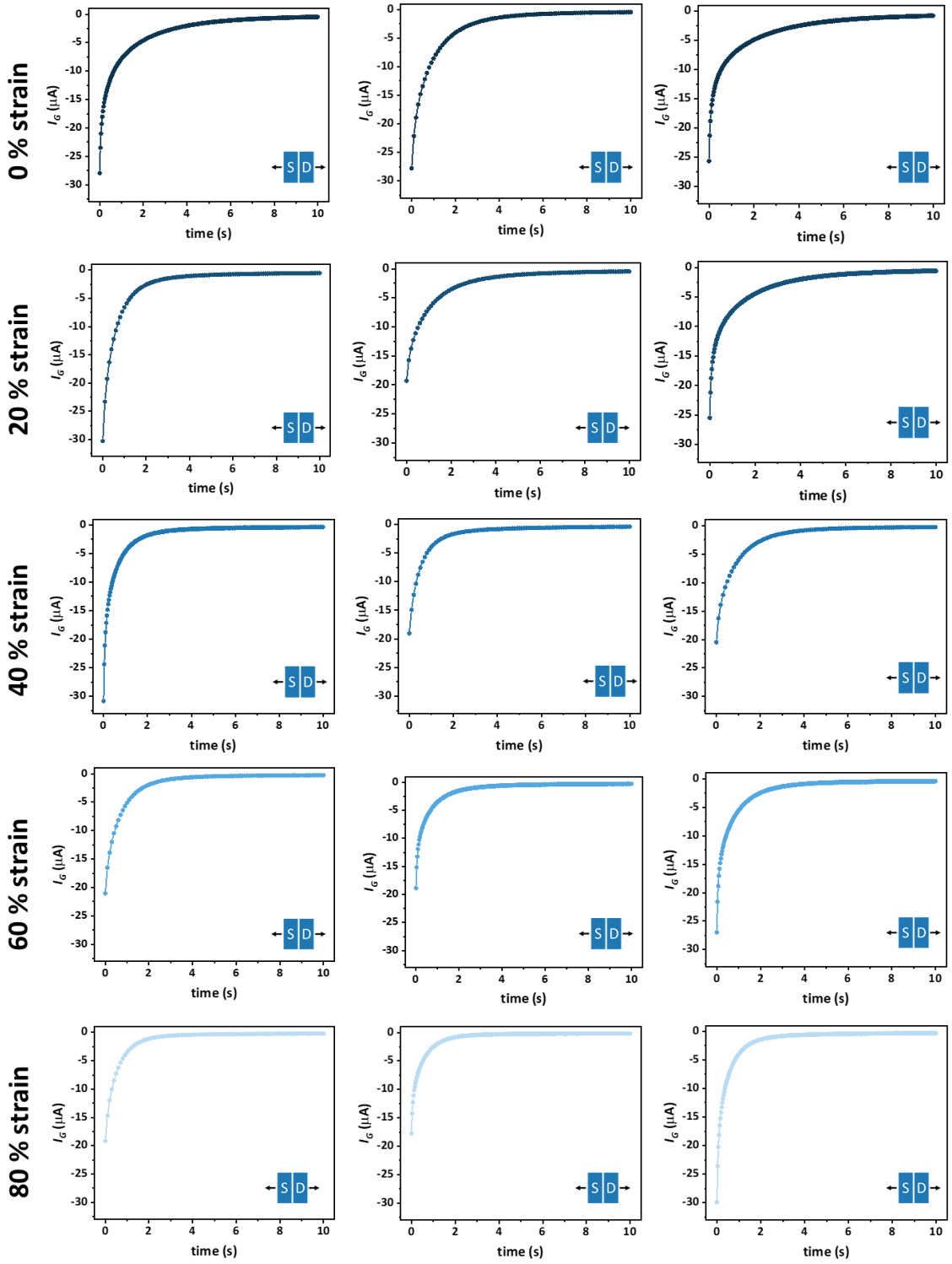

Figure S5.18: *Chronoamperometry of the parallel OECT arrangement at various strains.*

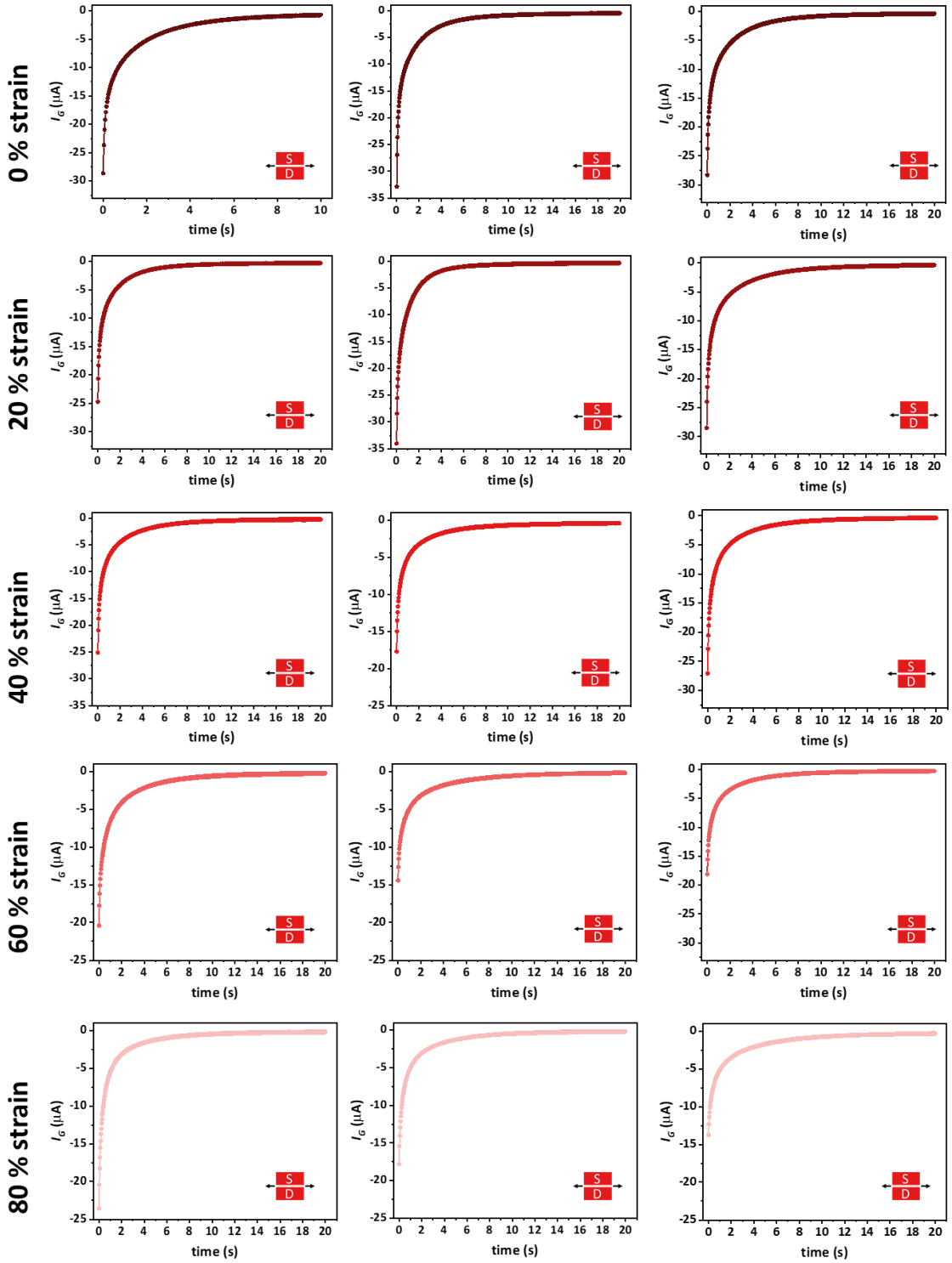

Figure S5.19: *Chronoamperometry of the parallel OECT arrangement at various strains.*

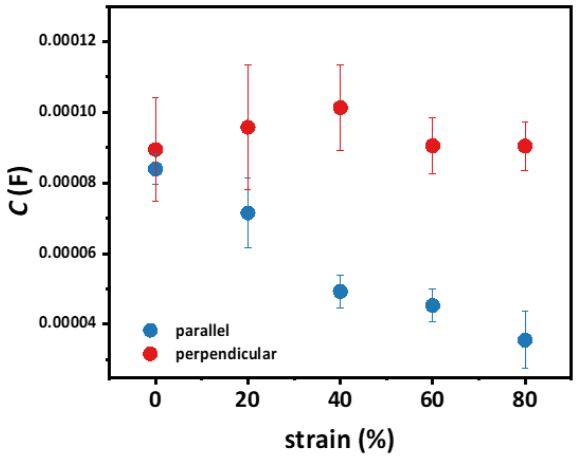

Figure S5.20: *Channel capacitance C_{ch} vs strain for the parallel and perpendicular OECT arrangement.*

6. Conclusions and Outlook

Concluding, this doctoral thesis established a pathway towards intrinsically stretchable OECTs through three interconnected projects, addressing key challenges in processing, morphology and electrical properties. These key challenges include reliably transferring PEDOT:PSS patterns onto stretchable substrates, understanding and tailoring PEDOT:PSS's response to strain via organic plasticizers and lastly generating a fundamental understanding of the effect of strain-induced morphological and geometrical changes within OECTs on their performance.

For reliable fabrication, O_2-plasma-patterned PEDOT:PSS was transfer-printed onto stretchable and biodegradable PVA:glycerol substrates. As discussed in **Chapter 3**, this method demonstrated compatibility with various PEDOT:PSS treatments designed to enhance conductivity and stretchability, all while preserving the integrity of the substrate. Additionally, it enabled large-area film transfers and offered water solubility, facilitating environmentally friendly disposal.

Chapter 4 examined the influence of an organic plasticizer on PEDOT:PSS morphology and electrical properties using the transfer-printing approach. The interaction between PEDOT:PSS, glycerol (acting as a plasticizer) and PVA (as a supporting substrate) in a stretchable bilayer system was analyzed through Flory-Huggins theory modeling, revealing a loading-dependent intermixing effect. The results showed that concentration-dependent plasticizer diffusion from the substrate into the conducting layer induces a rearrangement of PEDOT and PSS, forming better-connected PEDOT domains and enhancing conductivity. These effects were systematically studied using electrical characterization, microscopic imaging, scanning force microscopy and Raman spectroscopy. The improved adaptability to strain resulted in decreased resistance upon stretching, a higher onset strain for crack formation and strain-induced alignment of PEDOT chains. With increasing glycerol content, these effects became more pronounced, providing valuable insights for optimizing PEDOT:PSS performance in stretchable applications.

In **Chapter 5**, the findings from **Chapters 3** and **4** were integrated to fabricate intrinsically stretchable OECTs—devices that are inherently stretchable, without relying on structural design elements such as wavy interconnects or buckling (pre-straining). The relationship between device geometry, strain-induced morphological changes and overall performance was examined in detail. Two OECT configurations—parallel and perpendicular (referring to the current flow direction relative to the applied strain)—were studied to assess their effects on turn-off voltage, electrolyte resistance and device charge time. Additionally, the impact of strain-induced morphological changes on hole mobility and ionic uptake was investigated. While ionic uptake generally decreased under strain, hole mobility exhibited anisotropic behavior. These combined effects allowed the parallel OECT configuration to maintain its performance under strain, whereas the perpendicular configuration showed a significant decline. These results emphasize the central importance of geometric and morphological changes in stretchable OECTs and provide guidelines for the fabrication of next-generation intrinsically stretchable OECTs.

Future challenges include overcoming the water solubility of PVA substrates, which currently limits their suitability for certain applications, e.g. in aqueous environments. In addition, the development of (PVA-)systems that can recover their original shape after deformation is crucial for ensuring the long-term and cycling stability of these devices—a goal that may be achieved through techniques such as chemical cross-linking of the PVA chains. Further research is also needed in the field of non-toxic (solid-state) electrolytes, particularly with regard to their mechanical resilience and the impact of

deformation on the performance of OECT devices. And finally, the integration of these OECTs as (bio)sensors remains a key area for future developments. Despite these challenges, this doctoral thesis provides guidelines and design strategies to support further progress of intrinsically stretchable OECTs.

7. Experimental

This chapter supplements the work presented in **Chapters 3**, **4** and **5** by providing a detailed experimental description of the equipment developed, along with the design considerations involved in their creation. It covers electrical measurements conducted on both strained and unstrained samples, the design of intrinsically stretchable OECTs and the methods for evaluating their performance under strain. It is worth noting that this chapter does not provide detailed experimental procedures, e.g. sample preparation. For this, please refer to **Chapter 3** - **5**.

7.1 Electrical Characterization

In this work, two-point measurements were conducted. For this, electrodes with a large and smooth contact areas were employed. To determine the conductivity (σ), sheet resistance (R_s) and the change in resistance/resistance ratio relative to the initial resistance (R/R_0) for both strained and unstrained samples, the following equations were used:

$$\sigma = \frac{L}{RWt} \tag{7.1}$$

where L is the length, R is the resistance, W is the width and t is the thickness. R_s was calculated as:

$$R_s = \frac{1}{\sigma t} \tag{7.2}$$

Thus, accurate knowledge of the sample dimensions is essential to calculate both σ and R_s. As explained in **Chapter 1**, it is challenging to reliably know these dimensions, particularly under strain.

To connect the clamps/contacts to a source meter, banana plugs were utilized. Hence, all setups were designed accordingly.

Electrical Measurements on Unstrained Samples

Clamps in two sizes were developed for electrical measurements on unstrained samples. Metal pieces were welded onto crocodile clamps and coated with gold (see **Fig. 7.1**), between which a sample can be positioned. This way, tight and reliable contact could be established. The clamps can be clamped onto samples of different thicknesses and contacted with banana plugs, which in turn are connected to a source meter.

***Figure 7.1**: Metal clamps developed in two sizes to measure the electrical properties of unstrained conducting samples.*

Measuring Electrical Properties under Elongation

At the heart of the setup for electronically evaluating samples under strain is the stretch station, engineered to elongate samples uniformly in both directions simultaneously to ensure even stress distribution. A schematic representation of the setup is shown in **Fig. 7.2a**. To ensure consistent and reliable operation, the stretch station is motor-driven, providing precise control over adjustable input parameters such as the starting position and the elongation percentage. The sample under investigation is secured within the stretch station using metal brackets (made of brass). These clamps serve both physical and electrical purposes: they secure the sample and are coated with gold for good electrical contact. Furthermore, they contain metal sockets for connecting banana plugs (see **Fig. 7.2b**). In an earlier version of the stretch station the brackets were made of 3D-printed plastic but these proved inadequate for securely holding the sample during stretching. In contrast, the metal brackets have performed flawlessly and were found to impose negligible contact resistance.
The banana plugs are connected to a source meter (Keithley 2000 multimeter) for electrical measurements. Both the source meter and the motor are linked to a laptop via serial cables (RS cables). A custom program on the laptop enables automated tracking of electrical measurements by synchronizing inputs from the motor ('motor status'), which triggers data collection from the source meter. The primary data collected is the absolute resistance, which is processed using a Python script to calculate parameters such as conductivity (see **Eq. 7.1** and **7.2**). The results are then stored for further analysis.

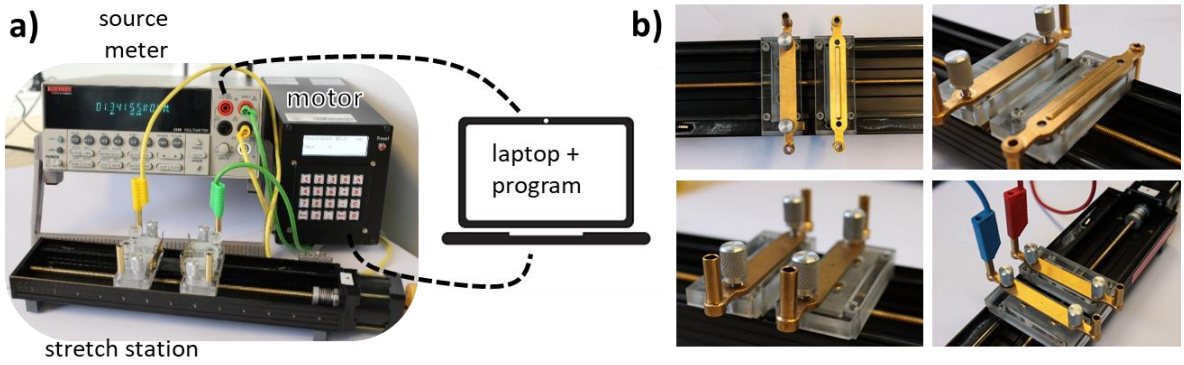

***Figure 7.2**: **a)** Experimental setup for evaluating electrical properties under strain, comprising a motor-driven stretch station, a source meter and a laptop for data acquisition and analysis. **b)** Brackets/mechanism designed to simultaneously establish both physical and electrical contact.*

The stretch station offers three distinct straining modes. The first mode is single-step strain, where the sample undergoes a single elongation to a specified percentage. The second mode, incremental straining, allows for gradual elongation in steps, with adjustable strain percentages and waiting periods between steps. The third mode, cyclic straining, involves repeatedly stretching and releasing the sample between defined strain percentages. These modes are visually depicted in **Fig. 7.3a**. Both the stretching speed and the strain percentage are adjustable for each mode and step, providing additional flexibility for experimental needs.

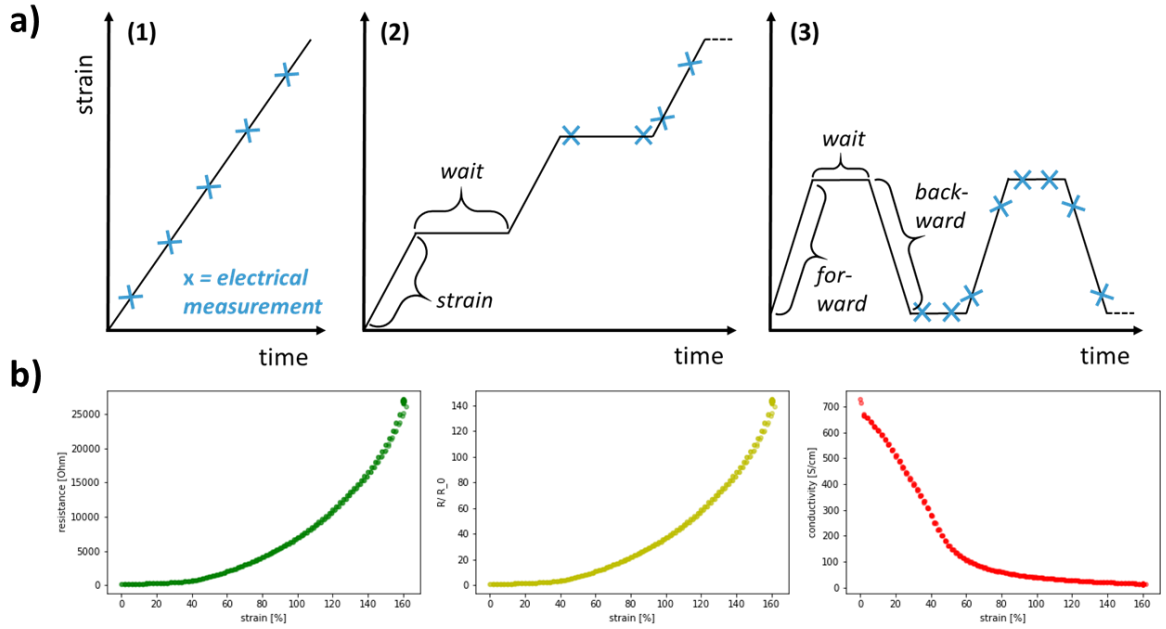

***Figure 7.3**: **a)** Strain modes the motorized stretch station can operate in. (1): single-step, (2) incremental straining and (3) cyclic straining. **b)** Date collected and plotted using strain mode (2). The blue "x" indicate the recording of the resistance.*

Upon completing an experiment, the program generates two CSV files and several plots. The first CSV file stores all input parameters, including the sample thickness, length, stretch time (and, if applicable, wait time and number of ramps), strain percentage at each step, stretching speed and total strain (see **Tab. 7.1**). This file serves as a detailed record of the experiment performed. The second CSV file contains both recorded and calculated data, including time stamps, time intervals between data points, motor status (for modes two and three), absolute length in millimeters at that point, strain percentage, absolute resistance, sheet resistance, R/R_0, conductivity, normalized conductivity, operation time, minimum and maximum normalized conductivity and the logarithm of R/R_0 (see **Tab. 7.2)**. To facilitate initial interpretation of the results, the program automatically generates plots of selected recorded and calculated values against strain or time. These visualizations provide a quick and informative overview of the experimental data. An example of such a plot is shown in **Fig. 7.3b**.

***Table 7.1**: Example of input parameters saved into a csv-file using the automated stretch station.*

thickness [cm]	length [mm]	width [mm]	stretch time [sec]	wait time [sec]	number of ramps	stretch% at each step [%]	speed [mm/s]	total stretch [%]
7.30E-06	30	25	10	30	60	2	0.06	120

***Table 7.2**: Data recorded and calculated running the Python code.*

time stamp	time diff [sec]	motor status	current length [mm]	strain percent [%]	*R* [Ohm]	R_S [Ohm/ square]	R/R_0	σ [S/cm]	normalized conductivity [%]	operation time [sec]	norm. cond.	$ln(R/R_0)$
10:37:08.0	0	**inital values**	30	0	1583960	14205.5	1	0.10378	100		0.009491	0
10:37:11.7	1.0044	R1			1586060		1.001326			10		0.0013249
10:37:19.8	9.0767	R1			1644688		1.038339			10		0.03762225
10:37:21.7	10.978	P1	30.6	2	1651956	1349636.9	1.042927	0.101499	97.8016367	30	0	0.0420315
10:37:49.8	39.035	P1	30.6	2	1616944	1349636.9	1.020823	0.103696	99.9193395	30	0.009143	0.02060956

7.2 Designing and Fabricating Stretchable OECTs

The fabrication of the stretchable OECTs utilized the setups described above (**Section 7.1**) as well as the patterning and transfer-printing method described in **Chapter 3**. PEDOT:PSS patterning and transfer-printing were used to fabricate the devices and the equipment was based on the (motorized) stretch station, which was adapted to be able to evaluate OECTs instead of uniform thin films. Two generations of OECTs were developed, with the second generation addressing the shortcomings identified in the first. Each generation required specific changes to the stretch station, however, both designs utilized an in-plane OECT configuration. While the data from the first generation OECT was not summarized in a separate chapter or manuscript, the development of this first setup is discussed here as it provides valuable insight into the key considerations for the design and evaluation of stretchable OECTs.

First Generation

With the materials and deposition methods established, the primary challenge was designing a mask to create an OECT. The metal mask for the first generation of OECTs including all measures is depicted in **Fig. 7.4a**. The mask was applied onto a spin-coated PEDOT:PSS thin film, which then underwent O_2-plasma treatment to remove all exposed areas. Any residual material that could cause shorts was manually removed using water and a cotton swab. The final step involved transfer-printing the patterned film, as illustrated in **Fig. 7.4b**. The patterned film was subsequently inserted into the stretch station using a designated bracket, shown in **Fig. 7.4b** and **c**. The bracket featured two separate contact areas enabling the connection of all three electrodes (gate, source and drain) through the bracket. Finally, the electrolyte was applied onto the device, as depicted also in **Fig. 7.4b**. In this first generation of OECTs, the electrolyte was manually cut to fit.

Key considerations in the design of the OECT (mask) included the ratio between the gate and channel, as well as the distance between them. As evident from **Fig. 7.4b** (3.), the channel (which is defined by the electrolyte, see also **Chapter 5**) is significantly smaller than the gate, a feature that literature suggests is advantageous for achieving high transconductance in the OECT[159]. Additionally, the channel width was designed to be narrow, with an emphasis on maximizing its length. Since the assembly process was performed manually, the dimensions were kept as small as practicable to align with these design goals.

Problems Encountered in the First Generation

One obvious problem was the fact that parts of the process were carried out manually. This of course affected reproducibility. In particular, the cutting of the electrolyte led to inaccuracies as the covered area defined the size of gate and channel. Another problem was the roughness of the bracket shown in **Fig. 7.4b**, which was found to scrape off parts of the underlying material. Although problematic, this is a fixable problem. And finally, a major flaw was found in the design of the mask. Revisiting **Fig. 7.4c**, it becomes evident that the distance between the electrodes/brackets (where the voltages are applied) and the channel or gate were very large. Worse still, this distance increased when stretched. These distances (or interconnects) add additional resistance to the system and were extremely difficult to account for during data analysis. Furthermore, the first generation did not allow to study potential anisotropy of the material and its impact on the charge transport as the OECTs were designed in such

a way, that the current flow along the channel from source to drain was aligned parallel with the direction of strain.

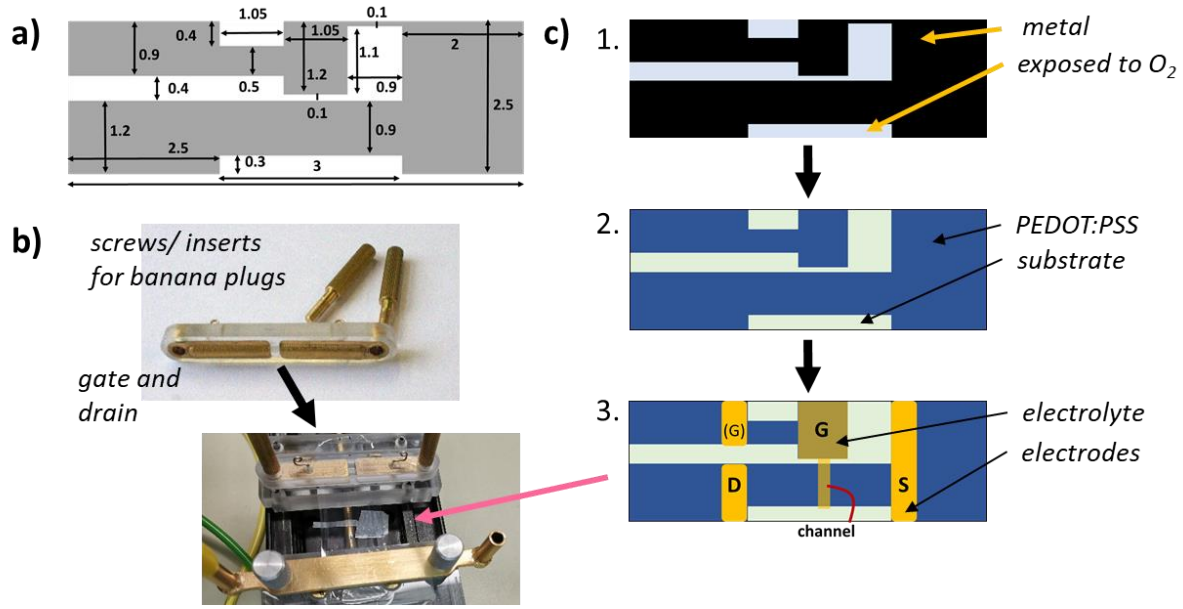

***Figure 7.4**: **a)** First-generation metal mask designed for patterning PEDOT:PSS in stretchable OECTs. **b)** Bracket designed to create source and drain contacts while using the stretch station. **c)** Fabrication process for the first generation of stretchable OECTs.*

Second Generation

In the second generation, the overall approach towards stretchable OECTs remained unchanged. This means that the materials, fabrication techniques as well as the placement of the electrolyte on top of the PEDOT:PSS remained unchanged. The above-mentioned pain points were addressed by updating the equipment used as well as designing new masks. First, stencils to cut the electrolyte were designed. This way, the gate and the channel are identical in size (see **Fig. 7.5a**). In total, three stencils were designed, offering different gate to channel ratios. Second, the contacting of the source and drain contacts and gate electrodes was altered by designing pins that can the inserted into manipulators and placed and moved around freely (see **Fig. 7.5b** and **c**). This way, they can be positioned right next to where the electrolyte defines gate and channel.

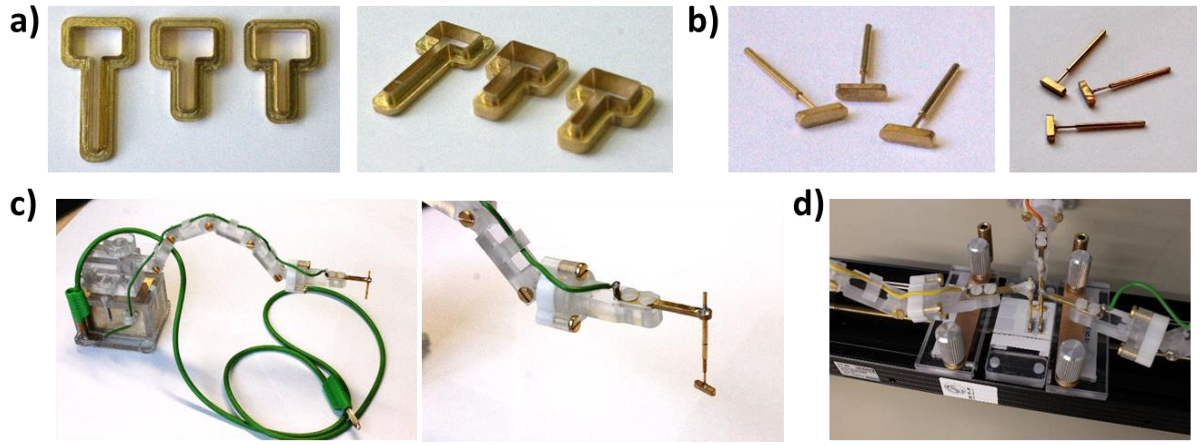

***Figure 7.5**: **a)** Stencils in different sizes to cut the solid state electrolyte. **b)** Contact pins to probe source, drain and gate. **c)** Manipulators to insert the metal pins. **d)** Set up including the metal pins and manipulators to contact OECTs.*

The updated mask design is shown in **Fig. 7.6a** and **b**. In total, four masks were designed. In two of them the current is flowing parallel to the direction of strain and in the other two perpendicular. Furthermore, the masks feature either a single or a double arrangement. The idea behind the double arrangement is that it allows to study two OECTs that are based on exactly the same material avoiding batch to batch fluctuation. As can be seen, the long interconnects, potentially imposing additional resistance, were removed in this design. The positioning of the source, drain and gate as well as the electrolyte can be understood in **Fig. 7.6c**.

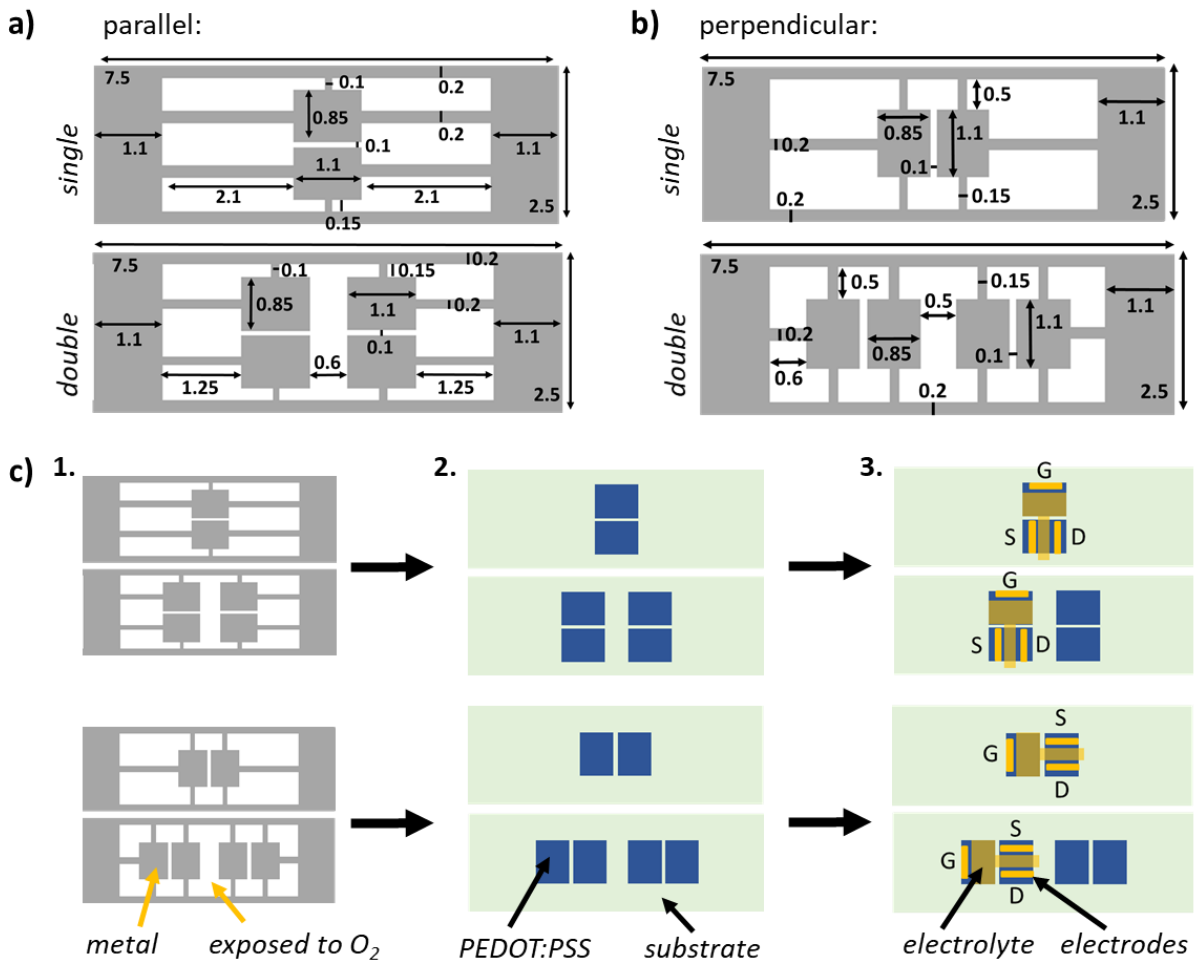

***Figure 7.6**: Metal masks employed to pattern PEDOT:PSS for stretchable OECTs. **a)** Single and double parallel OECT arrangement. **b)** Single and double perpendicular OECT arrangement. All measures are given in cm. **c)** Schematic illustration of the fabrication process of stretchable OECTs: 1. selection of the appropriate mask, 2. patterning via O_2-plasma treatment followed by manual removal of residual material using a cotton swab and 3. arranging the electrolyte and electrodes.*

8. References

[1] W. Gao, J. Qiao, J. Hu, Y. Guan, Q. Li, *Responsive Mater.* **2024**, *2*, e20230022.

[2] X. Fan, B. Xu, S. Liu, C. Cui, J. Wang, F. Yan, *ACS Appl. Mater. Interfaces* **2016**, *8*, 14029.

[3] J. Y. Oh, S. Rondeau-Gagné, Y. C. Chiu, A. Chortos, F. Lissel, G. J. N. Wang, B. C. Schroeder, T. Kurosawa, J. Lopez, T. Katsumata, J. Xu, C. Zhu, X. Gu, W. G. Bae, Y. Kim, L. Jin, J. W. Chung, J. B. H. Tok, Z. Bao, *Nature* **2016**, *539*, 411.

[4] W. Wang, S. Wang, R. Rastak, Y. Ochiai, S. Niu, Y. Jiang, P. K. Arunachala, Y. Zheng, J. Xu, N. Matsuhisa, X. Yan, S. K. Kwon, M. Miyakawa, Z. Zhang, R. Ning, A. M. Foudeh, Y. Yun, C. Linder, J. B. H. Tok, Z. Bao, *Nat. Electron.* **2021**, *4*, 143.

[5] S. Park, S. H. Kim, H. Lee, K. Cho, *npj Flex. Electron.* **2024**, *8*, 71.

[6] Z. Zhang, W. Wang, Y. Jiang, Y. X. Wang, Y. Wu, J. C. Lai, S. Niu, C. Xu, C. C. Shih, C. Wang, H. Yan, L. Galuska, N. Prine, H. C. Wu, D. Zhong, G. Chen, N. Matsuhisa, Y. Zheng, Z. Yu, Y. Wang, R. Dauskardt, X. Gu, J. B. H. Tok, Z. Bao, *Nature* **2022**, *603*, 624.

[7] S. Zhang, Y. Li, G. Tomasello, M. Anthonisen, X. Li, M. Mazzeo, A. Genco, P. Grutter, F. Cicoira, *Adv. Electron. Mater.* **2019**, *5*, 1900191.

[8] Y. Li, S. Zhang, X. Li, V. R. N. Unnava, F. Cicoira, *Flex. Print. Electron.* **2019**, *4*, 044004.

[9] D. Liu, X. Tian, J. Bai, Y. Wang, Y. Cheng, W. Ning, P. K. L. Chan, K. Wu, J. Sun, S. Zhang, *Adv. Sci.* **2022**, *9*, 2203418.

[10] O. Parlak, S. T. Keene, A. Marais, V. F. Curto, A. Salleo, *Sci. Adv.* **2018**, 4 : eaar2904.

[11] R. Colucci, D. A. Koutsouras, S. Morsbach, P. Gkoupidenis, P. W. M. Blom, U. Kraft, *ACS Appl. Electron. Mater.* **2024**, *6*, 2739.

[12] Y. Cui, G. Zheng, Z. Jiang, M. Zhou, P. Wang, Y. Yu, Q. Wang, *Compos. Part A Appl. Sci. Manuf.* **2022**, *163*, 107245.

[13] A. Lund, Y. Wu, B. Fenech-Salerno, F. Torrisi, T. B. Carmichael, C. Müller, *MRS Bull.* **2021**, *46*, 491.

[14] L. V. Kayser, D. J. Lipomi, *Adv. Mater.* **2019**, *31*, 1806133.

[15] M. Drack, I. Graz, T. Sekitani, T. Someya, M. Kaltenbrunner, S. Bauer, *Adv. Mater.* **2014**, *27*, 34.

[16] W. Lee, S. Kobayashi, M. Nagase, Y. Jimbo, I. Saito, Y. Inoue, T. Yambe, M. Sekino, G. G. Malliaras, T. Yokota, M. Tanaka, T. Someya, *Sci. Adv.* **2018**, *4*, eaau2426.

[17] J. Mun, Y. Ochiai, W. Wang, Y. Zheng, Y. Q. Zheng, H. C. Wu, N. Matsuhisa, T. Higashihara, J. B. H. Tok, Y. Yun, Z. Bao, *Nat. Commun.* **2021**, *12*, 3572.

[18] D. Ohayon, V. Druet, S. Inal, *Chem. Soc. Rev.* **2023**, *52*, 1001.

[19] G. Malliaras, I. McCulloch, *Chem. Rev.* **2022**, *122*, 4323.

[20] J. Rivnay, S. Inal, A. Salleo, R. M. Owens, M. Berggren, G. G. Malliaras, *Nat. Rev. Mater.* **2018**, *3*, 17086.

[21] Y. Wang, S. Wustoni, J. Surgailis, Y. Zhong, A. Koklu, S. Inal, *Nat. Rev. Mater.* **2024**, *9*, 249.

[22] J. T. Friedlein, R. R. McLeod, J. Rivnay, *Org. Electron.* **2018**, *63*, 398.

[23] Y. Van De Burgt, E. Lubberman, E. J. Fuller, S. T. Keene, G. C. Faria, S. Agarwal, M. J. Marinella, A. Alec Talin, A. Salleo, *Nat. Mater.* **2017**, *16*, 414.

[24] P. Gkoupidenis, N. Schaefer, B. Garlan, G. G. Malliaras, *Adv. Mater.* **2015**, *27*, 7176.

[25] S. L. Bidinger, S. Han, G. G. Malliaras, T. Hasan, *Appl. Phys. Lett.* **2022**, *120*, 073302.

[26] M. Ashizawa, Y. Zheng, H. Tran, Z. Bao, *Prog. Polym. Sci.* **2020**, *100*, 101181.

[27] G. J. N. Wang, A. Gasperini, Z. Bao, *Adv. Electron. Mater.* **2018**, *4*, 1700429.

[28] I. E. Jacobs, A. J. Moulé, *Adv. Mater.* **2017**, *29*, 1703063.

[29] T. M. Swager, *Macromolecules* **2017**, *50*, 4867.

[30] S. E. Root, S. Savagatrup, A. D. Printz, D. Rodriquez, D. J. Lipomi, *Chem. Rev.* **2017**, *117*, 6467.

[31] W. Brütting, *Introduction to the Physics of Organic Semiconductors*, WILEY-VCH Verlag GmbH & Co. KGaA, Weinheim **2005**.

[32] S. Koltzenburg, M. Maskos, O. Nuyken, *Polymere: Synthese, Eigenschaften und Anwendungen*, Springer Spektrum Berlin, Heidelberg **2014**.

[33] R. Noriega, J. Rivnay, K. Vandewal, F. P. V. Koch, N. Stingelin, P. Smith, M. F. Toney, A. Salleo, *Nat. Mater.* **2013**, *12*, 1038.

[34] S. Thankaraj Salammal, J. Chen, F. Ullah, H. Chen, *J. Inorg. Organomet. Polym. Mater.* **2015**, *25*, 12.

[35] P. W. M. Blom, *Adv. Mater. Technol.* **2020**, *5*, 2000144.

[36] Y. Zheng, S. Zhang, J. B. H. Tok, Z. Bao, *J. Am. Chem. Soc.* **2022**, *144*, 4699.

[37] X. Fan, W. Nie, H. Tsai, N. Wang, H. Huang, Y. Cheng, R. Wen, L. Ma, F. Yan, Y. Xia, *Adv. Sci.* **2019**, *6*, 1900813.

[38] D. Choi, H. Kim, N. Persson, P. H. Chu, M. Chang, J. H. Kang, S. Graham, E. Reichmanis, *Chem. Mater.* **2016**, *28*, 1196.

[39] J. Mun, J. Kang, Y. Zheng, S. Luo, Y. Wu, H. Gong, J. C. Lai, H. C. Wu, G. Xue, J. B. H. Tok, Z. Bao, *Adv. Electron. Mater.* **2020**, *6*, 2000251.

[40] H. He, L. Zhang, S. Yue, S. Yu, J. Wei, J. Ouyang, *Macromolecules* **2021**, *54*, 1234.

[41] N. Kim, S. Lienemann, I. Petsagkourakis, D. Alemu Mengistie, S. Kee, T. Ederth, V. Gueskine, P. Leclère, R. Lazzaroni, X. Crispin, K. Tybrandt, *Nat. Commun.* **2020**, *11*, 1424.

[42] Y. Yang, G. Zhao, X. Cheng, H. Deng, Q. Fu, *ACS Appl. Mater. Interfaces* **2021**, *13*, 14599.

[43] K. Ditte, J. Perez, S. Chae, M. Hambsch, M. Al-Hussein, H. Komber, P. Formanek, S. C. B. Mannsfeld, A. Fery, A. Kiriy, F. Lissel, *Adv. Mater.* **2021**, *33*, 2005416.

[44] Y. Zheng, Z. Yu, S. Zhang, X. Kong, W. Michaels, W. Wang, G. Chen, D. Liu, J. C. Lai, N. Prine, W. Zhang, S. Nikzad, C. B. Cooper, D. Zhong, J. Mun, Z. Zhang, J. Kang, J. B. H. Tok, I. McCulloch, J. Qin, X. Gu, Z. Bao, *Nat. Commun.* **2021**, *12*, 5701.

[45] S. Savagatrup, X. Zhao, E. Chan, J. Mei, D. J. Lipomi, *Macromol. Rapid Commun.* **2016**, *37*, 1623.

[46] S. Zhang, A. Alesadi, G. T. Mason, K. L. Chen, G. Freychet, L. Galuska, Y. H. Cheng, P. B. J. St. Onge, M. U. Ocheje, G. Ma, Z. Qian, S. Dhakal, Z. Ahmad, C. Wang, Y. C. Chiu, S. Rondeau-Gagné, W. Xia, X. Gu, *Adv. Funct. Mater.* **2021**, *31*, 2100161.

[47] C. Lu, W. Y. Lee, X. Gu, J. Xu, H. H. Chou, H. Yan, Y. C. Chiu, M. He, J. R. Matthews, W. Niu, J. B. H. Tok, M. F. Toney, W. C. Chen, Z. Bao, *Adv. Electron. Mater.* **2017**, *3*, 1600311.

[48] H. F. Wen, H. C. Wu, J. Aimi, C. C. Hung, Y. C. Chiang, C. C. Kuo, W. C. Chen, *Macromolecules* **2017**, *50*, 4982.

[49] H. Shi, C. Liu, Q. Jiang, J. Xu, *Adv. Electron. Mater.* **2015**, 1: 1500017.

[50] J. G. Troughton, B. Marchiori, R. Delattre, S. Escoubas, M. Y. Aliouat, S. Grigorian, M. Ramuz, *Org. Electron.* **2021**, *92*, 106108.

[51] J. Rivnay, S. Inal, B. A. Collins, M. Sessolo, E. Stavrinidou, X. Strakosas, C. Tassone, D. M. Delongchamp, G. G. Malliaras, *Nat. Commun.* **2016**, *7*, 11287.

[52] U. Kraft, F. Molina-Lopez, D. Son, Z. Bao, B. Murmann, *Adv. Electron. Mater.* **2020**, *6*, 1900681.

[53] M. Skowrons, A. Schander, A. G. P. Negron, B. Lüssem, *Adv. Electron. Mater.* **2024**, *10*, 2300673.

[54] L. V. Kayser, M. D. Russell, D. Rodriquez, S. N. Abuhamdieh, C. Dhong, S. Khan, A. N. Stein, J. Ramírez, D. J. Lipomi, *Chem. Mater.* **2018**, *30*, 4459.

[55] T. S. Hansen, K. West, O. Hassager, N. B. Larsen, *Adv. Funct. Mater.* **2007**, *17*, 3069.

[56] B. Lu, H. Yuk, S. Lin, N. Jian, K. Qu, J. Xu, X. Zhao, *Nat. Commun.* **2019**, *10*, 1043.

[57] Y. Y. Lee, H. Y. Kang, S. H. Gwon, G. M. Choi, S. M. Lim, J. Y. Sun, Y. C. Joo, *Adv. Mater.* **2016**, *28*, 1636.

[58] P. Gu, L. Lu, X. Yang, Z. Hu, X. Zhang, Z. Sun, X. Liang, M. Liu, Q. Sun, J. Huang, G. Zu, *Adv. Funct. Mater.* **2024**, *34*, 2400589.

[59] N. Matsuhisa, X. Chen, Z. Bao, T. Someya, *Chem. Soc. Rev.* **2019**, *48*, 2946.

[60] Y. Li, Y. Pang, L. Wang, Q. Li, B. Liu, J. Li, S. Liu, *Adv. Mater.* **2024**, *36*, 2310973.

[61] C. H. Chen, A. Torrents, L. Kulinsky, R. D. Nelson, M. J. Madou, L. Valdevit, J. C. Larue, *Synth. Met.* **2011**, *161*, 2259.

[62] P. Li, K. Sun, J. Ouyang, *ACS Appl. Mater. Interfaces* **2015**, *7*, 18415.

[63] Y. Wang, C. Zhu, R. Pfattner, H. Yan, L. Jin, S. Chen, F. Molina-Lopez, F. Lissel, J. Liu, N. I. Rabiah, Z. Chen, J. W. Chung, C. Linder, M. F. Toney, B. Murmann, Z. Bao, *Sci. Adv.* **2017**, *3*, e1602076.

[64] M. Y. Teo, N. Kim, S. Kee, B. S. Kim, G. Kim, S. Hong, S. Jung, K. Lee, *ACS Appl. Mater. Interfaces* **2017**, *9*, 819.

[65] S. Kee, N. Kim, H. Park, B. S. Kim, M. Y. Teo, S. Lee, J. Kim, K. Lee, *Macromol. Chem. Phys.* **2020**, *221*, 2000291.

[66] M. Kim, S. Y. Lee, J. Kim, C. Choi, Y. Lansac, H. Ahn, S. Park, Y. H. Jang, S. H. Lee, B. H. Lee, *ACS Appl. Mater. Interfaces* **2022**, *15*, 3202.

[67] T. Shimura, S. Sato, T. Tominaga, S. Abe, K. Yamashita, M. Ashizawa, T. Kato, H. Ishikuro, N. Matsuhisa, *Adv. Mater. Technol.* **2023**, 8: 2201992.

[68] H. He, L. Zhang, X. Guan, H. Cheng, X. Liu, S. Yu, J. Wei, J. Ouyang, *ACS Appl. Mater. Interfaces* **2019**, *11*, 26185.

[69] J. Y. Oh, M. Shin, J. B. Lee, J. H. Ahn, H. K. Baik, U. Jeong, *ACS Appl. Mater. Interfaces* **2014**, *6*,

6954.

[70] Z. Rao, A. Thukral, P. Yang, Y. Lu, H. Shim, W. Wu, A. Karim, C. Yu, *Adv. Funct. Mater.* **2022**, *32*, 2111232.

[71] O. Jin Young, S. Kim, H. K. Baik, U. Jeong, *Adv. Mater.* **2016**, *28*, 4455.

[72] J. Cao, X. Yang, J. Rao, A. Mitriashkin, X. Fan, R. Chen, H. Cheng, X. Wang, J. Goh, H. L. Leo, J. Ouyang, *ACS Appl. Mater. Interfaces* **2022**.

[73] J. H. Lee, Y. R. Jeong, G. Lee, S. W. Jin, Y. H. Lee, S. Y. Hong, H. Park, J. W. Kim, S. S. Lee, J. S. Ha, *ACS Appl. Mater. Interfaces* **2018**, *10*, 28027.

[74] J. S. Noh, *RSC Adv.* **2014**, *4*, 1857.

[75] K. Rohtlaid, G. T. M. Nguyen, C. Soyer, E. Cattan, F. Vidal, C. Plesse, *Adv. Electron. Mater.* **2019**, *5*, 1800948.

[76] M. Geetha, C. Roslan, J. Cabibihan, **2023**, *13*, 8202.

[77] R. Luo, H. Li, B. Du, S. Zhou, Y. Zhu, *Org. Electron.* **2020**, *76*, 105451.

[78] X. Fan, N. Wang, J. Wang, B. Xu, F. Yan, *Mater. Chem. Front.* **2018**, *2*, 355.

[79] A. M. Nardes, M. Kemerink, R. A. J. Janssen, J. A. M. Bastiaansen, N. M. M. Kiggen, B. M. W. Langeveld, A. J. J. M. Van Breemen, M. M. De Kok, *Adv. Mater.* **2007**, *19*, 1196.

[80] Y. Y. Lee, J. H. Lee, J. Y. Cho, N. R. Kim, D. H. Nam, I. S. Choi, K. T. Nam, Y. C. Joo, *Adv. Funct. Mater.* **2013**, *23*, 4020.

[81] Y. Y. Lee, G. M. Choi, S. M. Lim, J. Y. Cho, I. S. Choi, K. T. Nam, Y. C. Joo, *Sci. Rep.* **2016**, *6*, 25332.

[82] L. V. Lingstedt, M. Ghittorelli, H. Lu, D. A. Koutsouras, T. Marszalek, F. Torricelli, N. I. Crăciun, P. Gkoupidenis, P. W. M. Blom, *Adv. Electron. Mater.* **2019**, *5*, 1800804.

[83] N. A. Shahrim, Z. Ahmad, A. Wong Azman, Y. Fachmi Buys, N. Sarifuddin, *Mater. Adv.* **2021**, *2*, 7118.

[84] D. Alemu Mengistie, P. C. Wang, C. W. Chu, *J. Mater. Chem. A* **2013**, *1*, 9907.

[85] J. Ouyang, Q. Xu, C. W. Chu, Y. Yang, G. Li, J. Shinar, *Polymer (Guildf).* **2004**, *45*, 8443.

[86] J. H. Shin, J. Y. Choi, K. June, H. Choi, T. il Kim, *Adv. Mater.* **2024**, *36*, 2313157.

[87] S. Savagatrup, E. Chan, S. M. Renteria-Garcia, A. D. Printz, A. V. Zaretski, T. F. O'Connor, D. Rodriquez, E. Valle, D. J. Lipomi, *Adv. Funct. Mater.* **2015**, *25*, 427.

[88] D. J. Lipomi, J. A. Lee, M. Vosgueritchian, B. C. Tee, J. A. Bolander, *Chem. Mater.* **2012**, *24*, 373.

[89] V. Vijay, A. D. Rao, K. S. Narayan, *J. Appl. Phys.* **2011**, *109*, 084525.

[90] D. Liu, X. Tian, J. Bai, S. Wang, S. Dai, Y. Wang, Z. Wang, S. Zhang, *Nat. Electron.* **2024**, *7*, 1176.

[91] J. C. Ho, Y. C. Lin, C. K. Chen, L. C. Hsu, W. C. Chen, *Org. Electron.* **2022**, *100*, 106358.

[92] S. Zhang, H. Ling, Y. Chen, Q. Cui, J. Ni, X. Wang, M. C. Hartel, X. Meng, K. J. Lee, J. Lee, W. Sun, H. Lin, S. Emaminejad, S. Ahadian, N. Ashammakhi, M. R. Dokmeci, A. Khademhosseini, *Adv. Funct. Mater.* **2020**, *30*, 1906016.

[93] X. Fan, W. Song, T. Lei, B. Xu, F. Yan, N. Wang, H. Cui, Z. Ge, *Mater. Chem. Front.* **2019**, *3*, 901.

[94] N. Kim, H. Kang, J. H. Lee, S. Kee, S. H. Lee, K. Lee, *Adv. Mater.* **2015**, *27*, 2317.

[95] J. K. Kim, W. Kim, D. H. Wang, H. Lee, S. M. Cho, D. Choi, J. H. Park, *Langmuir* **2013**, *29*, 5377.

[96] J. K. Kim, G. Veerappan, N. Heo, D. H. Wang, J. H. Park, *J. Phys. Chem. C* **2014**, *118*, 22672.

[97] C. H. Kim, M. Azimi, J. Fan, H. Nagarajan, M. Wang, F. Cicoira, *Nanoscale* **2023**, *15*, 3263.

[98] S. Park, C. W. Lee, J. M. Kim, *Org. Electron.* **2018**, *58*, 1.

[99] J. Cao, X. Yang, J. Rao, A. Mitriashkin, X. Fan, R. Chen, H. Cheng, X. Wang, J. Goh, H. L. Leo, J. Ouyang, *ACS Appl. Mater. Interfaces* **2022**, *14*, 39159.

[100] S. Zhang, E. Hubis, C. Girard, P. Kumar, J. DeFranco, F. Cicoira, *J. Mater. Chem. C* **2016**, *4*, 1382.

[101] Y. Li, N. Wang, A. Yang, H. Ling, F. Yan, *Adv. Electron. Mater.* **2019**, *5*, 1900566.

[102] J. M. Nassar, S. M. Khan, D. R. Villalva, M. M. Nour, A. S. Almuslem, M. M. Hussain, *npj Flex. Electron.* **2018**, *2*, 24.

[103] I. Miccoli, F. Edler, H. Pfnür, C. Tegenkamp, *J. Phys. Condens. Matter* **2015**, *27*, 223201.

[104] P. W. McMullin, *Mechanics of materials*, McGraw-Hill Education **2016**.

[105] Y. Dai, S. Dai, N. Li, Y. Li, M. Moser, J. Strzalka, A. Prominski, Y. Liu, Q. Zhang, S. Li, H. Hu, W. Liu, S. Chatterji, P. Cheng, B. Tian, I. McCulloch, J. Xu, S. Wang, *Adv. Mater.* **2022**, *34*, 2201178.

[106] N. Matsuhisa, Y. Jiang, Z. Liu, G. Chen, C. Wan, Y. Kim, J. Kang, H. Tran, H. C. Wu, I. You, Z. Bao, X. Chen, *Adv. Electron. Mater.* **2019**, *5*, 1900347.

[107] J. Chen, W. Huang, D. Zheng, Z. Xie, X. Zhuang, D. Zhao, Y. Chen, N. Su, H. Chen, R. M. Pankow, Z. Gao, J. Yu, X. Guo, Y. Cheng, J. Strzalka, X. Yu, T. J. Marks, A. Facchetti, *Nat. Mater.* **2022**, *21*, 564.

[108] H. M. Schrickx, P. Sen, N. Balar, B. T. O'Connor, *Cell Reports Phys. Sci.* **2024**, *5*, 102076.

[109] H. Tian, L. Yuan, D. Zhou, J. Niu, H. Cong, A. Xiang, *Polym. Adv. Technol.* **2018**, *29*, 2612.

[110] L. Meng, J. Xu, X. Chen, N. Tian, Y. Lin, K. Cui, J. Li, L. Li, *Polym. Test.* **2014**, *36*, 110.

[111] C. I. Martins, M. Cakmak, *Polymer (Guildf).* **2007**, *48*, 2109.

[112] B. O'Connor, R. J. Kline, B. R. Conrad, L. J. Richter, D. Gundlach, M. F. Toney, D. M. DeLongchamp, *Adv. Funct. Mater.* **2011**, *21*, 3697.

[113] P. Sen, R. Yang, J. J. Rech, Y. Feng, C. H. Y. Ho, J. Huang, F. So, R. J. Kline, W. You, M. W. Kudenov, B. T. O'Connor, *Adv. Opt. Mater.* **2019**, *7*, 1801346.

[114] H. S. White, G. P. Kittlesen, M. S. Wrighton, *J. Am. Chem. Soc.* **1984**, *106*, 5375.

[115] A. Weissbach, M. Cucchi, H. Tseng, K. Leo, H. Kleemann, *Adv. Funct. Mater.* **2023**, *33*, 2302205.

[116] J. Rivnay, P. Leleux, M. Sessolo, D. Khodagholy, T. Hervé, M. Fiocchi, G. G. Malliaras, *Adv. Mater.* **2013**, *25*, 7010.

[117] P. Lin, F. Yan, *Adv. Mater.* **2012**, *24*, 34.

[118] S. Inal, G. G. Malliaras, J. Rivnay, *Nat. Commun.* **2017**, *8*, 1767.

[119] P. Schmode, D. Ohayon, P. M. Reichstein, A. Savva, S. Inal, M. Thelakkat, *Chem. Mater.* **2019**, *31*, 5286.

[120] S. Inal, J. Rivnay, P. Leleux, M. Ferro, M. Ramuz, J. C. Brendel, M. M. Schmidt, M. Thelakkat, G. G. Malliaras, *Adv. Mater.* **2014**, *26*, 7450.

[121] V. Venkatraman, J. T. Friedlein, A. Giovannitti, I. P. Maria, I. McCulloch, R. R. McLeod, J. Rivnay, *Adv. Sci.* **2018**, *5*, 1800453.

[122] A. Savva, R. Hallani, C. Cendra, J. Surgailis, T. C. Hidalgo, S. Wustoni, R. Sheelamanthula, X. Chen, M. Kirkus, A. Giovannitti, A. Salleo, I. McCulloch, S. Inal, *Adv. Funct. Mater.* **2020**, *30*, 1907657.

[123] C. M. Proctor, J. Rivnay, G. G. Malliaras, *J. Polym. Sci. Part B Polym. Phys.* **2016**, *54*, 1433.

[124] Y. Yao, W. Huang, J. Chen, X. Liu, L. Bai, W. Chen, Y. Cheng, J. Ping, T. J. Marks, A. Facchetti, *Adv. Mater.* **2023**, *35*, 2209906.

[125] D. Khodagholy, T. Doublet, P. Quilichini, M. Gurfinkel, P. Leleux, A. Ghestem, E. Ismailova, T. Hervé, S. Sanaur, C. Bernard, G. G. Malliaras, *Nat. Commun.* **2013**, *4*, 1575.

[126] J. Rivnay, P. Leleux, M. Ferro, M. Sessolo, A. Williamson, D. A. Koutsouras, D. Khodagholy, M. Ramuz, X. Strakosas, R. M. Owens, C. Benar, J. M. Badier, C. Bernard, G. G. Malliaras, *Sci. Adv.* **2015**, *1*, e1400251.

[127] A. Tricoli, N. Nasiri, S. De, *Adv. Funct. Mater.* **2017**, *27*, 1605271.

[128] Z. Zhao, Z. Tian, F. Yan, *Cell Reports Phys. Sci.* **2023**, *4*, 101673.

[129] J. Zaumseil, H. Sirringhaus, *Chem. Rev.* **2007**, *107*, 1296.

[130] M. J. Donahue, A. Williamson, X. Strakosas, J. T. Friedlein, R. R. McLeod, H. Gleskova, G. G. Malliaras, *Adv. Mater.* **2018**, *30*, 1705031.

[131] C. B. Nielsen, A. Giovannitti, D. T. Sbircea, E. Bandiello, M. R. Niazi, D. A. Hanifi, M. Sessolo, A. Amassian, G. G. Malliaras, J. Rivnay, I. McCulloch, *J. Am. Chem. Soc.* **2016**, *138*, 10252.

[132] R. Colucci, H. F. D. P. Barbosa, F. Günther, P. Cavassin, G. C. Faria, *Flex. Print. Electron.* **2020**, *5*, 013001.

[133] D. A. Bernards, G. G. Malliaras, *Adv. Funct. Mater.* **2007**, *17*, 3538.

[134] M. C. J. M. Vissenberg, M. Matters, *Phys. Rev. B* **1998**, *57*, 12964.

[135] L. F. Santos, R. M. Faria, A. R. de Andrade, G. C. Faria, C. A. Amorin, S. Mergulhão, *Thin Solid Films* **2007**, *515*, 8034.

[136] H. Bässler, *Phys. Status Solidi* **1993**, *175*, 15.

[137] R. Colucci, B. de A. Feitosa, G. C. Faria, *Adv. Electron. Mater.* **2024**, *10*, 2300235.

[138] S. M. Kim, C. H. Kim, Y. Kim, N. Kim, W. J. Lee, E. H. Lee, D. Kim, S. Park, K. Lee, J. Rivnay, M. H. Yoon, *Nat. Commun.* **2018**, *9*, 3858.

[139] C. Cendra, A. Giovannitti, A. Savva, V. Venkatraman, I. McCulloch, A. Salleo, S. Inal, J. Rivnay, *Adv. Funct. Mater.* **2019**, *29*, 1807034.

[140] G. Sych, P. Rannou, M. Jullien-Palletier, S. Sadki, Y. Bonnassieux, S. Sanaur, *Adv. Electron. Mater.* **2023**, *0*, 2201067.

[141] J. Rivnay, M. Ramuz, P. Leleux, A. Hama, M. Huerta, R. M. Owens, *Appl. Phys. Lett.* **2015**, *106*, 043301.

[142] D. A. Koutsouras, M. H. Amiri, P. W. M. Blom, F. Torricelli, K. Asadi, P. Gkoupidenis, *Adv. Funct.*

Mater. **2021**, *31*, 2011013.

[143] E. Stavrinidou, M. Sessolo, B. Winther-Jensen, S. Sanaur, G. G. Malliaras, *AIP Adv.* **2014**, *4*, 017127.

[144] D. A. Koutsouras, L. V. Lingstedt, K. Lieberth, J. Reinholz, V. Mailänder, P. W. M. Blom, P. Gkoupidenis, *Adv. Healthc. Mater.* **2019**, *8*, 1901215.

[145] A. V. Volkov, K. Wijeratne, E. Mitraka, U. Ail, D. Zhao, K. Tybrandt, J. W. Andreasen, M. Berggren, X. Crispin, I. V. Zozoulenko, *Adv. Funct. Mater.* **2017**, *27*, 1700329.

[146] P. Barthó, H. Hirase, L. Monconduit, M. Zugaro, K. D. Harris, G. Buzsáki, *J. Neurophysiol.* **2004**, *92*, 600.

[147] K. Tybrandt, S. B. Kollipara, M. Berggren, *Sensors Actuators, B Chem.* **2014**, *195*, 651.

[148] G. Rebetez, O. Bardagot, J. Affolter, J. Réhault, N. Banerji, *Adv. Funct. Mater.* **2022**, *32*, 2105821.

[149] E. Stavrinidou, P. Leleux, H. Rajaona, D. Khodagholy, J. Rivnay, M. Lindau, S. Sanaur, G. G. Malliaras, *Adv. Mater.* **2013**, *25*, 4488.

[150] Y. Zhong, P. D. Nayak, S. Wustoni, J. Surgailis, J. Z. Parrado Agudelo, A. Marks, I. McCulloch, S. Inal, *ACS Appl. Mater. Interfaces* **2023**, *16*, 61457.

[151] X. Wu, M. Stephen, T. C. Hidalgo, T. Salim, J. Surgailis, A. Surendran, X. Su, T. Li, S. Inal, W. L. Leong, *Adv. Funct. Mater.* **2022**, *32*, 2108510.

[152] X. Wu, S. Chen, M. Moser, A. Moudgil, S. Griggs, A. Marks, T. Li, I. McCulloch, W. L. Leong, *Adv. Funct. Mater.* **2023**, *33*, 2209354.

[153] T. Nguyen-Dang, K. Harrison, A. Lill, A. Dixon, E. Lewis, J. Vollbrecht, T. Hachisu, S. Biswas, Y. Visell, T. Q. Nguyen, *Adv. Electron. Mater.* **2021**, *7*, 2100519.

[154] F. Hofmeister, *Arch. für Exp. Pathol. und Pharmakologie* **1888**, *24*, 247.

[155] L. Q. Flagg, C. G. Bischak, J. W. Onorato, R. B. Rashid, C. K. Luscombe, D. S. Ginger, *J. Am. Chem. Soc.* **2019**, *141*, 4345.

[156] L. Q. Flagg, R. Giridharagopal, J. Guo, D. S. Ginger, *Chem. Mater.* **2018**, *30*, 5380.

[157] S. Dai, X. Zhang, X. Liu, X. Tian, B. Cui, I. Pang, H. Luo, D. Liu, X. He, X. Chen, J. Zhang, Z. Wang, J. Huang, S. Zhang, *Adv. Mater.* **2024**, *37*, 2413951.

[158] D. J. Coutinho, B. de Andrade Feitosa, H. F. de Paula Barbosa, R. Colucci, B. B. M. Torres, G. C. Faria, *J. Phys. Chem. C* **2023**, *127*, 24443.

[159] D. A. Koutsouras, F. Torricelli, P. Gkoupidenis, P. W. M. Blom, *Adv. Mater. Technol.* **2021**, *6*, 2100732.

[160] V. Kostianovskii, B. Sanyoto, Y. Y. Noh, *Org. Electron.* **2017**, *44*, 99.

[161] M. Zabihipour, R. Lassnig, J. Strandberg, M. Berggren, S. Fabiano, I. Engquist, P. Andersson Ersman, *npj Flex. Electron.* **2020**, *4*, 15.

[162] F. Molina-Lopez, T. Z. Gao, U. Kraft, C. Zhu, T. Öhlund, R. Pfattner, V. R. Feig, Y. Kim, S. Wang, Y. Yun, Z. Bao, *Nat. Commun.* **2019**, *10*, 2676.

[163] D. A. Koutsouras, F. Torricelli, P. W. M. Blom, *Adv. Electron. Mater.* **2023**, *9*, 2200868.

[164] V. R. Feig, H. Tran, M. Lee, K. Liu, Z. Huang, L. Beker, D. G. Mackanic, Z. Bao, *Adv. Mater.* **2019**,

31, 1902869.

[165] T. G. Kim, S. R. Ha, H. Choi, K. Uh, U. Kundapur, S. Park, C. W. Lee, S. H. Lee, J. Kim, J. M. Kim, *ACS Appl. Mater. Interfaces* **2017**, *9*, 19231.

[166] Z. Zhu, G. Yang, R. Li, T. Pan, *Microsystems Nanoeng.* **2017**, *3*, 17004.

[167] W. S. Chang, T. S. Chang, C. M. Wang, W. S. Liao, *ACS Appl. Mater. Interfaces* **2022**, *14*, 22826.

[168] J. Lee, S. Chung, H. Song, S. Kim, Y. Hong, *J. Phys. D. Appl. Phys.* **2013**, *46*, 105305.

[169] H. Guo, C. Liu, Y. Peng, L. Gao, J. Yu, *Sensors* **2023**, *23*, 6910.

[170] C. Liu, J. Deng, L. Gao, J. Cheng, Y. Peng, H. Zeng, W. Huang, L. W. Feng, J. Yu, *Adv. Electron. Mater.* **2023**, *9*, 2300119.

[171] Y. Peng, L. Gao, C. Liu, J. Deng, M. Xie, L. Bai, G. Wang, Y. Cheng, W. Huang, J. Yu, *Nano Res.* **2023**, *16*, 10206.

[172] T. D. Nguyen, T. Q. Trung, Y. Lee, N. E. Lee, *Adv. Eng. Mater.* **2022**, *24*, 2100918.

[173] W. Wang, Z. Li, M. Li, L. Fang, F. Chen, S. Han, L. Lan, J. Chen, Q. Chen, H. Wang, C. Liu, Y. Yang, W. Yue, Z. Xie, *Nano-Micro Lett.* **2022**, *14*, 184.

[174] X. Su, X. Wu, S. Chen, A. M. Nedumaran, M. Stephen, K. Hou, B. Czarny, W. L. Leong, *Adv. Mater.* **2022**, *34*, 2200682.

[175] B. Marchiori, R. Delattre, S. Hannah, S. Blayac, M. Ramuz, *Sci. Rep.* **2018**, *8*, 8477.

[176] S. Wang, J. Xu, W. Wang, G. J. N. Wang, R. Rastak, F. Molina-Lopez, J. W. Chung, S. Niu, V. R. Feig, J. Lopez, T. Lei, S. K. Kwon, Y. Kim, A. M. Foudeh, A. Ehrlich, A. Gasperini, Y. Yun, B. Murmann, J. B. H. Tok, Z. Bao, *Nature* **2018**, *555*, 83.

[177] S. W. Jung, Z. J. S. Choi, J. B. Koo, C. W. Park, B. S. Na, J. Y. Oh, S. S. Lee, H. Y. Chu, *ECS Solid State Lett.* **2014**, *4*, P1.

[178] D. Qi, Z. Liu, M. Yu, Y. Liu, Y. Tang, J. Lv, Y. Li, J. Wei, B. Liedberg, Z. Yu, X. Chen, *Adv. Mater.* **2015**, *27*, 3145.

[179] T. C. Shyu, P. F. Damasceno, P. M. Dodd, A. Lamoureux, L. Xu, M. Shlian, M. Shtein, S. C. Glotzer, N. A. Kotov, *Nat. Mater.* **2015**, *14*, 785.

[180] Y. Morikawa, S. Yamagiwa, H. Sawahata, R. Numano, K. Koida, M. Ishida, T. Kawano, *Adv. Healthc. Mater.* **2018**, *7*, 1701100.

[181] S. Xu, Y. Zhang, J. Cho, J. Lee, X. Huang, L. Jia, J. A. Fan, Y. Su, J. Su, H. Zhang, H. Cheng, B. Lu, C. Yu, C. Chuang, T. Il Kim, T. Song, K. Shigeta, S. Kang, C. Dagdeviren, I. Petrov, P. V. Braun, Y. Huang, U. Paik, J. A. Rogers, *Nat. Commun.* **2013**, *4*, 1543.

[182] G. Lanzara, N. Salowitz, Z. Guo, F. K. Chang, *Adv. Mater.* **2010**, *22*, 4643.

[183] D. S. Gray, J. Tien, C. S. Chen, *Adv. Mater.* **2004**, *16*, 393.

[184] D. Qi, K. Zhang, G. Tian, B. Jiang, Y. Huang, *Adv. Mater.* **2021**, *33*, 2003155.

[185] J. T. Kim, J. Pyo, J. Rho, J. H. Ahn, J. H. Je, G. Margaritondo, *ACS Macro Lett.* **2012**, *1*, 375.

[186] S. Zhang, E. Hubis, G. Tomasello, G. Soliveri, P. Kumar, F. Cicoira, *Chem. Mater.* **2017**, *29*, 3126.

[187] S. Lee, J. Jang, S. Lee, D. Jung, M. Shin, D. Son, *Gels* **2022**, *8*, 534.

[188] S. Bontapalle, M. Na, H. Park, K. Sim, *Chem. Commun.* **2022**, *58*, 1298.

[189] H. Lee, S. Lee, W. Lee, T. Yokota, K. Fukuda, T. Someya, *Adv. Funct. Mater.* **2019**, *29*, 1906982.

[190] J. Kang, Y. W. Lim, I. Lee, S. Kim, K. Y. Kim, W. Lee, B. S. Bae, *ACS Appl. Mater. Interfaces* **2022**, *14*, 24840.

[191] Y. Wang, D. Liu, J. Bai, X. Tian, P. T. Lai, S. Zhang, *Appl. Phys. Lett.* **2024**, *125*, 141901.

[192] N. Li, Y. Li, Z. Cheng, Y. Liu, Y. Dai, S. Kang, S. Li, N. Shan, S. Wai, A. Ziaja, Y. Wang, J. Strzalka, W. Liu, C. Zhang, X. Gu, J. A. Hubbell, B. Tian, S. Wang, *Science (80-.).* **2023**, *381*, 686.

[193] H. Shim, S. Jang, J. G. Jang, Z. Rao, J. I. Hong, K. Sim, C. Yu, *Nano Res.* **2022**, *15*, 758.

[194] L. Gao, M. Wu, X. Yu, J. Yu, *Int. J. Extrem. Manuf.* **2024**, *6*, 012005.

[195] S. Chen, A. Surendran, X. Wu, S. Y. Lee, M. Stephen, W. L. Leong, *Adv. Mater. Technol.* **2020**, *5*, 2000523.

[196] H. Yuk, J. Wu, X. Zhao, *Nat. Rev. Mater.* **2022**, *7*, 935.

[197] M. Mohsin, A. Hossin, Y. Haik, *J. Appl. Polym. Sci.* **2011**, *112*, 3102.

[198] T. Liu, X. Peng, Y. N. Chen, Q. W. Bai, C. Shang, L. Zhang, H. Wang, *Macromol. Rapid Commun.* **2018**, *39*, 1800050.

[199] E. Chiellini, A. Corti, S. D'Antone, R. Solaro, *Prog. Polym. Sci.* **2003**, *28*, 963.

[200] X. Crispin, S. Marciniak, W. Osikowicz, G. Zotti, A. W. D. V. A. N. D. E. R. Gon, F. Louwet, M. Fahlman, L. Groenendaal, F. D. E. Schryver, W. R. Salaneck, *Polym. Phys.* **2003**, 2561.

[201] J. K. Kim, I. Park, W. Kim, D. H. Wang, D. G. Choi, Y. S. Choi, J. H. Park, *ChemSusChem* **2014**, *7*, 1957.

[202] W. Meng, R. Ge, Z. Li, J. Tong, T. Liu, Q. Zhao, S. Xiong, F. Jiang, L. Mao, Y. Zhou, *ACS Appl. Mater. Interfaces* **2015**, *7*, 14089.

[203] K. Xu, W. Sun, Y. Shao, F. Wei, X. Zhang, W. Wang, P. Li, *Nanotechnol. Rev.* **2018**, *7*, 605.

[204] E. Hosseini, V. Ozhukil Kollath, K. Karan, *J. Mater. Chem. C* **2020**, *8*, 3982.

[205] C. Wang, K. Sun, J. Fu, R. Chen, M. Li, Z. Zang, X. Liu, B. Li, H. Gong, J. Ouyang, *Adv. Sustain. Syst.* **2018**, *2*, 1800085.

[206] Y. H. Kim, C. Sachse, M. L. MacHala, C. May, L. Müller-Meskamp, K. Leo, *Adv. Funct. Mater.* **2011**, *21*, 1076.

[207] W. Song, X. Fan, B. Xu, F. Yan, H. Cui, Q. Wei, R. Peng, L. Hong, J. Huang, Z. Ge, *Adv. Mater.* **2018**, *30*, 1800075.

[208] X. Wang, A. K. K. Kyaw, C. Yin, F. Wang, Q. Zhu, T. Tang, P. I. Yee, J. Xu, *RSC Adv.* **2018**, *8*, 18334.

[209] U. Lang, E. Muller, N. Naujoks, J. Dual, *Adv. Funct. Mater.* **2009**, *19*, 1215.

[210] N. Kim, S. Kee, S. H. Lee, B. H. Lee, Y. H. Kahng, Y. R. Jo, B. J. Kim, K. Lee, *Adv. Mater.* **2014**, *26*, 2268.

[211] C. Volkert, R. Colucci, R. Berger, P. Besenius, P. W. M. Blom, U. Kraft, *J. Mater. Chem. C* **2024**, *12*, 3865.

[212] H. Yamaguchi, K. Aizawa, Y. Chonan, T. Komiyama, T. Aoyama, E. Sakai, J. Qiu, N. Sato, *J. Electron. Mater.* **2018**, *47*, 3370.

[213] M. W. Lee, M. Y. Lee, J. C. Choi, J. S. Park, C. K. Song, *Org. Electron.* **2010**, *11*, 854.

[214] G. R. Ross, W. J. Heideger, *J. Chem. Eng. Data* **1962**, *7*, 505.

[215] H. Soleymani, M. Noormohammadi, M. A. Kashi, M. H. Amiri, J. J. Michels, K. Asadi, M. M. Abolhasani, *Adv. Mater. Interfaces* **2021**, *8*, 2001734.

[216] M. M. Abolhasani, M. Naebe, K. Shirvanimoghaddam, H. Fashandi, H. Khayyam, M. Joordens, A. Pipertzis, S. Anwar, R. Berger, G. Floudas, J. Michels, K. Asadi, *Nano Energy* **2019**, *62*, 594.

[217] C. Schaefer, J. J. Michels, P. Van Der Schoot, *Macromolecules* **2016**, *49*, 6858.

[218] P. J. Flory, *Principles of Polymer Chemistry*, Cornell University Press, New York **1953**.

[219] J. W. Cahn, J. E. Hilliard, *J. Chem. Phys.* **1958**, *28*, 258.

[220] D. J. Lipomi, B. C. K. Tee, M. Vosgueritchian, Z. Bao, *Adv. Mater.* **2011**, *23*, 1771.

[221] Z. Liang, X. Li, P. Luan, Z. Yang, J. Su, X. Li, F. Li, D. Zhang, J. Huang, H. Zhu, D. Wang, Z. H. Lu, Q. Zhu, *ACS Appl. Electron. Mater.* **2024**, *6*, 3409.

[222] H. Yu, Z. Wu, X. Huang, S. Shi, Y. Li, *Org. Electron.* **2018**, *62*, 121.

[223] L. Van Gheluwe, E. Munnier, H. Kichou, K. Kemel, F. Mahut, M. Vayer, C. Sinturel, H. J. Byrne, F. Yvergnaux, I. Chourpa, F. Bonnier, *Molecules* **2021**, *26*, 7440.

[224] S. H. Chang, C. H. Chiang, F. S. Kao, C. L. Tien, C. G. Wu, *IEEE Photonics J.* **2014**, *6*, 8400307.

[225] F. C. Tang, J. Chang, F. C. Wu, H. L. Cheng, S. L. C. Hsu, J. S. Chen, W. Y. Chou, *J. Mater. Chem.* **2012**, *22*, 22409.

[226] C. Hou, H. Yu, *J. Mater. Chem. C* **2020**, *8*, 4169.

[227] M. Kong, M. Garriga, J. S. Reparaz, M. I. Alonso, *ACS Omega* **2022**, *7*, 39429.

[228] S. Sakamoto, M. Okumura, Z. Zhao, Y. Furukawa, *Chem. Phys. Lett.* **2005**, *412*, 395.

[229] M. Stavytska-Barba, A. M. Kelley, *J. Phys. Chem. C* **2010**, *114*, 6822.

[230] B. D. Saksena, *Proc. Indian Acad. Sci. (Math. Sci.)* **1939**, *10*, 333.

[231] N. A. Zubair, N. A. Rahman, H. N. Lim, R. M. Zawawi, Y. Sulaiman, *RSC Adv.* **2016**, *6*, 17720.

[232] Y. A. Badr, K. M. Abd El-Kader, R. M. Khafagy, *J. Appl. Polym. Sci.* **2004**, *92*, 1984.

[233] W. Zhen, C. Lu, C. Li, M. Liang, *Appl. Clay Sci.* **2012**, *57*, 64.

[234] H. S. Dehsari, J. J. Michels, K. Asadi, *J. Mater. Chem. C* **2017**, *5*, 10490.

[235] E. J. Kramer, P. Green, C. J. Palmstrøm, *Polymer (Guildf).* **1984**, *25*, 473.

[236] N. Billecke, G. Rago, M. Bosma, G. Eijkel, A. Gemmink, P. Leproux, G. Huss, P. Schrauwen, M. K. C. Hesselink, M. Bonn, S. H. Parekh, *Histochem. Cell Biol.* **2014**, *141*, 263.

[237] C. H. Camp Jr., J. S. Bender, Y. J. Lee, *Opt. Express* **2020**, *28*, 20422.

[238] G. Scheiblin, R. Coppard, R. M. Owens, P. Mailley, G. G. Malliaras, *Adv. Mater. Technol.* **2017**, *2*, 1600141.

[239] L. V. Lingstedt, M. Ghittorelli, M. Brückner, J. Reinholz, N. I. Crăciun, F. Torricelli, V. Mailänder, P. Gkoupidenis, P. W. M. Blom, *Adv. Healthc. Mater.* **2019**, *8*, 1900128.

[240] C. Volkert, M. Brzezinski, P. Argudo, R. Colucci, S. H. Parekh, P. Besenius, J. J. Michels, U. Kraft,

Adv. Sci. **2025**, 2502853.

[241] M. Romero, D. Mombrú, F. Pignanelli, R. Faccio, Á. W. Mombrú, *ACS Appl. Electron. Mater.* **2023**, *5*, 4863.

[242] S. T. M. Tan, G. Lee, I. Denti, G. LeCroy, K. Rozylowicz, A. Marks, S. Griggs, I. McCulloch, A. Giovannitti, A. Salleo, *Adv. Mater.* **2022**, *34*, 2202359.

[243] T. C. Tsai, H. C. Chang, C. H. Chen, W. T. Whang, *Org. Electron.* **2011**, *12*, 2159.

[244] S. Dai, Y. Dai, Z. Zhao, F. Xia, Y. Li, Y. Liu, P. Cheng, J. Strzalka, S. Li, N. Li, Q. Su, S. Wai, W. Liu, C. Zhang, R. Zhao, J. J. Yang, R. Stevens, J. Xu, J. Huang, S. Wang, *Matter* **2022**, 3375.